UNIVERSITY OF SOUTHAMPTON

FACULTY OF ENGINEERING, SCIENCE AND MATHEMATICS

Optoelectronics Research Centre

Development of Frequency Converters with Extended Functionalities in Periodically Poled Silica Fibres

by

Albert Canagasabey

Thesis for the degree of Doctor of Philosophy

July 2009

UNIVERSITY OF SOUTHAMPTON

ABSTRACT

FACULTY OF ENGINEERING, SCIENCE AND MATHEMATICS
OPTOELECTRONICS RESEARCH CENTRE

Doctor of Philosophy

Development of Efficient Frequency Converters with Extended Functionalities in Periodically Poled Silica Fibres

by Albert Canagasabey

The centrosymmetry of amorphous silica can be broken through the technique of thermal poling, whereby the application of an electric field at elevated temperatures introduces an effective second-order nonlinearity. Quasi-phase-matching is realised through periodic ultra-violet erasure of the uniformly induced nonlinearity. A truly all-fibre laser system operating in the visible was envisioned to replace the crystalline frequency doublers currently employed. Despite the lower second-order-nonlinearity in poled silica fibres, the longer interaction length for comparable acceptance bandwidths, the higher damage threshold and straightforward integration makes them a very attractive substitute.

In this thesis, the routes taken to induce the maximum possible nonlinearity and the optimisation of the quasi-phase-matching technique to achieve the highest possible normalised conversion efficiency are reported. Periodic ultra-violet erasure for quasi-phase-matching allows scalability to longer interaction lengths in comparison to the photolithography technique previously employed. Further circular twin-hole fibres can be used instead of D-shaped fibres. A greater than 16 times improvement in the normalised conversion efficiency over previous results was obtained through the enhancement of key parameters of interaction length, stability and reproducibility. An average conversion efficiency of $\sim 15\%$ was demonstrated in a $\sim 32 cm$ long periodically poled fibre using a fibre laser source with just $\sim 200 W$ of peak power. The functionalities of all-fibre frequency converters have been extended to include broadband wavelength tunability of $45 nm$ and chirped period poling for precise control of the acceptance bandwidth.

Acknowledgements

I would like to express my sincere thanks to my supervisors, Prof. Peter Kazansky and Dr. Morten Ibsen. Their continual support and guidance have been instrumental in achieving the results presented in this thesis. I am grateful to Morten for arranging my first research visit to the ORC and subsequently supporting my application for admission in to the ORC PhD program. I am particularly thankful for his unwavering encouragements throughout the course of this work. I thank Dr. Costantino Corbari for all the help rendered to me in the lab, with the analysis of the results and the numerous technical discussions over the course of this work.

I thank our international collaborators for their tireless efforts and contributions to this work. The group at ACREO, Sweden is acknowledged for the many fibres and devices fabricated and sent to us over the years. Dr Walter Margulis is acknowledged for his support and the many enlightening discussions on the subject of this work. Prof. Evgeny Dianov's group at FORC, Russia is accredited for their technical help and for the fabrication of a number of specialty fibres used in this work. Dr. Alexey Gladyshev is thanked for his two visits to the UK to work closely with us and for his part in the results achieved. Dr. Yves Hernandez and Mr. Flavien Liegeois, our collaborators at Multitel, Belgium are thanked for building the high power fibre laser source used in the latter part of the work. Finally our collaborators at Brussels University, Dr. Serge Massar and Dr. Anh Tuan Nguyen and our collaborators at the University of Toronto, Dr. Li Qian and Mr. Eric Zhu are thanked for putting our devices to good use and for the resulting publications.

I would like to thank Dr. Zhaowei Zhang, Dr. Katia Gallo, Dr. Christophe Codemard, Dr. Ridzuan Mokhtar, Dr. David Banks, Dr. John Mills and Ms. Jindan Shi for their help with some of the experiments and for the many fruitful technical discussions. Further thanks to Dr. Gilberto Brambilla, Dr. Collin Sones, Dr. Senthil Ganapathy, Dr. Corin Gawith, Dr. James Gates, Mr. Carl Farrell, Mr. Junhua Ji and Dr. Nyuk Voo for the many equipment loans over the years. The help of the technicians, Mr. Simon Butler, Mr. Ed Weatherby, Mr. Tim McIntyre, Mr. Rob Standish and Mr. Mark Lessey for their efforts over the years is gratefully acknowledged.

I would like to thank my family for being very supportive of all my endeavours and my move to the UK. Finally I thank my Lord and Saviour Jesus Christ for the grace that has got me through this far.

Contents

Declaration of authorship

I, Albert Canagasabey, declare that this thesis titled, `Development of Frequency Converters with Extended functionalities in Periodically Poled Silica Fibres' and the work presented in it are my own. I confirm that:

- This work was done wholly or mainly while in candidature for a research degree at this University
- Where any part of this thesis has previously been submitted for a degree or any other qualification at this University or any other institution, this has been clearly stated
- Where I have consulted the published work of others, this is always clearly attributed
- Where I have quoted from the work of others, the source is always given. With the exception of such quotations, this thesis is entirely my own work
- I have acknowledged all main sources of help
- Where the thesis is based on work done by myself jointly with others, I have made clear exactly what was done by others and what I have contributed myself

Signed:…… …….

Date:…… …….

List of figures

List of tables

Acronyms

AFM	Atomic Force Microscope
AOM	Acousto-Optic Modulator
ASE	Amplified Spontaneous Emission
CLAP	CO2 Laser Assisted Poling
CW	Continuous Wave
DFG	Difference Frequency Generation
EDFA	Erbium Doped Fibre Amplifier
EO	Electro Optic
EYDFA	Erbium/Ytterbium Doped Fibre Amplifier
EFISH	Electric Field Induced Second Harmonic Generation
FBG	Fibre Bragg Grating
FOM	Figure of Merit
FRM	Faraday Mirrors
FWHM	Full Width Half Maximum
FWM	Four-Wave Mixing
GVD	Group Velocity Dispersion
GVM	Group Velocity Mismatch
HF	Hydrofluoric Acid
LEO	Linear Electro-Optic Effect
LPFG	Long Period Fibre Grating
MCVD	Modified Chemical Vapour Deposition
MIC	Michelson Interferometer
MOPA	Master Oscillator Power Amplifier
MZ	Mach-Zehnder Interferometer
NA	Numerical Aperture
OPG	Optical Parametric Generator
OSA	Optical Spectrum Analyser
PCM	Phase Contrast Microscope
PGC	Phase Generated Carrier
PPLN	Periodically Poled Lithium Niobate
PPLT	Periodically Poled Lithium Tantalate

PPSF	Periodically Poled Silica Fibre
PUV	Periodic Ultra-Violet erasure
QPM	Quasi-Phase Matching
SEM	Scanning Electron Microscope
SFG	Sum Frequency Generation
SHG	Second Harmonic Generation
SH	Second Harmonic
SI	International Unit System
SOP	State of Polarisation
SMF	Single Mode Fibre
SPM	Self Phase Modulation
SON	Second Order Nonlinearity
SBS	Stimulated Brillouin Scattering
SRS	Stimulated Raman Scattering
SVEA	Slowly Varying Envelope Approximation
THG	Third Harmonic Generation
TON	Third Order Nonlinearity
UV	Ultra-Violet

Symbols

A_{ω_i}	Amplitude of wave i
A_{OVL}	Mode overlap area
α	Attenuation constant
$\mathbf{B}$	Magnetic flux density
$\mathbf{D}$	Electric flux density
$d_{ijk}^{(i)}$	Nonlinear mixing tensor
d_{eff}	Effective nonlinear coefficient
Δk	Wave vector mismatch
$\Delta\lambda$	Bandwidth
$\mathbf{E}$	Electric field

E_{DC}	Frozen-in field
ε_0	Vacuum permittivity
ε	Strain
H	Magnetic field
η_1	Normalised efficiency
η_2	Normalised efficiency
$I_{2\omega}$	Second harmonic intensity
I_{OVL}	Mode overlap integral
k_i	Wave vector of wave i
L_c	Coherence length
L_W	Walk-off length
Λ_{QPM}	Phase matching period
λ_f	Fundamental wavelength
μ_0	Vacuum permeability
μ	Ion mobility
n	Refractive index
n_2	Nonlinear index
P	Electric polarisation
ρ_e	Photoelectric constant
ρ_f	Free charge density
r_{ijk}	Electro-optic coefficient
ζ	Normalised propagation coordinate
V_π	Pi voltage
φ	Optical phase
$\chi_{ijk}^{(i)}$	i^{th} order susceptibility tensor
ω_i	Angular frequency of wave i

Chapter 1: Introduction

1.1 General introduction

The field of nonlinear optics was born in 1961 with the first experimental observation of frequency doubling of a ruby laser by Franken et al [1]. Since then, intense research in this area has resulted in demonstrations of frequency down and up conversion, parametric fluorescence, parametric oscillation and amplification, etc. These demonstrations however, have always been in media possessing a non-vanishing second-order nonlinearity (SON), which are predominantly inorganic crystals lacking an inversion symmetry. Parametric processes based on the SON, such as frequency doubling are typically realised in crystalline materials such as, Lithium Triobate (LBO), Potassium Titanil Phosphate (KTP) and Beta Barium Borate (BBO). The parametric processes such as frequency doubling, sum and difference frequency generation, parametric oscillation and amplification are only efficient if the interacting waves are in phase. Through phase matching there is a unidirectional flow of energy from the input fields to the generated fields [2]. In the case of frequency doubling for example, the requirement for phase matching necessitates the fundamental and generated second-harmonic (SH) wave to experience the same refractive index. In practice, the wavelength dependence of the refractive index (chromatic dispersion) prevents this condition for collinear propagation of the fundamental and SH fields. An early and now common solution to this problem is to use the inherent birefringence of crystals. Quasi-phase-matching (QPM) is an alternative technique that has a number of distinct advantages. It allows the use of non-birefringent materials, access to larger nonlinear coefficients and access to a wider range of wavelength interactions, limited primarily by the transparency of the material.

The successful introduction of a significant and permanent SON in fused silica, a material inherently void of any SON due to its macroscopic inversion symmetry, has opened up a plethora of applications based on this technology [3]. Applications such as electro-optic modulation and SHG, which were once the sole domain of crystalline materials, can now be realised in glass-based devices such as optical fibres through a

process called poling. Poling in effect, serves to break the centrosymmetry of amorphous materials enabling the formation of a SON. The induced SON is limited to a maximum value of $1pm/V$ in fused silica, with typical values of $0.1-0.3pm/V$ in optical fibres. Nevertheless the low loss, the high optical damage threshold, ease of integration and the longer interaction length make poled silica fibres a very attractive alternative to expensive crystal based devices. The technique of QPM can also be implemented in poled fibres making phase matched SON processes a very real possibility.

1.2 Fibre lasers

The conception of the fibre lasers by Elias Snitzer in 1959 eventually led to the demonstration of a flash-lamp pumped neodymium doped fibre laser [4]. Although the potential advantages of a fibre laser over gas and semiconductor lasers were realised at its inception, the pumping schemes, initially the bulky flash-lamp and subsequently low power, limited lifetime diode lasers [5] severely limited their versatility. Interest in fibre lasers and amplifiers was revived in the mid-late eighties with the demonstration by Mears et al. of the erbium doped fibre amplifier (EDFA) [6]. By this stage the diode laser technology had also progressed, and within a very short period of time the EDFA pumped by diode lasers were commercially available. Since then intense research in the field of fibre lasers has produced a variety of fibre lasers, operating in continuous-wave (CW) and pulsed modes delivering a range of power levels up to and beyond the kilowatt level.

The operating wavelength range of the erbium doped fibre stretches from $\sim 1535-1620nm$, depending on the type of silica host glass. To access other wavelengths, a range of other rare-earth ions have been used. Fibres doped with ytterbium have been used to access wavelengths of $977nm$ [7], $1080nm$ [8-9], 1179nm [10] , and $980-1070nm$ from an external cavity tunable laser [11]. Neodymium doping has been used to access some wavelengths within this range [12] with CW tunable lasers over $896-940nm$ wavelength range demonstrated [13-15]. However ytterbium doped fibre lasers are often preferred due to their broader emission bandwidth, smaller quantum defect, and higher upper state lifetime, a particularly desirable trait for Q-switched operation. Neodymium [16] and praseodymium [17-18] based fluoride fibre

amplifiers operating around $1.3\mu m$ have also been demonstrated. Bismuth doped silica fibre lasers operating at a wavelength range $(1150 - 1300nm)$ just above that of ytterbium doped fibre lasers have also been demonstrated [19]. Further, thulium doping provides access to the $1.7 - 2.1\mu m$ range [20]. The shortest wavelength $(651nm)$ produced has been in samarium doped fibres pumped with $488nm$ from an argon-ion laser [21-22]. While the longest wavelength $(2260nm)$ produced has been in a thulium-sensitised holmium doped fibre [23]. Finally, fibre lasers based on the Raman gain can be realised provided a suitable wavelength pump laser of sufficiently high power is available. Thus with silica based fibre lasers an almost seamless coverage of the $\sim 1 - 2\mu m$ wavelength range has been achieved. Fluoride based fibre lasers in comparison offer a much wider range of wavelengths spanning from near-UV to mid-IR [24]. However their incompatibility with silica based systems (particularly for telecommunications), fragility and prohibitive costs have restricted their use to specialist applications.

1.2.1 Entering the visible

Historically, most visible lasers have been based on gas, dye or semiconductor gain media. Gas and dye lasers are known to be inherently inefficient, bulky and difficult to maintain, while semiconductor lasers are typically limited in power. For high power applications of visible light, frequency doubled solid-state lasers have become the preferred choice. Fibre lasers with their inherently high efficiency, high beam quality coupled with the ease of beam delivery makes them a particularly attractive alternative to solid state lasers. Their compactness, ruggedness and typically lower costs are an added bonus. However, just like their rare earth solid-state counterparts, they require secondary frequency conversion to access wavelengths in the visible.

The frequency doubling of erbium fibre lasers has been demonstrated with periodically poled lithium niobate (PPLN) [25] and also with periodically poled potassium titanyl phosphate (PPKTP) [26], which has a greater damage threshold to that of PPLN. Frequency doubling of ytterbium based fibre lasers have also been demonstrated with CW blue [27], green [28], and yellow [29] wavelengths. CW green fibre laser sources utilising PPLN are now commercially available. The low thermal conductivity and low damage threshold of PPLN has prevented it from being used in the frequency doubling

of high power fibre lasers. Frequency doubling of a pulsed ytterbium based fibre laser system has been demonstrated with an LBO crystal [30]. Visible light has also been generated with CW bismuth fibre lasers frequency doubled using PPLN [31] and also with Raman fibre lasers [32-34]. The complexities associated with launching light from fibre lasers in to bulk crystals, the high coupling losses, the low damage thresholds associated with such are some of the disadvantages that are typically considered inescapable for the generation of visible wavelengths. Periodically poled silica fibres (PPSF) are therefore an attractive all-fibre solution to frequency conversion of high power fibre lasers. The rationale for targeting fibre lasers for frequency conversion applications based on PPSF is straightforward as expounded in the following section.

1.2.2 All-fibre visible lasers

The ability to introduce a second order nonlinearity into silica, a ubiquitous constituent of photonic devices and systems offers a number of conspicuous advantages, such as ease of integration, adaptability and lower propagation losses. By introducing a figure of merit (FOM) [35], the comparisons between poled fibres and crystals can be more easily appreciated.

$$FOM = \frac{\left|\chi^{(2)}\right|^2 L^2 I}{exp(\alpha n^3)} \quad (1.1)$$

Where, $\chi^{(2)}$ is the second order susceptibility and is a measure of the SON, L is the interaction length, I is the intensity of the pump beam, α (m^{-1}) is the attenuation constant (loss) and n is the refractive index of the medium at the wavelength of operation. For low loss mediums (i.e. $\alpha n^3 \ll 1$) the denominator can be approximated to 1. The $\chi^{(2)}$ inducible through poling is relatively modest and this is the single most crucial disadvantage of silica based nonlinear frequency conversion. However, frequency doubling in silica fibre is nevertheless appealing given that the silica fibres possess a much lower loss ($0.2dB/km$) and much higher damage threshold of $10^5 MW/cm^2$ compared to $10^2 - 10^3 MW/cm^2$ for crystals, enabling it to withstand much higher intensities. The intrinsically lower chromatic dispersion of silica fibres allow longer interaction for comparable acceptance bandwidths and finally, silica fibres for poling are relatively cheaper and easier to manufacture than crystals.

Frequency doubling of fibre lasers in PPSF has been demonstrated using a master oscillator power amplifier (MOPA) source of $2ns$ pulse duration and $4kHz$ repetition rate delivering $4kW$ peak power. An average conversion efficiency of $\sim 21\%$ was demonstrated [36]. The electrodes for the PPSF structure was fabricated using the lithographic technique commonly employed in the fabrication of periodically poled crystals. The implementation of this technique in fibres is challenging, particularly for the fabrication of long lengths of PPSF required for high conversion efficiencies. A novel technique of periodic point-by-point ultraviolet (UV) laser erasure of uniformly poled fibres was proposed, allowing the fabrication of long lengths of PPSF with high accuracy domain boundaries. Using this technique, a $11.5cm$ long PPSF was fabricated and subsequently used to frequency double a MOPA laser source of $108W$ peak power, yielding an average conversion efficiency of 2.4% [37].

1.3 Challenges and limitations

A number of challenges and limitations similar to those of crystalline frequency conversion are also encountered for PPSF. These are:

1. Self phase modulation (SPM) is the time dependent optical phase shift caused by the Kerr effect, where the refractive index of the medium is modified by intense optical fields. The change to the refractive index is a function of the intensity and the nonlinear index (n_2). The induced phase change is dependent on the change to the refractive index and interaction length. In comparison to crystals, standard silica fibres (SMF28) have a relatively low value of n_2 ($3 \times 10^{-16} cm^2/W$), however the tighter confinement of light within fibres can still give rise to SPM, which could result in spectral broadening of the fundamental light and limit the efficiency of nonlinear frequency conversion. Ultrashort pulsed lasers are particularly prone to SPM given their high peak powers; however it is possible to fabricate PPSF devices from fibres with specifications matched to that of the laser.

2. Temporal walk-off can limit the length of the PPSF or the pulse duration of the fundamental source that can be frequency doubled as the pulses of the frequency components involved have differing group velocities. Group velocity

mismatch (GVM) for silica fibres is relatively low for fibres, however longer interaction lengths than crystals are also required to compensate for the lower nonlinearity.

3. The acceptance bandwidth (or phase-matching bandwidth) of the PPSF is controlled by the GVM between the interacting waves. The lower GVM of silica fibres is again beneficial in allowing longer interaction lengths for comparable bandwidth to crystals. As with periodically poled crystals, a linearly varying period can be implemented, allowing precise control of the bandwidth.

1.4 Summary of key achievements

This present work resulted in a number of demonstrations in the field of fibre poling, particularly for SHG. In addition, a number of processes allowing the optimisation of poling parameters to achieve the maximum possible nonlinearity were instituted. A number of fibre interferometers based on the Michelson and Mach-Zehnder configurations were designed and constructed. A range of improvements were made to the interferometers resulting in a 10-fold improvement in the measurement errors from the first interferometer constructed for this present work. The interferometers were also instrumental in the optimisation of the design of the twin-hole fibre. The excessive decay of the nonlinearity (up to 50% within 24 hours) of the early twin-hole fibres was eliminated through improved geometry of the twin-hole fibre. Further the fabrication techniques of the poled fibre devices were significantly improved, allowing serial fabrication and repeatability of experiments. These include the implementation of the side-polishing of twin-hole fibres and also the construction of a number of furnaces of varying sizes up to $\sim 42cm$.

The improved fibre design along with the extension of the interaction length of the PPSF grating, yielded a normalised conversion efficiency of $0.086\%/W$, a 4-fold improvement in comparison to the previously best reported value [37]. An average conversion efficiency of 15.2% was demonstrated, limited by the relatively moderate power of the fibre laser source available for this present work. Over 50% conversion efficiency is theoretically possible by fabricating twice as long devices, or by doubling

the effective nonlinearity or by making use of fibre laser sources having ~1kW peak power.

Periodic UV erasure for PPSF fabrication in comparison to the photo-lithographic technique is extremely versatile and relatively easy to implement. It can be used to fabricate very long lengths of PPSF with metre-long devices considered feasible. The length was improved $\sim 4.5X$ over the PPSF device made using the photo-lithographic technique [36]. A length of $\sim 32cm$ was demonstrated in this present work, limited by the range of the translation stage used for periodic UV erasure.

Finally, the functionality and versatility of the PPSF has been expanded through the adaptation of two techniques used commonly with fibre Bragg gratings (FBG). A highly efficient, robust compression tuner was utilised to demonstrate $\sim 45nm$ tunability of the fundamental wave. This technique is potentially ideal for the construction of an all-fibre tunable laser source based on the ytterbium fibre laser, given the very broad gain range. A tunable range approaching $100nm$ is considered practicable.

The acceptance bandwidth, as noted earlier, is regulated by the GVM of the fundamental and second harmonic waves and the interaction length. The technique of chirping can also be adapted to the case of PPSFs to modify the acceptance bandwidth of the QPM process to overcome the inevitable narrowing of the bandwidth for longer devices, allowing the spectral accommodation of ultrashort fibre lasers. The acceptance bandwidth for a $10cm$ long PPSF device, typically $\sim 1.5nm$ with periodic poling was broadened to $\sim 51.5nm$. Frequency converters can be tailor-made to match the specifications of fibre laser sources through bandwidth engineering.

1.5 Overview of chapters

In Chapter 2, a historical background and a theoretical overview of this present work is given. The origins of thermal poling of bulk silica and its advancement into silica fibre poling and applications, particularly for second harmonic generation are summarised. A theoretical overview and some mathematical expressions explaining some of the

relevant optical parametric processes are provided. Through the use of Maxwell's equations, the amplitude evolutions of the interaction of waves in a nonlinear media of non-vanishing SON are derived for plane waves and subsequently applied to cylindrical waves within fibres.

Chapter 3 is a summary of the key experimental procedures used within this present work. Experimental considerations such as the fabrication of the specialty twin-hole fibre, device fabrication techniques, the methods of measurement of the second order nonlinearity in uniformly poled fibres, the fabrication of the periodic structure for QPM and the techniques used for the characterisation of the PPSF are presented. The challenges encountered and the various improvements made to the *in-situ* measurement technique are explained in detail.

Chapters 4 and 5 report on the key experimental results of this present work along with discussions with a particular emphasis on the comparisons with previous results and the improvements made over the course of this work. The best results obtained for each of the twin-hole fibres used are presented, along with the techniques used for optimising the nonlinearity and the UV periodic erasure conditions. Chapter 5 gives the results of the efforts which were focussed primarily on extending the functionality of the PPSF. The results on the wavelength tunability and bandwidth engineering through chirped period erasure are presented in the chapter.

In Chapter 6, the conclusions of this present work are provided. A brief summary of the key achievements of this present work along with ideas for potential future applications of PPSF are discussed. The improvements made, particularly with the design of the twin-hole fibre and the techniques employed for the various experiments conducted for this present work are also discussed.

1.6 References

1. Franken, P.A., et al., *Generation of optical harmonics.* Physics Review Letters, 1961. **7**(4): p. 118.
2. Armstrong, J.A., et al., *Interactions between Light Waves in a Nonlinear Dielectric.* Physical Review, 1962. **127**(6): p. 1918.
3. Myers, R.A., N. Mukherjee, and S.R.J. Brueck, *Large-second-order nonlinearity in poled fused silica.* Optics Letters, 1991. **16**(22): p. 1732.

4. Snitzer, E., *Optical Maser Action of Nd+3 in a Barium Crown Glass.* Physical Review Letters, 1961. **7**(12): p. 444.
5. Stone, J. and C.A. Burrus, *Neodymium-Doped Silica Lasers in End-Pumped Fiber Geometry.* Applied Physics Letters, 1973. **23**(7): p. 388.
6. Mears, R.J., et al., *Low-Noise Erbium-Doped Fiber Amplifier Operating at 1.54-Mu-M.* Electronics Letters, 1987. **23**(19): p. 1026.
7. Yla-Jarkko, K.H., et al., *A 3.5 W 977 nm cladding-pumped jacketed air-clad ytterbium-doped fiber laser.* 2003 OSA Topical Meeting on Advanced Solid-State Photonics (ASSP) (Trends in Optics and Photonics Series Vol.83), 2003: p. 103.
8. Dominic, V., et al., *110W fibre laser.* Electronics Letters, 1999. **35**(14): p. 1158.
9. Jeong, Y., et al., *Ytterbium-doped large-core fiber laser with 1.36 kW continuous-wave output power.* Optics Express, 2004. **12**(25): p. 6088.
10. Sahu, J.K., et al. *12W Ytterbium doped all-fiber laser at 1179 nm*. in *Conference on Lasers and Electro-Optics*. 2009. Munich, Germany.
11. Okhotnikov, O.G., et al., *Mode-locked ytterbium fiber laser tunable in the 980-1070-nm spectral range.* Optics Letters, 2003. **28**(17): p. 1522.
12. Mears, R.J., et al., *Neodymium-Doped Silica Single-Mode Fiber Lasers.* Electronics Letters, 1985. **21**(17): p. 738.
13. Cook, A.L. and H.D. Hendricks, *Diode-laser-pumped tunable 896-939.5-nm neodymium-doped fiber laser with 43-mW output power.* Applied Optics, 1998. **37**(15): p. 3276.
14. Fu, L.B., et al., *Compact high-power tunable three-level operation of double cladding Nd-doped fiber laser.* IEEE Photonics Technology Letters, 2005. **17**(2): p. 306.
15. Soh, D.B.S., et al. *Cladding pumped Nd-doped fiber laser tunable from 908 to 938 nm*. in *Conference on Lasers and Electro-Optics/International Quantum Electronics Conference and Photonic Applications Systems Technologies*. 2004. San Francisco, California, USA: Optical Society of America.
16. Brierley, M.C. and C.A. Millar, *Amplification and Lasing at 1350nm in a Neodymium Doped Fluorozirconate Fiber.* Electronics Letters, 1988. **24**(7): p. 438.
17. Carter, S.F., et al., *Amplification at 1.3μm in a Pr3+-Doped Single-Mode Fluorozirconate Fiber.* Electronics Letters, 1991. **27**(8): p. 628.
18. Durteste, Y., et al., *Amplification and Lasing at 1.3μm in Praseodymium-Doped Fluorozirconate Fibers.* Electronics Letters, 1991. **27**(8): p. 626.
19. Dianov, E.M., et al., *CW bismuth fibre laser.* Quantum Electronics, 2005. **35**(12): p. 1083.
20. Funk, D.S. and J.G. Eden, *Chapter 3, Rare-Earth doped Fiber Lasers and Amplifiers*. 2 ed, ed. M.J.F. Digonnet. 2001, New York.
21. Farries, M.C., P.R. Morkel, and J.E. Townsend, *Samarium3+-Doped Glass-Laser Operating at 651-Nm.* Electronics Letters, 1988. **24**(11): p. 709.
22. Farries, M.C., P.R. Morkel, and J.E. Townsend, *The Properties of the Samarium Fiber Laser.* Fiber Laser Sources and Amplifiers, 1990. **1171**: p. 271.
23. Ghisler, C., et al., *A Tm3+ Sensitized Ho3+ Silica Laser at 2.04 Mu-M Pumped at 809 Nm.* Optics Communications, 1994. **109**(3-4): p. 279.
24. Funk, D.S. and J.G. Eden, *Chapter 4, Rare-Earth doped Fiber Lasers and Amplifiers*. 2 ed, ed. M.J.F. Digonnet. 2001, New York.
25. Taverner, D., et al., *Highly efficient second-harmonic and sum-frequency generation of nanosecond pulses in a cascaded erbium-doped fiber periodically poled lithium niobate source.* Optics Letters, 1998. **23**(3): p. 162.

26. Champert, P.A., S.V. Popov, and J.R. Taylor, *3.5 W frequency-doubled fiber-based laser source at 772 nm.* Applied Physics Letters, 2001. **78**(17): p. 2420.
27. Soh, D.B.S., et al., *A 980-nm Yb-doped fiber MOPA source and its frequency doubling.* IEEE Photonics Technology Letters, 2004. **16**(4): p. 1032.
28. Tovstonog, S.V., S. Kurimura, and K. Kitamura, *High power continuous-wave green light generation by quasi phase matching in Mg stoichiometric lithium tantalate.* Applied Physics Letters, 2007. **90**(5): p. 051115.
29. Sinha, S., et al., *Efficient yellow-light generation by frequency doubling a narrow-linewidth 1150 nm ytterbium fiber oscillator.* Optics Letters, 2006. **31**(3): p. 347.
30. Dupriez, P., et al. *80 W green laser based on a frequency-doubled picosecond, single-mode, linearly-polarized fiber laser*. in *Conference on Lasers and Electro-Optics and Quantum Electronics and Laser Science Conference*. 2006. Longbeach, California, USA: Optical Society of America.
31. Dianov, E.M., et al., *High-power cw bismuth-fiber lasers.* Journal of the Optical Society of America B-Optical Physics, 2007. **24**(8): p. 1749.
32. Feng, Y., et al., *Multiple-color cw visible lasers by frequency sum-mixing in a cascading Raman fiber laser.* Opt. Express, 2004. **12**(9): p. 1843.
33. Georgiev, D., et al., *Watts-level frequency doubling of a narrow line linearly polarized Raman fiber laser to 589nm.* Opt. Express, 2005. **13**(18): p. 6772.
34. Kablukov, S.I., et al., *Frequency doubling of a broadband Raman fiber laser to 655 nm.* Opt. Express, 2009. **17**(8): p. 5980.
35. Corbari, C., *Development of Non-Linear Waveguide Devices for Optical Signal Processing, PhD thesis*, in *Optoelectronics Research Centre*. 2005, Southampton University: Southampton, United Kingdom.
36. Pruneri, V., et al., *Greater than 20% efficient frequency doubling of 1532nm pulses in quasi-phase-matched germanosilicate fibres.* Optics Letters, 1999. **24**(4): p. 208.
37. Corbari, C., et al. *All-fibre frequency conversion in long periodically poled silica fibres*. in *OFC*. 2005. Anaheim, California, USA: Optical Society of America.

Chapter 2: Background

In this Chapter, a historical background of the poling process in silica is presented. The early observations of second-harmonic generation (SHG) in silica fibres which subsequently led to efforts in improving the conversion efficiency and later onto the investigations of a variety of poling techniques to introduce a permanent second-order nonlinearity (SON) are summarised in Section 2.1. The primary focus however is on thermal poling, the technique employed for the introduction of the SON in all the devices fabricated for this present work. The mechanisms responsible for the formation of the SON are discussed in Section 2.2 along with the shape and depth reached by nonlinear layer in the glass matrix. The applications of poled fibres realised thus far and their performances are reported in Section 2.3. Sections 2.4 and 2.5 present a theoretical overview of the nonlinear optical phenomena associated with the SON. Equations describing the evolution of SON processes are derived for plane waves and subsequently applied to cylindrical coordinates in fibres.

2.1 Nonlinearities in optical fibres

The field of fibre optics was born in 1950s with the realisation that a dielectric cladding could significantly improve the guidance of light within a higher index core [1]. This significant discovery thrust silica based optical fibres to the forefront as a transport medium for communications. The high losses of the first optical fibres (>1000dB/km) were drastically reduced over a 2 decade period to a level limited by the fundamental process of Rayleigh scattering. The advent of silica fibres further led to the discovery of a range of interesting nonlinear optical effects within fibres. Nonlinear effects such as stimulated Raman scattering (SRS) and stimulated Brillouin scattering (SBS) were some of the earliest studied [2-3]. Other effects such as self-phase-modulation (SPM) and four-wave-mixing (FWM) have also been extensively studied.

The accidental discovery of photosensitivity in silica fibres by Hill et al. led to the development of fibre Bragg gratings [4]. The invention of fibre amplifiers and later lasers based on doped silica fibres further increased the functionality of fibres and fuelled extensive research into the nonlinear effects based on the third-order

nonlinearity (TON). The inherent lack of a SON in silica has precluded it from active components such as, electro-optic modulators and switches, frequency converters, parametric oscillators, etc. Consequently, the functions based on the SON are performed by bulk crystalline materials. While the crystals used for SON processes are better suited for gas, solid-state and semiconductor lasers, they are less than ideal for all-fibre lasers which are poised to dominate applications typically reliant on conventional bulk lasers. The high insertion and propagation losses, the low damage threshold and the complexities involved in integrating bulky crystals within fibre-based systems warrants the drive for all-fibre solutions.

2.2 Second order nonlinearity in silica

The centrosymmetry of amorphous silica renders it unsuitable for nonlinear processes dependent on the SON. However, the unexpected generation of sum frequency light [5-6] and subsequently the generation of second harmonic light in Nd:YAG laser pumped optical fibres [7-9] suggested that the symmetry can in fact be broken. The demonstration by Österberg and Margulis of green second harmonic (SH) light generation within the silica fibre was by a slow process that eventually saturated at around 12 hours with $\sim 3\%$ of the fundamental light converted [8]. Stolen and Tom hypothesised that a permanent photoinduced change analogous to the photorefractive Hill gratings was responsible, given the length of time taken for the build-up of the SH light [10]. This photoinduced SHG was later attributed to the coherent photogalvanic effect, in which a spatially modulated static electric field is built up within the fibre [11-14]. This electric field combines with the intrinsic TON of the glass ($\chi^{(3)}$), giving rise to an effective SON ($\chi^{(2)}$). The low nonlinearity ($10^{-3} pm/V$) and the limited interaction length ($60 - 80 cm$) of the self-written grating owing to chromatic dispersion placed a fundamental limit on the conversion efficiency of photo-induced SHG to around 5% [7].

2.2.1 Electric field induced second harmonic generation

SH can be generated through the application of an electric field to a material possessing a TON. This technique, referred to as electric field induced second harmonic generation (EFISH) introduces an asymmetry in the symmetric material through the generation of

an effective electric dipole [15]. Since third order susceptibilities ($\chi^{(3)}$) are typically small, large voltages and high power lasers are required to observe the effect. The phase mismatch between the fundamental and second harmonic modes is compensated through the application of a spatially periodic electric field along the fibre. The electric field was applied through an interdigitated grating-electrode structure placed atop a fibre polished down to the inner cladding. The maximum conversion efficiency ($3.57x10^{-4}\%$) was limited by the interaction length and the accuracy of electrode fabrication [15].

2.3 Permanent second order nonlinearity

A renewed enthusiasm for frequency conversion in silica was born in 1991 with the demonstration of a high and permanent SON induced through thermal poling [16]. In this demonstration, Myers et al. showed that the simultaneous application of heat and high DC electric-field to bulk silica samples introduces a permanent SON with $\chi^{(2)}$ values as high as 1pm/V [16]. For about a decade following the first demonstration of thermal poling in silica, there were a slew of reports of thermal poling of silica thin films, silica fibres, lead silicate glasses and also other glass systems not based on silica. There have also been a number of reports on alternative poling techniques namely, UV poling [17], whereby a UV laser irradiates a sample while a strong electric-field is applied and CO_2 laser assisted poling (CLAP) in which the high intensity CO_2 laser beam is used as a heat source for thermal poling [18-19].

2.3.1 Mechanisms responsible for the induced second order nonlinearity

The demonstrations of DC induced second order nonlinearity spawned a considerable number of reports attempting to explain the mechanism responsible for the establishment of the effective SON. The reported hypotheses for the induction of $\chi^{(2)}$ are based primarily around two fundamental models.

1. Charge migration model
2. Dipole orientation model

In the charge migration model, the application of the strong electric field (E_{DC}) while the sample is at elevated temperatures causes the migration of impurity ions from the anode to the cathode [20]. The ionic migration leaves behind a negatively charged region over which the resistivity is increased, resulting in an intensification of the electric field in this region, which is subsequently locked in place when the sample is cooled down to room temperature. The creation of the effective SON, as with photoinduced SHG, was again attributed to the coupling of the electric field to the inherent TON of silica as described by;

$$\chi^{(2)} = 3\chi^{(3)}E_{DC} \quad (2.1)$$

In the dipole orientation model, the electric field acts to re-orient the dipoles within silica, leading to hyperpolarisation [21]. The report by Mukherjee et al. claims a combination of the two mechanisms as described by [20];

$$\chi^{(2)} \approx 3\chi^{(3)}E_{DC} + \frac{Np\beta}{5kT}E_{DC} \quad (2.2)$$

The first term, as stated above is the contribution from the frozen-in field and its action on the TON while the second term originates from $N\beta\langle cos^3\theta\rangle$ and describes the electric-field-induced orientation of the molecular second-order hyperpolarisability β, while θ is the angle between the molecular axis and the dc electric field. N is the concentration of the moieties that can be reoriented and p is the permanent dipole associated with the bond. Indeed the high SON obtained by Myers et al. favours the dipole orientation model over the charge migration model due to the ratios of $7:1$ and $2:1$ in the nonlinear coefficients d_{33} and d_{31} for p- and s-polarised light probes. However a more thorough study in poled bulk silica by Kazansky et al. yielded a ratio of $3:1$, strongly supporting the electric field induced SON model [21]. However a ratio of $3:1$ does not necessarily rule out the model based on dipole orientation.

2.3.2 Depletion region

The charge migration model is now generally accepted as the most plausible model or at the least the most dominant model for the creation of the depletion region. In the case of thermal poling, the sample is heated up to an optimum temperature typically in the range, $250°-290$℃ mobilising impurity ions commonly found in silica, such as

K^+, Li^+ and Na^+ [22]. The optimum temperature is determined by the strength of the applied field and the poling duration. The relative mobility of Na^+ in fused silica was reported to be an order of magnitude higher than Li^+ with mobility values of $\mu = 1 \times 10^{-13} m^2 s^{-1} V^{-1}$ [23] and $\mu = 5 \times 10^{-12} m^2 s^{-1} V^{-1}$ [24] reported. The action of the strong applied electric field drives the mobile ions towards the cathode, leaving behind a negatively charged region over which the resistivity is naturally increased due to the expulsion of mobile charges. A simplified model of the charge migration during poling is provided in Figure 2.1.

The width of the negatively charged region, also referred to as the depletion region and nonlinear region, can be as small as a few microns [25] to $10 \mu m$ [16, 26]. It is difficult to make a direct comparison between these reports as the composition of the bulk samples and fibres and the poling conditions used by the various groups are often different. Further, the width of the depletion layer is also dependent on the strength of the electric field [27] and the poling time [28]. However, for a first approximation of the space charge width and the field strength, Von Hippel's model assuming a single ionic carrier can be used [29]. In this approximation [24, 29], the width of the charge front, d, separating the depletion region near the anode from the neutral region near the cathode is given by;

$$d(t) = w.tanh\left(\frac{t}{\tau}\right) \quad (2.3)$$

With

$$\tau = \frac{L}{\mu}\sqrt{\frac{\varepsilon}{2qNV}} \quad (2.4)$$

And

$$w = \sqrt{\frac{2\varepsilon V}{qN}} = 2\tau\mu E_0 \quad (2.5)$$

Where w is the thickness of the depletion (nonlinear) region and τ is the time constant relation to its creation, q is the electron charge, N is the ionic concentration and μ as stated earlier, is the mobility of the ions; L is the width of the glass sample and ε is the permittivity. E_0, the electric field is given by $\frac{V}{L}$, where V is the applied DC voltage.

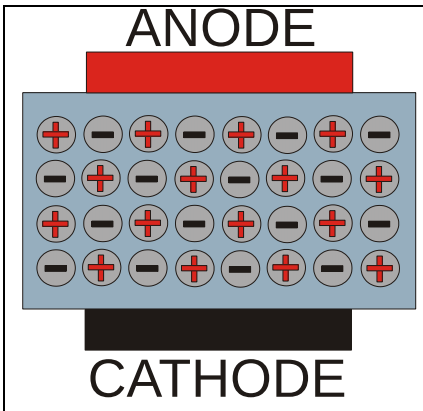	Electrodes are attached to the silica sample and the sample is heated up to the poling temperature at which the number of impurity ions available for conduction, particularly Na^{+}, is increased.
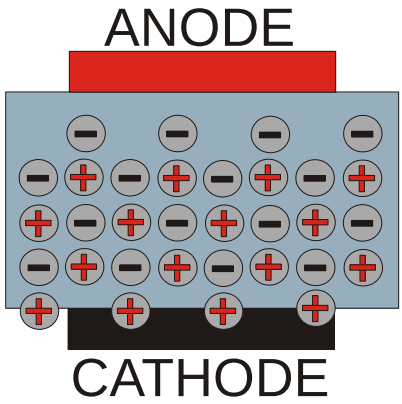	The application of the poling field mobilises the impurity ions, forcing them to move towards the cathode, leaving behind a region depleted of positive charges.
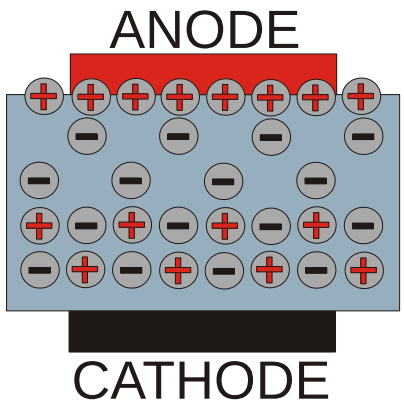	The applied field intensifies over the region depleted of the impurity ions as the resistivity is naturally increased. The negatively charged depletion region begins to attract positive charges from the surrounding atmosphere.
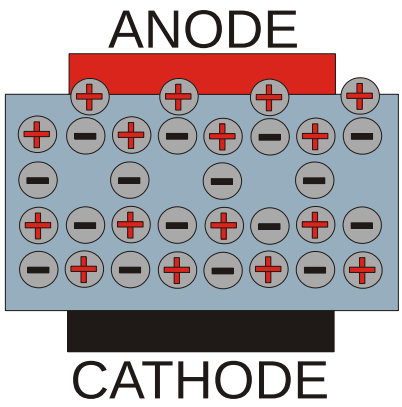	The silica sample is cooled down and the impurity ions are frozen-in, forming an electric field within the sample. Once the externally applied electric field is removed the sample further attracts positive charges from the atmosphere, bringing the overall net field to zero.

Figure 2.1 The formation of the depletion region during thermal poling

Faccio et al. showed experimentally the existence of an optimum poling duration, t_{opt} for the second-order nonlinearity [30]. Von Hippel's single carrier model is sufficiently accurate in explaining many of the experimental observations, particularly for thermal poling up to and within the optimum poling duration [30-31]. However it is found lacking for longer poling durations, in particular for durations above the optimum poling time where other charge carriers less mobile than Na^+ are involved. For poling durations exceeding t_{opt}, a multiple carrier model taking into account the other ions and injected charges can be employed [23-24, 32]. Kudlinski et al. used the multiple carrier model with two mobile carriers to map the spatial distribution of $\chi^{(2)}$ in 200μm thick Infrasil^{TM} samples for varying poling durations [31]. The layer-peeling technique [33] was used to characterise the $\chi^{(2)}$ in the poled samples for varying etch depths, revealing a very close match with the two-charge carrier model as seen in Figure 2.2.

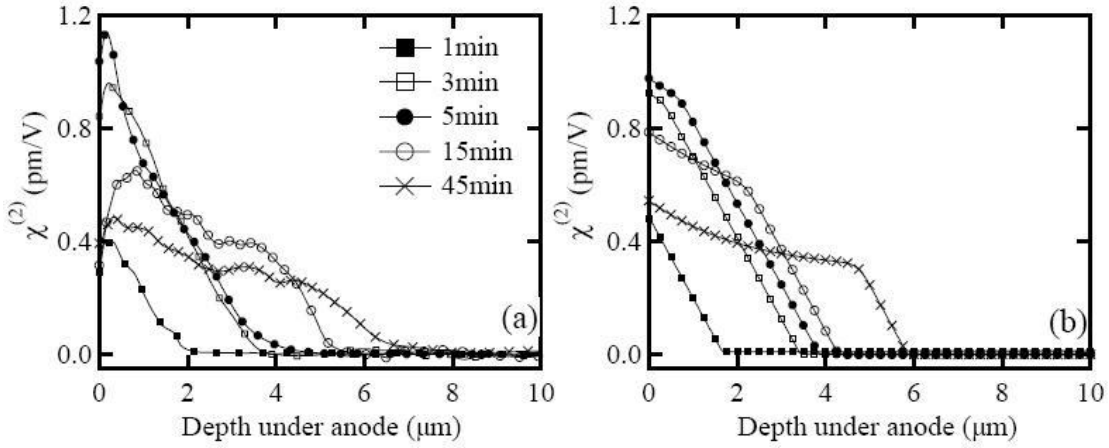

Figure 2.2 SON profiles experimentally obtained with the "layer peeling" method, for $200\,\mu m$ thick samples poled for 1, 3, 5, 15 and 45 minutes, and (b) the corresponding $\chi^{(2)}$spatial distributions obtained with the two-charge carrier model. From [31].

The spatial distribution (shape) of $\chi^{(2)}$ and the width of the depletion region is strongly dependent on the thickness of the poled sample. It is also strongly dependent on the poling duration, as the initial electric field, E_0 is not the same for varying sample thicknesses for the same poling voltage. The $\chi^{(2)}$ was shown to gradually decrease for increasing distance from the anode. The distribution of the nonlinear region is triangular for shorter poling durations as seen in Figure 2.2. For extended poling durations, the depletion region reaches further into the glass and the distribution tends to flatten out more, with an almost rectangular shape reported for a $500\mu m$ sample poled for 100 minutes [31]. Triques et al. showed that the width of the depletion region increases linearly with increasing poling voltage [27].

2.3.3 Charge injection

The poling model shown in Figure 2.1 is more applicable to thick samples where the injection of positive charges is predominantly on the surface of the anode side, since the thin (3-10μm) negatively charged depletion layer is located on the anode side. The injected charges act to shield and neutralise the frozen-in field, resulting in a zero net charge and electric field, $\int Edl = 0$.

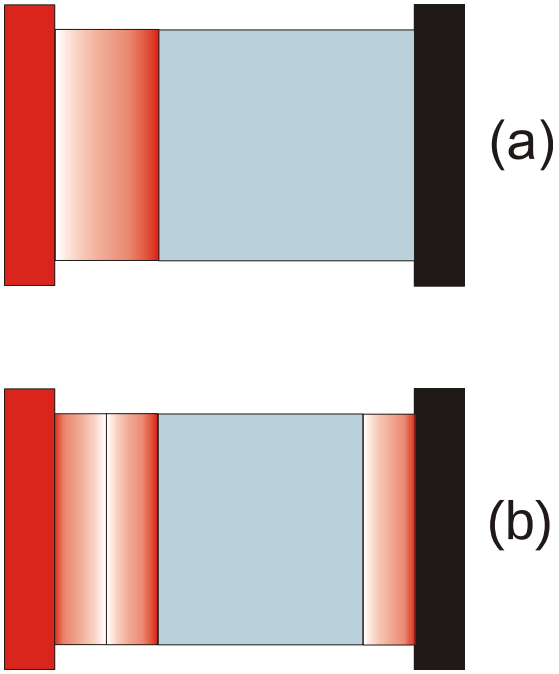

Figure 2.3 Thin sample poling (a) the distribution of impurity ions immediately after poling with darker red regions representing a higher concentration . (SON is higher in the lighter region) (b) The poled sample after neutralisation ($\int Edl = 0$) as a result of positive charge injection from the air and electrodes (width of regions not to scale)

In thin samples, such as fibres which typically have widths of 10-18μm, the positive charges are likely injected from both the anode and the cathode side as shown in figure 2.3. It is believed that the positive impurity ions which migrate toward the cathode are readily neutralised by free electrons within the glass matrix. The close proximity of the negatively charged depletion region to both surfaces in thin samples may result in the attraction and injection of the positive charges. This could potentially reduce the width of the depletion region and also reduce the strength of the frozen in-field. In fact, studies of the long term stability of thermally poled silica fibres indicate that there are two components: a fast decay occurring over a few hours and a slow component [34-35]. Thus, it is quite likely that the injection of positive charges is responsible for the fast decay of the electro-optic coefficient for fibres with the core positioned close to the

edge of the hole where the frozen-in field can be weakened or neutralised and for fibres with small hole-to-hole distances. In one of the fibres used in the present experiments, the fibre with the least separation between the holes (FORC-1, $10.5\mu m$ hole-to-hole spacing) about 50% of the induced residual electro-optic coefficient was depleted in a relatively short period of time (1-3hrs), whilst the FORC-2 fibre with a larger 31μm separation and core positioned 5μm away from the anode did not show any sign of decay. Thus for fibres a compromise between the hole-to-hole distance and the position of the core is required to induce the maximum but more importantly stable $\chi^{(2)}$ nonlinearity.

It has been shown that the incorporation of a borosilicate inner ring in the anode hole of the fibre serves to significantly improve the lifetime of the electro-optic coefficient [35]. The borosilicate layer may serve to impede the migration of positive charges towards the poled region by acting as a charge trapping layer.

2.3.4 Depletion visualisation through hydrofluoric etching

Fused silica can be effectively etched with hydrofluoric (HF) acid. There are many reports of HF etching studies carried out in poled silica, bulk and fibre, to visualise the poled region [36-38]. The etch rate of the poled region is faster in comparison to the un-poled regions and the small difference in the height resulting from etching can be detected using an atomic force microscope (AFM) [39], scanning electron microscope (SEM) [36] or a phase contrast microscope (PCM) [38, 40]. In twin-hole fibres, the HF etching technique reveals the distribution and profile of the frozen-in field, as seen in Figure 2.4 (a) and (b).

The microscope picture of the sample in Figure 2.4 (a) by Myren et al. is that of a twin-hole fibre with both holes completely filled with molten electrodes, giving rise to an axe-head shaped depletion profile [38], whereas in Figure 2.4 (b) wire electrodes were used for poling, resulting in a more circular layer. The same circular profile was also observed by Blazkiewicz et al. under similar poling conditions with wire electrodes [42].

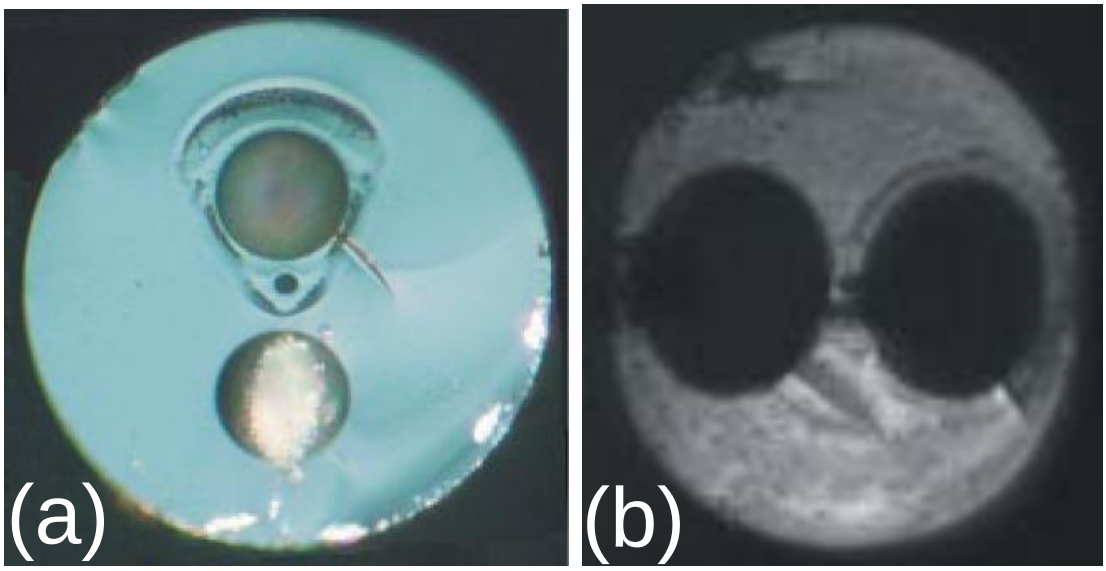

Figure 2.4 (a) poled fibre with alloy filled electrodes etched for 45 seconds and imaged with a phase contrast microscope, from [41]. (b) fibre poled with wire electrodes, etched and imaged with a phase contrast microscope.

2.4 Applications of poled silica fibre

There are a myriad number of applications for materials with a non-vanishing SON. Almost all of the research into the poling of silica and silica based materials has been focussed primarily on improving the understanding of the mechanisms and maximising the SON. A handful of groups have been developing devices based on the poled silica fibre. A summary of the poled fibre applications realised to date is presented here.

2.4.1 Quasi-phase matched second harmonic generation

In 1989, quasi-phase-matched (QPM) frequency conversion was first demonstrated in unpoled optical fibres using external inter-digited electrodes [15]. Later, in 1994, the group at the Optoelectronics Research Centre reported the first instance of QPM-SHG in poled silica fibres, generating blue light in a D-shaped fibre [43]. The conversion efficiency achieved was quite low, with just $400pW$ of blue light generated using a $100mW$ pump source. Then in 1997, frequency doubling in QPM D-shaped germanosilicate optical fibres was realised using periodic electrodes defined by standard photolithography by the same group with picosecond pulses [44] and then more efficiently with femtosecond pulses in 1998 [45]. By using a Q-switched pump source operating in nanoseconds, average conversion efficiency of 21%, (defined as

the ratio of the average SH power over the average fundamental pump power) was demonstrated for pump peak powers as high as $4\,kW$ corresponding to normalised conversion efficiency of $5x10^{-3}\ \%/W$ [46].

More recently, QPM has been successfully implemented using periodic ultraviolet erasure in uniformly poled silica fibres [47-48]. A conversion efficiency of 2.4% was achieved in a $11.5cm$ long, periodically poled fibre using a $108W$ (peak power) master oscillator power amplifier (MOPA) source operating at $1554.8nm$ as pump. The corresponding conversion efficiency normalised to the pump is $2.2x10^{-2}\%/W$ was the highest reported at the commencement of this present work.

2.4.2 Photon-pair generation through parametric fluorescence

The generation of photon-pairs through parametric fluorescence, a special case of difference-frequency-generation (DFG), where pump radiation at the frequency 2ω are transformed into two photons at ω, was demonstrated by Bonfrate et al. in 1999 [49]. The entangled photon pairs were generated in QPM, periodically poled silica fibre (PPSF). A CW Ti:sapphire laser with $300mW$ power operating at $766nm$ was launched into the PPSF device. Using InGaAs photo-detectors operating in the photon-counting mode, a photon-pair production rate of $150MHz$ was measured. More recently, PPSF devices fabricated for this present work were used for photon-pair generation with a significantly lower pump power of $43mW$ [50]. Correlated photon-pairs are imperative to quantum cryptography in improving the security of communications [51].

2.4.3 Poled fibre phase modulator and switch

A research group at ACREO, Sweden has demonstrated an optical phase modulator and a $2x2$ electro-optical switch [52-53]. The $1550nm$ single-moded fibre used for poling had a germanium rich core and a high NA of 0.27 with two $29.5\mu m$ holes positioned on either side of the core. The microscope picture of the fibre used is shown in Figure 2.4(a). The holes were filled with molten BiSn alloy and subsequently contacted through side polishing. The high NA of the fibre was chosen to minimise the losses

caused by the close proximity of the electrodes to the core. Thermal poling was performed at $265℃$ and a poling voltage of $4.4kV$ applied through the internal electrodes for a duration of 43 minutes. A V_π voltage of $210V$ was reported for a 37cm long device.

A poled fibre switch is an obvious application of the phase modulator described in the last section. The same group at ACREO incorporated a poled device in between two $2x2$ couplers, forming a $2x2$ Mach-Zehnder interferometer switch [52]. The switch was optimised for mode-locking and Q-switching of lasers rather than for telecoms switching. A preliminary demonstration of an actively mode-locked erbium doped fibre laser was made [54].

2.4.4 Poled fibre voltage sensor

The sensors group at the Optical Fibre Technology Centre (OFTC) in Sydney, Australia has demonstrated a fibre voltage sensor based on the linear electro-optic (LEO) response of the poled fibre device. Initially a standard twin-hole fibre design was utilised with two plate electrodes pressed against the fibre for the lab demonstration [55]. A low coherence interferometer based on a broadband depolarised source was fabricated. The depolarised light was split into two orthogonal polarisation states using a fibre pig-tailed polarising beam splitter. The orthogonally polarised light beams were then launched into the $31cm$ long poled fibre, where the natural birefringence of the twin-hole fibre maintains the two orthogonal polarisation states along the full interaction length. The light is reflected at the end of the poled fibre by a reflective coating applied to the fibre. The exploitation of the orthogonal polarisations for the interferometer ensures that the path lengths are automatically matched and the environmental variations affect both arms more or less equally, minimising noise significantly. The difference between the LEO (or the nonlinear coefficients d_{31} and d_{33}) coefficients in the two orthogonal polarisation states results in a difference in the phase shift experienced by the two orthogonally polarised beams. This difference in the phase measurement can be extrapolated to infer the voltage applied via the electrodes. The $50Hz$ test voltage applied yielded a reasonably linear response for voltages above $50Vrms$.

The group then progressed on to fabricate a high voltage field sensor based on the same principles of operation as the aforementioned lab sensor. The requirement for precise alignment of the poled fibre in relation to the externally applied electric field necessitated the design and fabrication of a new *keyed* fibre capable of maintaining its orientation. For this purpose, a new fibre was designed with two flat sections running along the length of the fibre. The uniformly poled double-flat twin-hole fibre was helically wound around a non-conducting tube and then packaged within a porcelain insulator. A $1.35m$ long fibre device was poled and packaged in this way and tested with externally applied voltages of up to $17kV$ [56].

2.5 Fibre nonlinearities and poling

For an intense electromagnetic field the response of optical fibres becomes nonlinear. Fibre nonlinearities can be represented mathematically by the induced polarisation of the electric dipoles **P** for applied electric field **E** as [57];

$$P = \varepsilon_0\left[\chi^{(1)}\mathbf{E} + \chi^{(2)}\mathbf{E^2} + \chi^{(3)}\mathbf{E^3} \ldots.\right] \quad (2.6)$$

Where ε_0 is the vacuum permittivity and $\chi^{(i)}$ $(i = 1,2,3 \ldots)$ is ith order susceptibility. The linear susceptibility $\chi^{(1)}$ makes up the greater part of **P** and its effects are included through the refractive index n of the medium and the fibre loss, α. The second-order susceptibility $\chi^{(2)}$ is responsible for nonlinear effects such as second-harmonic-generation (SHG), sum- (SFG) and difference-frequency-generation (DFG), etc. Amorphous materials such as silica display inversion symmetry on a macroscopic scale, as a result, $\chi^{(2)}$ vanishes for such media and SON processes are not possible. However, it is possible to induce an effective $\chi^{(2)}$ in silica through the technique of poling, in which an electric field is permanently frozen into the glass matrix. The frozen-in field combines with the inherent $\chi^{(3)}$ of the glass to give the effective $\chi^{(2)}$. This relation can be represented by $\chi^{(2)} = 3\chi^{(3)}E_{DC}$ (Equation 2.1).

The third order nonlinearity ($\chi^{(3)}$) which is responsible for phenomena such as third-harmonic-generation (THG), nonlinear refraction and FWM has a value of $2 \times 10^{-22}m^2/V^2$ for silica [58]. This coupled with the electrical breakdown voltage of $2 \times 10^9 V/m$ in silica [39, 59] limits the maximum attainable $\chi^{(2)}$ in silica to

approximately $1pm/V$. A value of this magnitude for $\chi^{(2)}$ has been reported for the poling of bulk silica [16] and in silica fibres [60], however, this value has not been consistently achieved, particularly in fibres. This is attributed to the lower nonlinearity experienced by the core of the fibre which is typically situated at a depth of a few microns from the anode hole in the fibre. In bulk samples the nonlinearity has been measured to be the highest at the surface in contact with the anode and tails off as it approaches the cathode as shown in Figure 2.2. In this thesis, the induced SON is assumed to be uniform across the cross section of the fibre for the interferometric measurements introduced in Chapter 3 and for all calculations of the nonlinear coefficient presented in Chapter 4.

2.5.1 Second order nonlinear susceptibility

In a medium of non-vanishing second order nonlinearity, two waves of angular frequencies, ω_1 and ω_2 can interact and produce, $|\omega_1 \pm \omega_2|$, $2\omega_1$, $2\omega_2$ and dc. The nonlinear susceptibility tensors introduced in the preceding section relate the cartesian components of the interacting and the newly induced polarisation fields. The second-order process involving the interaction of frequencies ω_1 and ω_2 for SFG ($\omega_3 = \omega_1 + \omega_2$) is

$$P_i(\omega_3) = \frac{\varepsilon_0}{2}\sum_{jk}\chi_{ijk}^{(2)}(-\omega_3, \omega_2, \omega_1)E_j(\omega_1)E_k(\omega_2) \quad (2.7)$$

And for DFG ($\omega_3 = \omega_1 - \omega_2$),

$$P_i(\omega_3) = \frac{\varepsilon_0}{2}\sum_{jk}\chi_{ijk}^{(2)}(\omega_3, \omega_2, -\omega_1)E_j(\omega_1)E_k(\omega_2) \quad (2.8)$$

Etc.

An alternative way of writing the second order susceptibility tensor is through the nonlinear coefficient, d, for example with SFG

$$\chi_{ijk}^{(2)}(-\omega_3, \omega_2, \omega_1) = 2d_{ijk}(-\omega_3, \omega_2, \omega_1) \quad (2.9)$$

Poled silica glass belongs to the crystallographic symmetry group $6mm$ or $C_{\infty mm}$ [61] which define the optical properties of the material. For frequencies $\omega_3, \omega_2, \omega_1$ for

which silica is transparent, Kleinman's conjecture ($d_{ijk} = d_{jik} = d_{jki}$) is valid and d is given by [62]

$$d = \begin{bmatrix} 0 & 0 & 0 & 0 & d_{31} & 0 \\ 0 & 0 & 0 & d_{31} & 0 & 0 \\ d_{31} & d_{31} & d_{33} & 0 & 0 & 0 \end{bmatrix} \quad (2.10)$$

With $d_{33} = 3d_{31}$

2.5.2 Nonlinear evolution equations

Nonlinear optical processes in optical fibres can be explained through Maxwell's equations which can be manipulated to describe the behaviour of electromagnetic waves in optical fibres. The plane wave evolution equations are derived and subsequently applied to cylindrical waves in optical fibres. In SI (*Syst`eme international d'unit´es*) units, the equations are

$$\nabla \times \mathbf{E} = -\frac{\partial \mathbf{B}}{\partial t} \quad (2.11)$$

$$\nabla \times \mathbf{H} = \boldsymbol{J} + \frac{\partial \mathbf{D}}{\partial t} \quad (2.12)$$

$$\nabla \cdot \mathbf{D} = \rho_f \quad (2.13)$$

$$\nabla \cdot \mathbf{B} = 0 \quad (2.14)$$

For a nonmagnetic mediums such as silica fibres void of charges and currents, Maxwell's equations can be expressed in the time domain as

$$\nabla \times \mathbf{E} = -\frac{\partial \mathbf{B}}{\partial t} \quad (2.15)$$

$$\nabla \times \mathbf{H} = \frac{\partial \mathbf{D}}{\partial t} \quad (2.16)$$

$$\nabla \cdot \mathbf{D} = 0 \quad (2.17)$$

$$\nabla \cdot \mathbf{B} = 0 \quad (2.18)$$

The electric field **E** is related to the electric flux density **D** through,

$$\mathbf{D} = \varepsilon_0 \mathbf{E} + \mathbf{P} \quad (2.19)$$

And **H**, the magnetic field is related to **B**, the corresponding magnetic flux density through,

$$\mathbf{B} = \mu_0 \mathbf{H} + \mathbf{M} \quad (2.20)$$

Where ε_0 is the vacuum permittivity and μ_0 is the vacuum permeability, **P** is the induced electric polarisation and **M** is the induced magnetic polarisation, which for fibres is equal to zero.

The wave equation describing light propagation in optical fibres can be deduced by taking the curl of Equation 2.15. Further simplifying using Equations 2.16 and 2.19 and the relation $\mu_0 \varepsilon_0 = \frac{1}{c^2}$ to express it in terms of **E** and **P** yields,

$$\nabla \times \nabla \times \mathbf{E} = -\frac{1}{c^2}\frac{\partial^2 \mathbf{E}}{\partial t^2} - \mu_0 \frac{\partial^2 \mathbf{P}}{\partial t^2} \quad (2.21)$$

Equation 2.21 describes the most general form of the wave equation in nonlinear optics. For low intensity fields, the response of the medium is linear and **P** is simply

$$\mathbf{P} = \varepsilon_0 \chi^{(1)} \mathbf{E} \quad (2.22)$$

Where $\chi^{(1)}$ is the linear electric susceptibility, which for isotropic media is a simple proportionality factor defining the refractive index; $n = \sqrt{1 + \chi^{(1)}}$. For intense electric fields, the response of the optical fibre becomes nonlinear and the induced polarisation is made up of both linear and nonlinear contributions as expressed in Equation 2.6. Using the identity,

$$\nabla \times \nabla \times \mathbf{E} = -\nabla^2 \mathbf{E} + \nabla(\nabla \cdot \mathbf{E}) \quad (2.23)$$

And with $\nabla \cdot \mathbf{E} = 0$, Equation 2.21 becomes,

$$\nabla^2 \mathbf{E} = \frac{n^2}{c^2}\frac{\partial^2 \mathbf{E}}{\partial t^2} + \mu_0 \frac{\partial^2 \mathbf{P}^{NL}}{\partial t^2} \quad (2.24)$$

In the case of poled silica, all tensor elements of $\chi^{(2)}_{ijk}$ are null apart from $\chi^{(2)}_{zzz}$ and $\chi^{(2)}_{zxx}$ with the former having a value 3 times that of the later. To avoid confusion, a

coordinate system where y is the direction of propagation and the field components polarised along the x or z direction is used (see Figure 2.5).

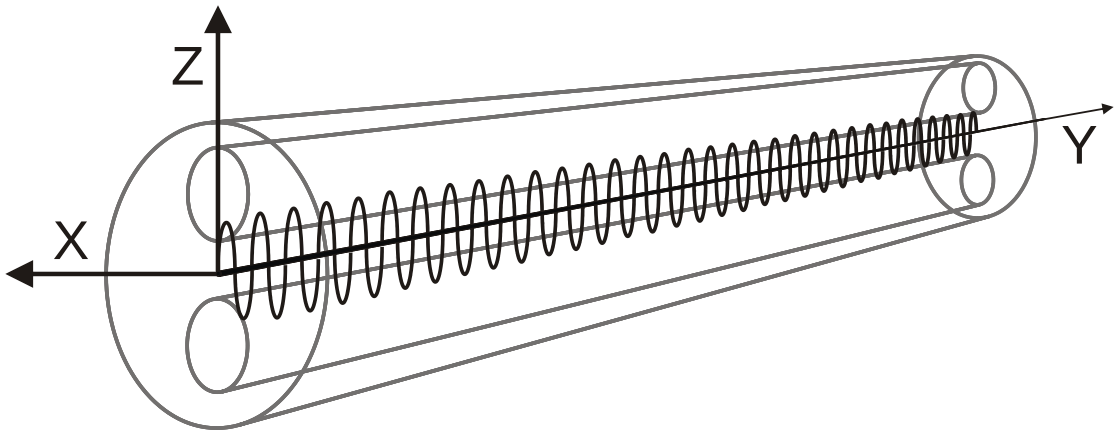

Figure 2.5 Coordinate system used to represent the interacting plane waves (the polarisation direction is shown as z)

Equation 2.24 then becomes

$$\frac{\partial^2 E_k}{\partial y^2} = \frac{n^2}{c^2}\frac{\partial^2 E_k}{\partial t^2} + \mu_0\left[\varepsilon_0 \frac{\partial^2}{\partial t^2}\chi_{ijk}^{(2)} E_i E_j\right] \quad (2.25)$$

Where the bracketed term is the contribution from the nonlinear polarisation for second order nonlinearities and the subscripts i, j, k can only take on the values x or z. If the field components E_i and E_j are at frequencies ω_1 and ω_2, then the frequency of E_k must be $\omega_3 = \omega_1 + \omega_2$. For the three co-linear waves polarised along the z-direction (highest SON) propagating along y-direction, the respective plane waves are

$$E^{\omega_1}(y,t) = \frac{1}{2}\left[A_{\omega_1}(y)e^{i(\omega_1 t - k_1 y)} + cc\right] \quad (2.26)$$

$$E^{\omega_2}(y,t) = \frac{1}{2}\left[A_{\omega_2}(y)e^{i(\omega_2 t - k_2 y)} + cc\right] \quad (2.27)$$

$$E^{\omega_3}(y,t) = \frac{1}{2}\left[A_{\omega_3}(y)e^{i(\omega_3 t - k_3 y)} + cc\right] \quad (2.28)$$

Where A_{ω_i} is the slowly varying amplitude of the interacting wave, i ($i = 1,2,3$). The nonlinear polarisation, $P_{\omega_i}^{NL}$, operating at the ω_3 frequency is

$$P_{\omega_3}^{NL}(y,t) = \frac{\varepsilon_0 \chi^{(2)}}{4} A_{\omega_1}(y) A_{\omega_2}(y) e^{i(\omega_1+\omega_2)t - (k_1+k_2)y} + cc \quad (2.29)$$

The left hand side of equation 2.25 can be expanded into

$$\frac{\partial^2 E^{\omega_3}}{\partial y^2}(y,t) = \frac{\partial^2}{\partial y^2}\left[\frac{1}{2}\left[A_{\omega_3}(y)e^{i(\omega_3 t - k_3 y)} + cc\right]\right]$$

$$= -\frac{1}{2}\left[k_3^2 A_{\omega_3}(y)e^{i(\omega_3 t - k_3 y)} + 2ik_3\frac{dA_{\omega_3}(y)}{dy}e^{i(\omega_3 t - k_3 y)} - \frac{d^2 A_{\omega_3}(y)}{dy^2}e^{i(\omega_3 t - k_3 y)}\right] + cc \quad (2.30)$$

The last term within the brackets can be neglected if the slowly varying envelope approximation (SVEA), $\frac{dA_{\omega_3}(y)}{dy} \gg \frac{d^2 A_{\omega_3}(y)}{dy^2}$, is assumed. Substituting Equation 2.30 without the last term into the left hand side of Equation 2.25 gives

$$-\frac{1}{2}\left[k_3^2 A_{\omega_3}(y)e^{i(\omega_3 t - k_3 y)} + 2ik_3\frac{dA_{\omega_3}(y)}{dy}e^{i(\omega_3 t - k_3 y)}\right]$$

$$= -\frac{1}{2}(\omega_3)^2\frac{n_3^2}{c^2}A_{\omega_3}(y)e^{i(\omega_3 t - k_3 y)} + \frac{\mu_0\varepsilon_0\chi^{(2)}(\omega_1+\omega_2)^2}{4}A_{\omega_1}(y)A_{\omega_2}(y)e^{i(\omega_1+\omega_2)t-(k_1+k_2)y} \quad (2.31)$$

Noting that $\omega_3 = \omega_1 + \omega_2$ and $k_3^2 = \frac{\omega_3^2 n_3^2}{c^2}$

$$\left[-\frac{k_3^2}{2}A_{\omega_3}(y) - ik_3\frac{dA_{\omega_3}(y)}{dy}\right]\frac{e^{i(\omega_3 t)}}{e^{i(k_3 y)}}$$

$$= -\frac{k_3^2}{2}A_{\omega_3}(y)\frac{e^{i(\omega_3 t)}}{e^{i(k_3 y)}} + \frac{\mu_0\varepsilon_0\chi^{(2)}(\omega_3)^2}{4}A_{\omega_1}(y)A_{\omega_2}(y)\frac{e^{i(\omega_3 t)}}{e^{i(k_1+k_2)y}} \quad (2.32)$$

Further simplification can be made by noting that $e^{i(\omega_3 t)}$ is common to all terms and that the first terms on either side cancel out.

$$ik_3\frac{dA_{\omega_3}}{dy}e^{-i(k_3 y)} = \frac{\mu_0\varepsilon_0\chi^{(2)}(\omega_3)^2}{4}A_{\omega_1}A_{\omega_2}e^{-i(k_1+k_2)y} \quad (2.33)$$

Dividing by $ik_3 e^{-i(k_3 y)}$ yields

$$\frac{dA_{\omega_3}}{dy} = -\frac{i\omega_3\chi^{(2)}}{4n_3 c}A_{\omega_1}A_{\omega_2}e^{-i(k_1+k_2-k_3)y} \quad (2.34)$$

Using the same method, the amplitude evolution equations for frequencies ω_1 and ω_2 are

$$\frac{dA_{\omega_1}}{dy} = -\frac{i\omega_1\chi^{(2)}}{4n_1c}A_{\omega_3}A^*_{\omega_2}e^{-i(k_3-k_2-k_1)y} \quad (2.35)$$

$$\frac{dA_{\omega_2}}{dy} = -\frac{i\omega_2\chi^{(2)}}{4n_2c}A_{\omega_3}A^*_{\omega_1}e^{-i(k_3-k_1-k_2)y} \quad (2.36)$$

Further simplifying Equations 2.34, 2.35 and 2.36 using the wave vector mismatch, $\Delta k = k_3 - k_2 - k_1$ yields

$$\frac{dA_{\omega_3}}{dy} = -\frac{i\omega_3\chi^{(2)}}{4n_3c}A_{\omega_1}A_{\omega_2}e^{i\Delta ky} \quad (2.37)$$

$$\frac{dA_{\omega_1}}{dy} = -\frac{i\omega_1\chi^{(2)}}{4n_1c}A_{\omega_3}A^*_{\omega_2}e^{-i\Delta ky} \quad (2.38)$$

$$\frac{dA_{\omega_2}}{dy} = -\frac{i\omega_2\chi^{(2)}}{4n_2c}A_{\omega_3}A^*_{\omega_1}e^{-i\Delta ky} \quad (2.39)$$

Equations 2.37, 2.38 and 2.39 can be used to describe the various nonlinear processes that are dependent on the $\chi^{(2)}$ nonlinearity.

2.5.3 Second harmonic generation

The process of SHG can be described mathematically simply by setting $\omega_1 = \omega_2 = \omega$ and $\omega_3 = 2\omega$. Equation 2.37 then becomes,

$$\frac{dA_{2\omega}}{dy} = \frac{i\omega d_{33}}{n_{2\omega}c}A^2_{\omega}e^{i\Delta ky} \quad (2.40)$$

And similarly for the fundamental wave,

$$\frac{dA_{\omega}}{dy} = \frac{i\omega d_{33}}{2n_{\omega}c}A_{2\omega}A^*_{\omega}e^{i\Delta ky} \quad (2.41)$$

Where n_ω and $n_{2\omega}$ represent the refractive index at the fundamental and second harmonic waves respectively and the nonlinear coefficient $d_{33} = \chi^{(2)}/2$ has been used. In a nonlinear medium of interaction length L, Equation 2.40 can be solved by integrating with boundary conditions $y = 0$ and y= L giving

$$A_{2\omega}(L) = \frac{\omega d_{eff} A_{\omega}^2}{n_{2\omega} c} \frac{e^{i\Delta kL} - 1}{\Delta k} \quad (2.42)$$

Where d_{eff} is the effective SHG coefficient which takes into account the polarisation state of the input beam and variations to the d coefficient (such as through periodic poling) over the length.

Taking the second harmonic intensity as $I_{2\omega} = \frac{1}{2}\varepsilon_0 n_{2\omega} c A_{2\omega} A_{2\omega}^*$ gives

$$I_{2\omega} = \frac{1}{2}\varepsilon_0 n_{2\omega} c \frac{\omega^2 d_{eff}^2 A_{\omega}^4}{n_{2\omega}^2 c^2} \frac{(e^{i\Delta k} - 1)(e^{-i\Delta k} - 1)}{\Delta k} \quad (2.43)$$

Introducing the intensity of the fundamental beam $I_{\omega} = \frac{1}{2}\varepsilon_0 n_{\omega} c |A_{\omega}^2|$ and simplifying further gives the second harmonic intensity

$$I_{2\omega} = 2\frac{\omega^2 d_{eff}^2 A_{\omega}^4 L^2 I_{\omega}^2}{\varepsilon_0 n_{2\omega} n_{\omega}^2 c^3} sinc^2\left(\frac{\Delta kL}{2}\right) \quad (2.44)$$

The quadratic dependence of the second harmonic intensity with quantities such as the fundamental intensity, the effective nonlinearity and the interaction length are clearly obvious from Equation 2.44. For $\Delta k = 0$, the process is said to be phase-matched and results in the maximum second harmonic intensity possible.

The variation for the second harmonic power with Δk is described by the $sinc^2$ function as shown in Figure 2.6. The second harmonic power is simply $P_{2\omega} = AI_{2\omega}$, where A is the area, which for a Gaussian beam is $A = \pi w_0^2$, with w_0 being the beam waist.

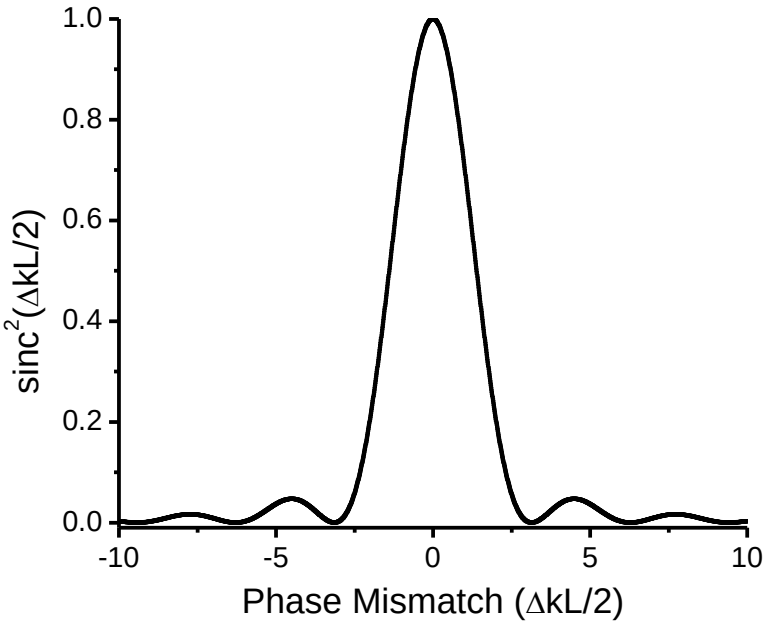

Figure 2.6 Variation of the second harmonic intensity with the wave vector mismatch Δk and interaction length L

2.6 SHG in optical fibres

The nonlinear evolution equations for the fundamental and SH in fibres can be developed using a technique analogous to that used for the plane waves in Section 2.4. Ignoring the radiation modes and assuming the weakly guiding approximation [63] which implies that $n_{core} - n_{cladding} \ll 1$ for cylindrical fibres, the electromagnetic field in the fibre can be expressed as a combination of the linearly polarised (LP) modes propagating in the y direction and polarised along the z direction (Figure 2.5);

$$E_z(y, r, \phi, t) = \frac{1}{2}\sum_{l,m}\left[A_{lm}(y) LP_{lm}(r, \phi) e^{i(\beta_{lm} y - \omega t)} + cc\right] \quad (2.45)$$

Where β_{lm} is the propagation constant for the l, m mode, which takes into account both material and waveguide dispersion through the effective refractive index at the specific wavelength. The LP_{lm} modes are normalised in such a way that,

$$\langle LP_{lm} | LP_{jk} \rangle = \delta_{jl} \quad (2.46)$$

Following Equations 2.40 and 2.41 the evolution equations for pump and the generated second harmonic in fibres are,

$$\frac{dA_{2\omega}}{dy} = \frac{i\omega d_{eff}}{n_{2\omega} c} A_{\omega}^2 I_{OVL} \sum_q e^{i(\beta_{2\omega} - 2\beta_{\omega} - K_q)y} \quad (2.47)$$

And similarly for the fundamental wave,

$$\frac{dA_{\omega}}{dy} = \frac{i\omega d_{eff}}{2n_{\omega} c} A_{2\omega} A_{\omega}^* I_{OVL} \sum_q e^{i(\beta_{2\omega} - 2\beta_{\omega} - K_q)y} \quad (2.48)$$

The wave vector mismatch, ΔK is defined as

$$\Delta K = \beta_{2\omega} - 2\beta_{\omega} - K_q \quad (2.49)$$

Where β_{ω} and $\beta_{2\omega}$ are the propagation constants of the fundamental and SH modes and the grating vector $k_q = \frac{2\pi q}{\Lambda}$, with $q = 1$ for a first order QPM interaction. The effective nonlinear coefficient, d_{eff} is a periodic function in the y direction with the period Λ, given by,

$$d_{eff} = \frac{\iint_{S_{fibre}} d_q(r,\phi) LP_{2\omega}(r,\phi) LP_{\omega}^2(r,\phi) d\sigma}{I_{OVL}} \quad (2.50)$$

Where

$$d_q(r,\phi) = \frac{d_{33}(r,\phi)}{q\pi} e^{iq\pi} \, sin(q\pi D) \quad (2.51)$$

And I_{OVL} is the overlap integral for the fundamental and SH modes given by

$$I_{OVL} = \iint_{S_{fibre}} LP_{2\omega}(r,\phi) LP_{\omega}^2(r,\phi) d\sigma \quad (2.52)$$

Equation 2.51 takes into account the periodicity of the nonlinear coefficient with the D being the duty cycle of the grating, defined as the ratio between the poled section and the period. Thus it is evident that the largest value of the nonlinear coefficient is obtained for $D = 50\%$ and $q = 1$. The second harmonic power $P_{2\omega}$ and the conversion efficiency η expressed as a function of the fundamental power P_{ω} for interaction length L is given by,

$$P_{2\omega} = \frac{2\omega^2 d_{eff}^2 L^2}{\varepsilon_0 c^3 n_\omega^2 n_{2\omega}} \frac{P_\omega^2}{A_{OVL}} sinc^2\left(\frac{\Delta KL}{2}\right) \quad (2.53)$$

$$\eta = \frac{2\omega^2 d_{eff}^2 L^2}{\varepsilon_0 c^3 n_\omega^2 n_{2\omega}} \frac{P_\omega}{A_{OVL}} sinc^2\left(\frac{\Delta KL}{2}\right) \quad (2.54)$$

Where the area overlap $A_{OVL} = \frac{1}{|I_{OVL}|^2}$. The value of $sinc^2$ at phase matching is 1. These equations consider only the interaction between the $LP_{01}^{\omega} \rightarrow LP_{01}^{2\omega}$ modes as all the fibres used in the present experiments were single moded at the fundamental wavelength and the mode of the second harmonic is set by the QPM period to the fundamental mode. The figure of merit (FOM) equation introduced in Chapter 1 is derived from the expressions for the SH power and conversion efficiency, Equations 2.53 and 2.54.

From Equation 2.54 it is clear that the parameter, area overlap (modal overlap), A_{OVL} has a significant influence over the conversion efficiency. The area overlap has a weaker dependence on the fundamental wavelength than it does on the NA of the fibre as seen in the simulation shown in Figure 2.7(a) where the variation of the A_{OVL} as a function of the fundamental wavelength and NA is illustrated. Figure 2.7 (b) shows the variation of A_{OVL} as a function of NA and core radius, where an even stronger dependence with the core radius is seen.

It would appear that fibres with larger NA and smaller core size would lead to higher efficiencies due to better overlap between the interacting modes. However, tighter confinement of the pump power may lead to higher order nonlinear processes as mentioned in Chapter 1. Smaller core size and larger NA also place tighter restrictions on the fabrication tolerances of the fibre as discussed later in this thesis.

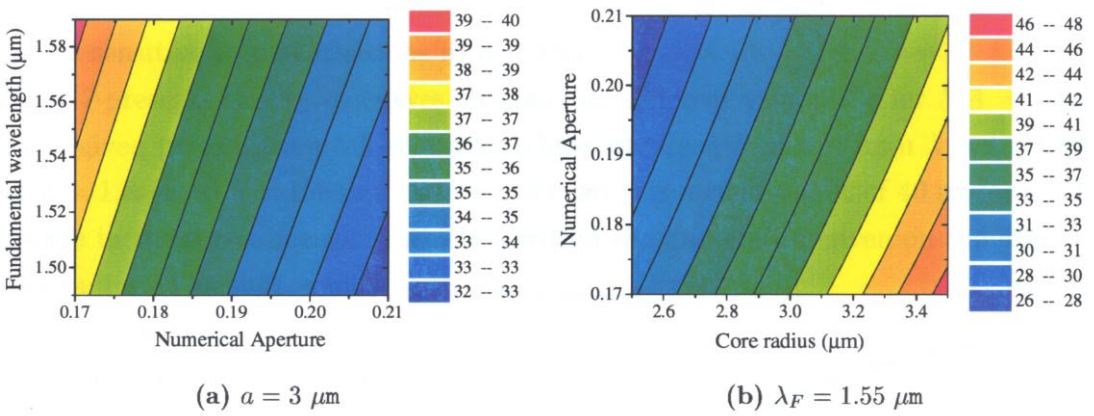

Figure 2.7 Area overlap as a function of (a) the fundamental wavelength and NA (b) NA and core radius. From [64].

As with other phase matching techniques, the QPM interaction is limited to a narrow spectral bandwidth as a result of chromatic dispersion. In a first order approximation, the acceptance bandwidth is given by [65]

$$\Delta\lambda \approx \frac{0.44\lambda_f^2}{cL \cdot GVM} \quad (2.55)$$

Where λ_f is the fundamental wavelength, L is the interaction length and GVM is the difference in the inverse of the group velocities of the two waves, given by

$$GVM = \left|v_g(2\omega)^{-1} - v_g(\omega)^{-1}\right| \quad (2.56)$$

Thus an inverse relationship exists between the acceptance bandwidth and the interaction length of the PPSF device. GVM also limits the length of interaction for pulsed sources as a result of *walk-off* between the fundamental and SH pulses. The walk off length, L_W is given by

$$L_W = \frac{\tau}{GVM} \quad (2.57)$$

Where τ is the pulse duration and the GVM for frequency doubling an erbium/ytterbium fibre laser with FORC-2 fibre was $43ps/m$. The laser sources used for frequency doubling in this present work operated in the nanosecond regime, for which the walk-off length was not an issue (e.g. $L_W = 46.5m$ for $2ns$ pulses). For frequency doubling of sources with picosecond or femtosecond pulse durations, the walk-off can be significant (e.g. $23cm$ for $10ps$ pulses) and the inherently broader spectral bandwidth of short pulse duration sources will limit the conversion efficiency

if it is not completely accommodated within the acceptance bandwidth of the PPSF device. The onset of SPM can further broaden the pulses within the fibre, limiting the conversion efficiency further.

2.7 Conclusions

A historical overview of silica poling and was presented in this chapter with a particular emphasis on thermal poling and the mechanisms responsible. The width and shape of the depletion region formed during poling was investigated in detail, given its relevance to twin-hole fibre poling and the typically lower SON inducible in comparison to bulk silica samples. A summary of the applications realised thus far in poled fibres was presented. Mathematical expressions describing the various nonlinear processes dependent on the SON were derived in Cartesian coordinates and subsequently represented in cylindrical coordinates to describe the process of SHG in periodically poled fibres.

2.8 References

1. Hecht, J., *City of Light*. 1999, New York: Oxford University Press.
2. Ippen, E.P. and R.H. Stolen, *Stimulated Brillouin-Scattering in Optical Fibers.* Applied Physics Letters, 1972. **21**(11): p. 539.
3. Stolen, R.H., A.R. Tynes, and E.P. Ippen, *Raman Oscillation in Glass Optical Waveguide.* Applied Physics Letters, 1972. **20**(2): p. 62.
4. Hill, K.O., et al., *Photosensitivity in optical fiber waveguides: Application to reflection filter fabrication.* Applied Physics Letters, 1978. **32**: p. 647.
5. Fujii, Y., et al., *Sum-Frequency Light Generation in Optical Fibers.* Optics Letters, 1980. **5**(2): p. 48.
6. Sasaki, Y. and Y. Ohmori, *Phase-Matched Sum-Frequency Light Generation in Optical Fibers.* Applied Physics Letters, 1981. **39**(6): p. 466.
7. Margulis, W. and U. Osterberg, *Second-Harmonic Generation in Optical-Glass Fibers.* Journal of the Optical Society of America B-Optical Physics, 1988. **5**(2): p. 312.
8. Osterberg, U. and W. Margulis, *Efficient Second Harmonic-Generation in an Optical Fiber.* Journal of the Optical Society of America B-Optical Physics, 1986. **3**(8): p. 102.
9. Osterberg, U. and W. Margulis, *Dye-Laser Pumped by Nd-YAG Laser-Pulses Frequency Doubled in a Glass Optical Fiber.* Optics Letters, 1986. **11**(8): p. 516.
10. Stolen, R.H. and H.W.K. Tom, *Self-Organized Phase-Matched Harmonic-Generation in Optical Fibers.* Optics Letters, 1987. **12**(8): p. 585.

11. Dianov, E.M., et al., *Test of Photovoltaic Model of Photoinduced Second Harmonic-Generation in Optical Fibers.* International Workshop on Photoinduced Self-Organization Effects in Optical Fiber, 1992. **1516**: p. 75.
12. Dianov, E.M., et al., *Evidence for Different Photovoltaic Mechanisms of Photoinduced Second-Harmonic Generation in Semiconductor Microcrystallite-Doped and Lead Glass.* Photosensitivity and Self-Organization in Optical Fibers and Waveguides, 1993. **2044**: p. 11.
13. Dianov, E.M., P.G. Kazansky, and D.Y. Stepanov, *Problem of the photoinduced second-harmonic generation.* Soviet Journal of Quantum Electronics, 1989. **19**: p. 575.
14. Dianov, E.M., P.G. Kazansky, and D.Y. Stepanov, *Photoinduced Effects in Optical Wave-Guides.* International Workshop on Photoinduced Self-Organization Effects in Optical Fiber, 1992. **1516**: p. 81.
15. Kashyap, R., *Phase-matched periodic electric field induced second harmonic generation in optical fibres.* Journal of the Optical Society of America, 1989. **6**(3): p. 313.
16. Myers, R.A., N. Mukherjee, and S.R.J. Brueck, *Large-second-order nonlinearity in poled fused silica.* Optics Letters, 1991. **16**(22): p. 1732.
17. Fujiwara, T., M. Takahashi, and A.J. Ikushima, *Second-harmonic generation in UV-poled germanosilicate glass.* Iooc-Ecoc 97 - 11Th International Conference on Integrated Optics and Optical Fibre Communications / 23Rd European Conference on Optical Communications, Vol 2, 1997(448): p. 119.
18. Quiquempois, Y., et al., *Study of organized chi((2)) susceptibility in germanosilicate optical fibers.* Optical Materials, 1998. **9**(1-4): p. 361.
19. Blazkiewicz, P., W. Xu, and S. Fleming, *Optimum parameters for CO2 laser-assisted poling of optical fibers.* Journal of Lightwave Technology, 2002. **20**(6): p. 965.
20. Mukherjee, N., R.A. Myers, and S.R.J. Brueck, *Dynamics of second-harmonic-generation in fused silica.* Journal of the optical Society of America B, 1994. **11**(4): p. 665.
21. Kazansky, P.G. and P.S.J. Russell, *Thermally poled glass: frozen-in electric field or oriented dipoles?* Optics Communications, 1994. **110**: p. 611.
22. Alley, T.G., S.R.J. Brueck, and M. Wiedenbeck, *Secondary ion mass spectrometry study of space-charge formation in thermally poled fused silica.* Journal of Applied Physics, 1999. **86**(12): p. 6634.
23. Kudlinski, A., et al. *Microscopic model for the second order nonlinearity creation in thermally poled bulk silica glasses*. in *Bragg Gratings, Photosensitivity and Poling in glass Waveguides*. 2003. Monterey, CA, USA: Optical Society of America.
24. Alley, T.G., S.R.J. Brueck, and R.A. Myers, *Space charge dynamics in thermally poled fused silica.* Journal of Non-Crystalline Solids, 1998. **242**(2-3): p. 165.
25. An, H. and S. Fleming, *Characterization of a second-order nonlinear layer profile in thermally poled optical fibers with second-harmonic microscopy.* Optics Letters, 2005. **30**(8): p. 866.
26. Franco, C.S., et al., *Measurement of depletion region width in poled silica.* Applied Optics, 2005. **44**(27): p. 5793.
27. Triques, A.L.C., et al., *Depletion region in thermally poled fused silica.* Applied Physics Letters, 2000. **76**(18): p. 2496.
28. Triques, A.L.C., et al., *Time evolution of depletion region in poled silica.* Applied Physics Letters, 2003. **82**(18): p. 2948.

29. Von Hippel, A., et al., *Photocurrent, space-charge buildup, and field emission in alkali halide crystals.* Physical Review Letters, 1953. **91**(3): p. 568.
30. Faccio, D., V. Pruneri, and P.G. Kazansky, *Dynamics of the second-order nonlinearity in thermally poled silica glass.* Applied Physics Letters, 2001. **79**(17): p. 2687.
31. Kudlinski, A., Y. Quiquempois, and G. Martinelli, *Modeling of the chi((2)) susceptibility time-evolution in thermally poled fused silica.* Optics Express, 2005. **13**(20): p. 8015.
32. Liu, X.M., X.H. Sun, and M.D. Zhang, *Theoretical analysis of thermal/electric-field poling fused silica with multiple-carrier model.* Japanese Journal of Applied Physics Part 1-Regular Papers Short Notes & Review Papers, 2000. **39**(8): p. 4881.
33. Kudlinski, A., et al., *Complete characterization of the nonlinear spatial distribution induced in poled silica glass with a submicron resolution.* Applied Physics Letters, 2003. **83**(17): p. 3623.
34. Janos, M., et al., *Growth and Decay of the Electrooptic Effect in thermally Poled B/Ge Codoped Fiber.* Journal of Lightwave Technology, 1999. **17**(6): p. 1037.
35. Canagasabey, A., et al. *Extended lifetime of the electro-optic coefficient in poled silica fibres*. in *Australian Conference on Optical Fibre Technology (ACOFT)*. 2001. Sydney, Australia: OSA.
36. Alley, T.G. and S.R.J. Brueck, *Visualization of the nonlinear optical space-charge region of bulk thermally paled fused-silica glass.* Optics Letters, 1998. **23**(15): p. 1170.
37. Myren, N. and W. Margulis, *Time evolution of frozen-in field during poling of fiber with alloy electrodes.* Optics Express, 2005. **13**(9): p. 3438.
38. Myren, N., et al., *Wide wedge-shaped depletion region in thermally poled fiber with alloy electrodes.* Optics Express, 2004. **12**(25): p. 6093.
39. Alley, T.G., S.R.J. Brueck, and R.A. Myers, *Space-charge dynamics in thermally poled fused silica.* Journal of Non-Crystalline Solids, 1998. **242**: p. 165.
40. Blazkiewicz, P., et al., *Mechanism for thermal poling in twin-hole silicate fibers.* Journal of the Optical Society of America B-Optical Physics, 2002. **19**(4): p. 870.
41. Myren, N., *Poled fiber devices, PhD thesis*, in *Department of Physics and Quantum Optics*. 2005, Royal Institute of Technology: Stockholm.
42. Blazkiewicz, P., et al., *Modification of thermal poling evolution using novel twin-hole fibers.* Journal of Lightwave Technology, 2001. **19**(8): p. 1149.
43. Kazansky, P.G., V. Pruneri, and P.S.J. Russell, *Blue light generation by quasi-phase matched frequency doubling in thermally poled optical fibre.* Optics Letters, 1995. **20**(8): p. 843.
44. Pruneri, V. and P.G. Kazansky, *Frequency doubling of picosecond pulses in periodically poled d-shape silica fibre* Electronics Letters, 1997. **33**(4): p. 318.
45. Pruneri, V., et al., *Efficient frequency doubling of 1.5um femtosecond laser pulses in quasi-phase matched optical fibres.* Applied Physics Letters, 1998. **72**(9): p. 1007.
46. Pruneri, V., et al., *Greater than 20% efficient frequency doubling of 1532nm pulses in quasi-phase-matched germanosilicate fibres.* Optics Letters, 1999. **24**(4): p. 208.
47. Bonfrate, G., V. Pruneri, and P.G. Kazansky. *Periodic UV erasure of the nonlinearity for quasi-phase-matching in optical fibres* in *Conference on lasers*

and Electro-Optics. 2000. San Francisco, California, USA: Optical Society of America.
48. Corbari, C., et al. *All-fibre frequency conversion in long periodically poled silica fibres*. in *OFC*. 2005. Anaheim, California, USA: Optical Society of America.
49. Bonfrate, G., et al., *Parametric fluorescence in periodically poled silica fibers.* Applied Physics Letters, 1999. **75**(16): p. 2356.
50. Huy, K.P., et al., *Photon pair source based on parametric fluorescence in periodically poled twin-hole silica fiber.* Optics Express, 2007. **15**(8): p. 4419.
51. Ekert, A.K., et al., *Practical Quantum Cryptography Based on 2-Photon Interferometry.* Physical Review Letters, 1992. **69**(9): p. 1293.
52. Fokine, M., et al., *Integrated fiber Mach-Zehnder interferometer for electro-optic switching.* Optics Letters, 2002. **27**(18): p. 1643.
53. Li, J., et al., *Systems measurements of 2x2 poled fiber switch.* IEEE Photonics Technology Letters, 2005. **17**(12): p. 2571.
54. Myren, N. and W. Margulis, *All-fiber electrooptical mode-locking and tuning.* IEEE Photonics Technology Letters, 2005. **17**(10): p. 2047.
55. Michie, A., et al., *Electric field and voltage sensing at 50 Hz using a thermally poled silica optical fibre.* Measurement Science & Technology, 2007. **18**(10): p. 3219.
56. Michie, A., *Sensing and interferometry, including design and characterisation of special optical fibres, PhD thesis*, in *Optical Fibre Technology Centre*. 2008, University of Sydney: Sydney.
57. Agrawal, G.P., *Nonlinear fiber optics*. 2 ed, ed. P.F. Liao, P.L. Kelley, and I. Kaminow. 1995, San Diego, CA: Academic Press.
58. Adair, R., L.L. Chase, and S.A. Payne, *Nonlinear refractive index measurement of glasses using three-wave frequency mixing.* Journal of the Optical Society of America, 1987. **4**: p. 875.
59. Quiquempois, Y., N. Godbout, and S. Lacroix, *Model of charge migration during thermal poling in silica glasses: Evidence of a voltage thersold for the onset of a second-order nonlinearity.* Physical Review A, 2002. **65**(4): p. 043816.
60. Kazansky, P.G., L. Dong, and P.S.J. Russell, *High second-order nonlinearities in poled silicate fibres.* Optics Letters, 1994. **19**(10): p. 701.
61. Corbari, C., *Development of Non-Linear Waveguide Devices for Optical Signal Processing, PhD thesis*, in *Optoelectronics Research Centre*. 2005, Southampton University: Southampton, United Kingdom.
62. Boyd, R.W., *Nonlinear optics*. 2nd ed. 2003, San Diego, CA: Academic Press. xvii.
63. Gloge, D., *Weakly Guiding Fibers.* Applied Optics, 1971. **10**(10): p. 2252.
64. Bonfrate, G., *Optical parametric processes in periodically poled silica fibres, PhD thesis*, in *Department of Electronics and Computer Science*. 2000, Southampton University: Southampton, United Kingdom.
65. Fejer, M.M., et al., *Quasi-Phase-Matched Second Harmonic-Generation - Tuning and Tolerances.* IEEE Journal of Quantum Electronics, 1992. **28**(11): p. 2631.

Chapter 3: Experimental methods

In this chapter the experimental techniques employed for this present work is explained in some detail. The challenges encountered with the fabrication of the twin-hole fibre, the construction of the measurement system for the induced second order nonlinearity and the frequency doubling experiments are expounded. The laser sources used for the initial characterisation of the PPSF devices are discussed along with the high power fibre lasers used to obtain the highest conversion efficiency possible.

3.1 Specialty poling fibre

The fabrication technique utilised for the twin-hole fibres used for this present work are similar to that of standard silica fibres. The fibre preform is manufactured by employing the modified chemical vapour deposition (MCVD) technique, whereby the cladding and core are deposited inside a fused silica tube [1]. Two identical holes are ultrasonically drilled on either side of the core with one hole positioned closer to the core than the other. This enables a higher SON to be induced within the core with thermal poling.

The completed preform with the two holes is mounted on a fibre-draw tower, consisting of a high temperature furnace, a diameter monitor, a polymer coating unit and a reeler. The preform is heated to a very high temperature until the end melts and begins to drop, passing through the diameter monitor (laser micrometer) and the coating unit. The polymer coated fibre then passes through the first UV curing oven where the coating is solidified through UV absorption and polymerisation. The coated fibre then traverses through a number of rollers before being spooled. A computerised control system ensures that the diameter of the fibre is kept to specifications by controlling the pulling speed.

3.1.1 Drawing induced twist and diameter variations

During the drawing process, the holes tend to collapse, consequently making the fibre elliptical in shape. The holes are typically pressurised while drawing to minimise the collapse as much as possible. The spooling process described above tends to twist the fibre while it is being drawn. If the fibre is twisted where the diameter is measured, the feedback control system adjusts the drawing speed to compensate for the change in diameter. The variation of the fibre diameter along the length directly results in variations of the core diameter and consequently the index of the fibre. The drawing induced twist limits the length of UV point-by-point erasure of the induced nonlinearity. All fibres used in this present work were affected by both of these detrimental effects. The degree of drawing induced twist varied from $\sim 5cm$ to $\sim 30cm$ for a 90° twist even in the same fibre spool. Although great care was taken to reduce the twist, it was not possible to completely prevent it from occurring during the fabrication process.

3.1.2 Core dopants

Specialty fibres fabricated for thermal poling are usually doped with higher concentrations of germanium than standard fibres. Aside from the primary purpose of increasing the index of the core glass, the rationale for germanium doping specialty twin-hole fibres is two-fold: 1. Possible enhancement of the SON through the presence of more defect centres and greater mobility of impurities. 2. Improve mode confinement and propagation losses which are inevitably affected due to the presence of the two holes. Increasing the concentration of germanium and thereby increasing the numerical aperture of the fibre improves the modal confinement and modal overlap of the propagating modes, however the splice losses to standard telecommunications fibre is also increased. Modal overlap of the co-propagating modes can be quantified through the parameter area overlap, introduced in Section 2.6. Secondly, for frequency doubling applications, greater control over diameter variations is required for fibres with higher NA as explained in Section 4.4.

Over the course of the project, five specialty twin-hole fibres were fabricated by three different groups. The first fibre used fabricated at the ORC was a very high NA (0.28)

germanium doped fibre. This fibre was used in the demonstration of high normalised conversion efficiency and the first demonstration of wavelength tuning. The yield for this fibre was particularly low as a result of irregularities in the core diameter and consequently the refractive index. This meant that it was difficult to ascertain the phase matching period for a specific wavelength and as a result a large number of devices made with this fibre were of no use. Plans to fabricate more fibre for this present work were hindered as a result of a devastating fire which destroyed the fibre fabrication facility at the ORC in October 2005. Since then two collaborations were commenced, the first with Fibre Photonics Group, ACREO, AB, Sweden which supplied two fibres of $125\mu m$ diameter. The second collaboration with Fibre Optic Research Centre (FORC), Russian Academy of Sciences, Russia also produced two fibres.

3.1.3 Twin-hole device fabrication

The twin-hole device for thermal poling is prepared firstly by determining and marking the hole closest to the core through the use of a microscope. In the case of positive poling, this is the anode hole and a positive voltage is applied within it. In the case of negative poling, a negative voltage is applied within this hole. The overall net effect is believed to be the same for both positive and negative poling with positive charges being expelled from around the hole. Due to practical reasons, all devices were fabricated with positive poling in this present work. The fibre is then mounted with the holes positioned perpendicular to the workbench and the top hole is polished with a fine sandpaper to enable access to the hole through the side of the fibre. A metal wire of high Young's modulus value and suitable diameter is then inserted in the hole. Tungsten and molybdenum with Young's modulus values of $411GPa$ and $329GPa$ were found to be suitable for wire diameters ranging from $20\mu m$ upwards. The device is then turned over and the procedure is repeated for the other hole from the other end of the fibre. Figure 3.1 shows the schematic of a device as prepared for poling.

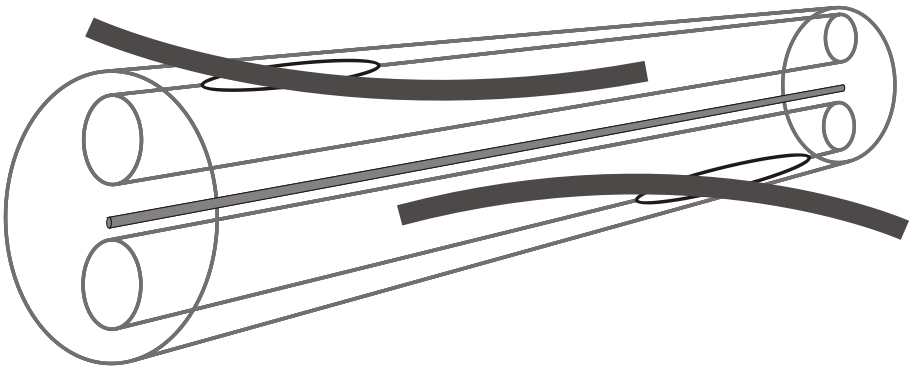

Figure 3.1(a). A specialty twin-hole fibre device with two electrodes inserted through side-polished holes

The overlap of the two wires and the anode electrodes are marked and the device is fusion spliced into one arm of a Mach-Zehnder or Michelson interferometer for *in-situ* measurement of the electro-optic coefficient during the poling procedure. While poling, the overlap region of the two wires is heated to an optimum temperature while a high DC voltage is applied across the wires.

3.2 Measurement of the induced nonlinearity

The measurement of the induced second order nonlinearity is pertinent in gaining an understanding of the poling mechanisms and in optimising the poling conditions. In poled bulk samples, the Maker fringe technique is often employed to measure the residual SON after poling. This technique has been used in poled fibre samples to probe the SON on the end-face of the fibre [2]. This measurement based on the measurement of the reflected SH signal, produced an unexpectedly high value of $\chi^{(2)}$ in the core of the fibre. This was attributed to the generation of second harmonic from the fundamental harmonic travelling along the core and subsequent reflection at the far end of the fibre. The implementation of this technique is difficult in the case of poled fibres and further, it does not allow the measurement of the nonlinearity during the poling process.

Since the objective of poling is to break the centrosymmetry and introduce a SON, it is obvious that an electric field could be used to cause a linear electro-optic effect (LEO) in the poled fibre. This effect results in a phase shift in the light traversing the fibre, which in turn gives a measure of the induced second order nonlinearity. The phase shift can be measured and quantified using an interferometer. This technique allows the

measurement of the evolution of the LEO and subsequently the SON during the poling process from the beginning to the end, allowing the precise optimisation of the poling parameters. A considerable amount of time was spent on the design and optimisation of interferometers for the *in-situ* measurement of the electro-optic coefficient. A review of these purpose-built interferometers and their principles of operation are given in the following sections. Firstly the relationship between the second order susceptibility and the electro-optic coefficient with the AC voltage induced phase shift is derived and explained.

3.2.1 Linear electro-optic effect in poled fibres

The application of an AC probe field during the poling process causes a change in the effective refractive index of the glass, which in turn results in a proportional phase shift in the light traversing the fibre. This is known as the linear electro-optic effect or Pockels effect. The electro-optic response becomes linear from the time the DC voltage is applied and the fibre device essentially becomes an electro-optic phase modulator. The measured phase can be used to calculate the electro-optic coefficient, r and the value of second order susceptibility, $\chi^{(2)}$. The relationship between these quantities is derived in this section.

With the application of the DC voltage, a DC electric field is setup in between the wires. Since the second order susceptibility is not intrinsic to silica it can be omitted and the nonlinear polarisation can be expressed in the temporal domain by;

$$P(t) = \varepsilon_0 \chi^{(1)} E(t) + \varepsilon_0 \chi^{(3)} E(t)E(t)E(t) \quad (3.1)$$

Using this equation with Equation 2.19 gives,

$$\varepsilon\varepsilon_0 E(t) = \varepsilon_0 E(t) + \left[\varepsilon_0 \chi^{(1)} E(t) + \varepsilon_0 \chi^{(3)} E(t)E(t)E(t)\right] \quad (3.2)$$

Simplifying,

$$\varepsilon E(t) = \left(1 + \chi^{(1)}\right) E(t) + \chi^{(3)} E(t)E(t)E(t) \quad (3.3)$$

Where the electric field for the electro-optic effect is now given by

$$E(t) = E_{DC} + \frac{1}{2}\{E_\omega + E_\Omega + cc\} \quad (3.4)$$

Where E_{DC} is the applied or frozen-in electric field and $E_\Omega = A_\omega e^{i\omega t}$ is the applied AC voltage of amplitude A_ω. E_ω is the optical field. Substituting Equation 3.4 into Equation 3.3 and taking into account frequencies around ω yields,

$$\begin{aligned}\frac{1}{2}\varepsilon\{E_\omega + cc\} = \frac{1}{2}\varepsilon\left(1 + \chi^{(1)}\right)\{E_\omega + cc\} \\ + \chi^{(3)}\left\{\frac{3}{2}E_{DC}E_{DC}E_\omega + \frac{6}{4}E_{DC}E_\Omega E_\omega + \frac{6}{4}E_{DC}E_{-\Omega}E_\omega + \frac{6}{8}E_\Omega E_{-\Omega}E_\omega\right. \\ \left. + \frac{3}{8}E_\omega E_{-\omega}E_\omega + \frac{3}{8}E_\Omega E_\Omega E_\omega + \frac{3}{8}E_{-\Omega}E_{-\Omega}E_\omega + cc\right\} \quad (3.5)\end{aligned}$$

Since $n \approx \sqrt{\varepsilon}$ at optical frequencies, Equation 3.5 can be simplified further and expressed in terms of the refractive index as

$$\begin{aligned}n^2 = n_0^2 + 2\chi^{(3)}\left\{\frac{3}{2}E_{DC}E_{DC} + \frac{6}{4}E_{DC}E_\Omega + \frac{6}{4}E_{DC}E_{-\Omega} + \frac{6}{8}E_\Omega E_{-\Omega} + \frac{3}{8}E_\omega E_{-\omega} + \frac{3}{8}E_\Omega E_\Omega\right. \\ \left. + \frac{3}{8}E_{-\Omega}E_{-\Omega}\right\} \quad (3.6)\end{aligned}$$

Where n_0 is the index of silica. Since the DC field is only measured by the second and third terms within the brackets, the other terms can be discarded to give,

$$n^2 = n_0^2 + 2\chi^{(3)}\{3E_{DC}A_\Omega \cos\Omega t\} \quad (3.7)$$

Where the Euler formula has been used for further simplification. Equation 2.1 can be substituted in Equation 3.7 to give an expression in terms of the induced $\chi^{(2)}$;

$$n^2 = n_0^2 + 2\chi^{(2)}A_\Omega \cos\Omega t \quad (3.8)$$

Giving

$$n = n_0\sqrt{1 + \frac{2\chi^{(2)}A_\Omega \cos\Omega}{n_0^2}} \approx n_0\left(1 + \frac{\chi^{(2)}A_\Omega \cos\Omega}{n_0^2}\right) \quad (3.9)$$

For which the amplitude of index change resulting from the applied AC voltage is

$$\delta n_\Omega = \frac{\chi^{(2)} A_\Omega}{n_0} \quad (3.10)$$

A_Ω can be represented in terms of the applied voltage, V_Ω and the effective distance, d_E between the electrodes,

$$A_\Omega = \frac{V_\Omega}{d_E} \quad (3.11)$$

The phase shift ($\delta\varphi_\Omega$) measured by the interferometer is related to the refractive index change through

$$\delta\varphi_\Omega = \frac{2\pi}{\lambda} L \delta n_\Omega \quad (3.12)$$

Combining Equations 3.10, 3.11 and 3.12 leads to

$$\chi^{(2)} = \frac{\lambda n_0 d_E}{4\pi L V_\Omega} \cdot \delta\varphi_\Omega \quad (3.13)$$

And the electro-optic coefficient (r) through the relation $\chi^{(2)} = \frac{n_0^4}{2} \cdot r$

$$r = \frac{\lambda d_E}{2\pi n_0^3 L V_\Omega} \cdot \delta\varphi_\Omega \quad (3.14)$$

3.2.2 The effective distance

It is clear from the preceding section (Equation 3.13) that the distance between the electrodes must be known for the SON to be calculated. The applied electric field is determined by the distance between the electrodes. The use of wire electrodes within twin-hole fibres for poling raises the question of their respective positions within the holes and consequently the separation between the two electrodes. It is assumed that the electrodes are brought together by the application of the high DC field during poling. However, if the weak AC test field is applied without the DC field, the positioning of the electrodes can be assumed to be statistically in the centre of the shown in Figure 3.2.

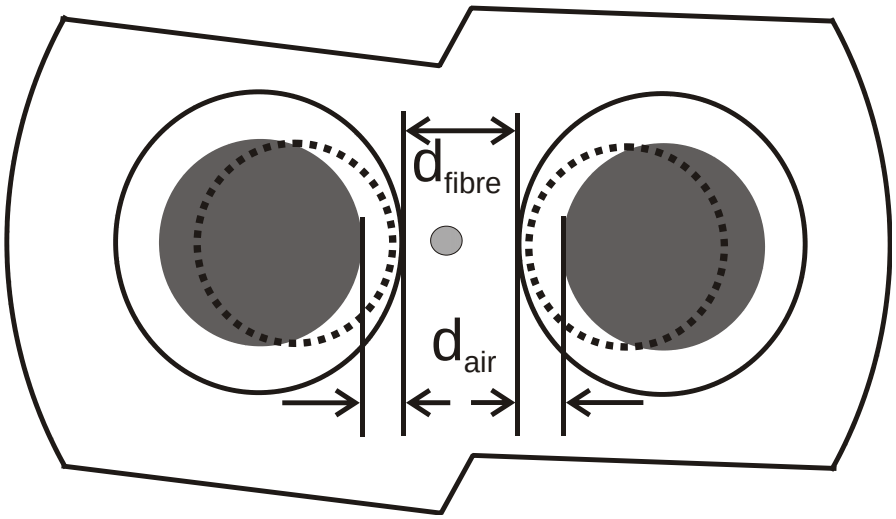

Figure 3.2 Cross section of the fibre devices with wire electrodes. Dots indicate the likely position of the wires during poling with DC field applied.

The effective distance d_E can be calculated taking into account the air gaps between the electrodes and the glass. In an environment with no free charges,

$$D_{air} = D_{fibre} \quad (3.15)$$

Where D_{air} and D_{fibre} are the electric displacements of the air and fibre respectively. Equation 3.15 can be represented by the relation:

$$\varepsilon_0 A_\Omega^{air} = \varepsilon_0 \varepsilon_{fibre} A_\Omega^{fibre} \quad (3.16)$$

Since $\varepsilon_{fibre} = n_0^2$,

$$A_\Omega^{air} = n_0^2 A_\Omega^{fibre} \quad (3.17)$$

From figure 3.2, the applied voltage, V_Ω is

$$V_\Omega = 2d_{air} A_\Omega^{air} + d_{fibre} A_\Omega^{fibre} \quad (3.18)$$

From Equation 3.17 and 3.18,

$$A_\Omega^{fibre} = \frac{V_\Omega}{d_{fibre} + 2d_{air} n_0^2} \quad (3.19)$$

Thus the effective distance is given by

$$d_E = d_{fibre} + 2d_{air}n_0^2 \quad (3.20)$$

The value of d_E for a FORC-2 fibre device with the $30\mu m$ electrodes positioned in the centre of the holes for example is $\sim 97\mu m$. If the electrodes are positioned against the edge of the holes as is the case during the application of the DC poling voltage, this would amount to a massive overestimation of the d_E by $66\mu m$, translating to more than $3X$ difference in the EO coefficient. Since devices were fabricated from a range of fibres of various hole sizes and various wire sizes, the electrodes were assumed to be positioned against the edge of the holes ($d_E = d_{fibre}$) for all measurements to avoid overestimation (see dotted representation of the electrodes in Figure 3.2). The residual values of the EO coefficient quoted within this thesis were measurements taken after a momentarily switching on the DC voltage to bring the electrodes together. This technique ensures that the actual residual value cannot be any lower than the measured value. The presence of debris, kinks in the wire and the disturbance of the field in-between the wires as a result of the grounded heater block could impact on the positions of the wires and consequently the induced nonlinearity. For accurate measurements of the nonlinearity and for the application of the maximum possible poling field across the core of the fibre it is ideal to have holes completely filled with electrodes. An alloy consisting of gold (80% wt) and tin (20% wt) was found to be ideal for this application by collaborators at ACREO [3]. The Au/Sn alloy is inserted at 300℃, and it is at a solid state during the poling process at 255℃. However for frequency doubling applications it is necessary to remove the wires after poling to reduce loss and to gain unimpeded access to the core for UV erasure (Section 3.3). Since the induced SON can also be thermally erased it is not possible to remove the alloy electrodes. Thus wire electrodes were used in the poling of all devices used for the frequency doubling work.

3.2.3 All-fibre Mach-Zehnder interferometer- the genesis

The first interferometric measurement of the evolution of the EO coefficient was made with an all-fibre Mach-Zehnder (MZ) interferometer system similar to the bulk system developed at the Optical Fibre Technology Centre, Australia [4]. The MZ interferometer was constructed by connecting two commercial $50:50$ splitting fibre couplers in series as shown schematically in Figure 3.3. For optimum fringe visibility,

the arms of the interferometer were matched to within a few centimetres below the coherence length of the laser diode source used. The challenge is to extract and quantify the fractional phase change in the poled device from the noise resulting from environmental (temperature, strain) variations in the interferometer. In the reference arm of the interferometer the fibre was glued onto a piezo-electric modulator stage. The piezo modulator was driven with a low frequency signal (typically $20Hz$) of sufficient amplitude to cause the interferometer to experience several fringe shifts for each direction of travel of the piezo stage. An AC-coupled detector at the output of the interferometer measures and outputs a signal for which the peak-to-peak value corresponds to the difference in the maxima (bright) and minima (dark) of the fringes.

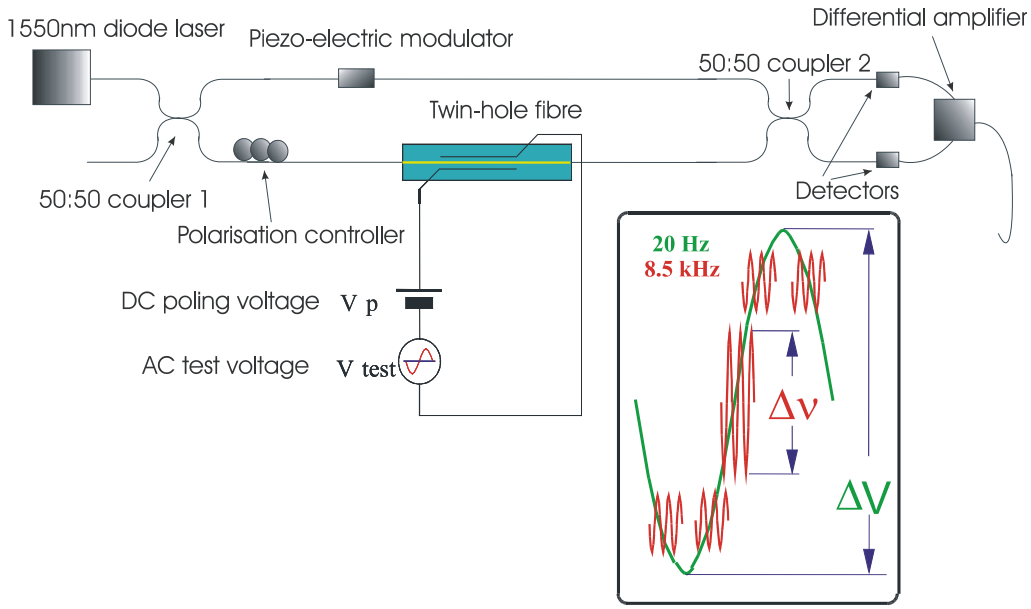

Figure 3.3 All-fibre Mach-Zehnder interferometer for in-situ measurements of the evolution of the second order nonlinearity

In the other arm, the twin-hole fibre device containing two internal electrodes is spliced in. A high frequency ($8.5kHz$) AC test signal is applied through the electrodes along with the high DC voltage required for the poling. Before the application of the DC voltage and before any second order nonlinearity is induced in the fibre, only the signal produced by the $20Hz$ modulation is visible (see slow modulation in the inset of Figure 3.3). With the application of a DC field across the core of the fibre, the $8.5kHz$ signal becomes visible (see fast modulation in the inset of Figure 3.3). The amplitude of the $8.5kHz$ signal is determined by the strength of the applied DC field across the core. Once poling is commenced by the application of heat, the amplitude of the $8.5kHz$ grows. The ratio of the $8.5kHz$ amplitude to the $20Hz$ amplitude gives a measure of

the fractional phase shift induced by the poled fibre device with which the electro-optic coefficient and second order nonlinearity are subsequently calculated. The inset in Figure 3.3 shows the typical output from the detector. A program written in LabView is used to filter the two interferometric signals ($20Hz$ and $8.5kHz$), measure the peak-to-peak amplitudes and to calculate the phase shift according to [4];

$$\delta\varphi_{\Omega} = 2sin\left(\frac{\Delta v}{\Delta V}\right) \quad (3.21)$$

3.2.4 Commercial phase demodulator for phase measurements

During the course of this present work, a commercial phase demodulator was acquired in the hopes of improving the accuracy and lowering the noise in the measurements of the electro-optic coefficient. The Mach-Zender interferometer described in the preceding section was rebuilt with a more efficient commercial piezo fibre stretcher phase modulator in place of the homemade modulator. The voltage required for π-phase shift (V_{π}) for the commercial phase modulator is $\sim$30 times lower than that of the homemade device, eliminated the need for amplification of the drive signal.

The phase demodulator, *Optiphase OPD 4000* (OPD), utilises the phase generated carrier (PGC) technique originally proposed by Dandridge et al. [5] for the extraction of phase in the sensor arm containing the poled fibre device. In an interferometer, the intensity variation at the output is given by

$$I = A + Bcos\theta(t) \quad (3.22)$$

Where the constants A and B are related to the input optical power and fringe visibility and $\theta(t)$ is the phase difference between the arms of the interferometer. In the implementation of the PGC technique, a large amplitude phase shift at an operating frequency outside the signal frequency is introduced into the phase factor $\theta(t)$. The intensity is now represented by

$$I = A + Bcos(Ccos\omega_0 t + \varphi(t)) \quad (3.23)$$

Where the superimposed signal of (carrier) frequency ω_0, has an amplitude of C. The $\varphi(t)$ term carries the phase of the signal of interest. The carrier signal carries the signal

as sidebands and is then extracted by the OPD using inverse trigonometric functions and digital signal processing. The software of the OPD controls three servos in real time: 1. Modulation amplitude- this is the amplitude of the drive signal to the piezo fibre modulator and the OPD maintains this at a modulation depth of π. 2. Modulation phase- this servo maintains the phase of the modulation signal to the measured carrier signal so that the signal phase could be extracted at the *zero* modulation points, i.e. at quadrature points. 3. Input level- this servo ensures that the signal amplitude fed to the internal analog to digital (ADC) convertor is maintained at a constant level. These three servos are used by the OPD to make accurate measurements of the signal phase at the quadrature points of the interferometer. Variations to the power or the fringe visibility as a result of polarisation drifts and changes to light intensity in the poled device arm as a result of wire movements can destabilise the OPD and cause constant changes to the servos (particularly the input level servo), resulting in increased noise in the measurements.

The phase evolution in the twin-hole fibre device is measured continuously and the electro-optic coefficient during the poling process is calculated using the Equation 3.14 in a LabView program. All parameters, aside from the measured phase shift, $\delta\varphi_{\Omega}$ are entered in manually on the front panel of the LabView program. The phase shift measured by the OPD is represented as radians per volt. The schematic of the interferometers used with the OPD is shown in Figure 3.4.

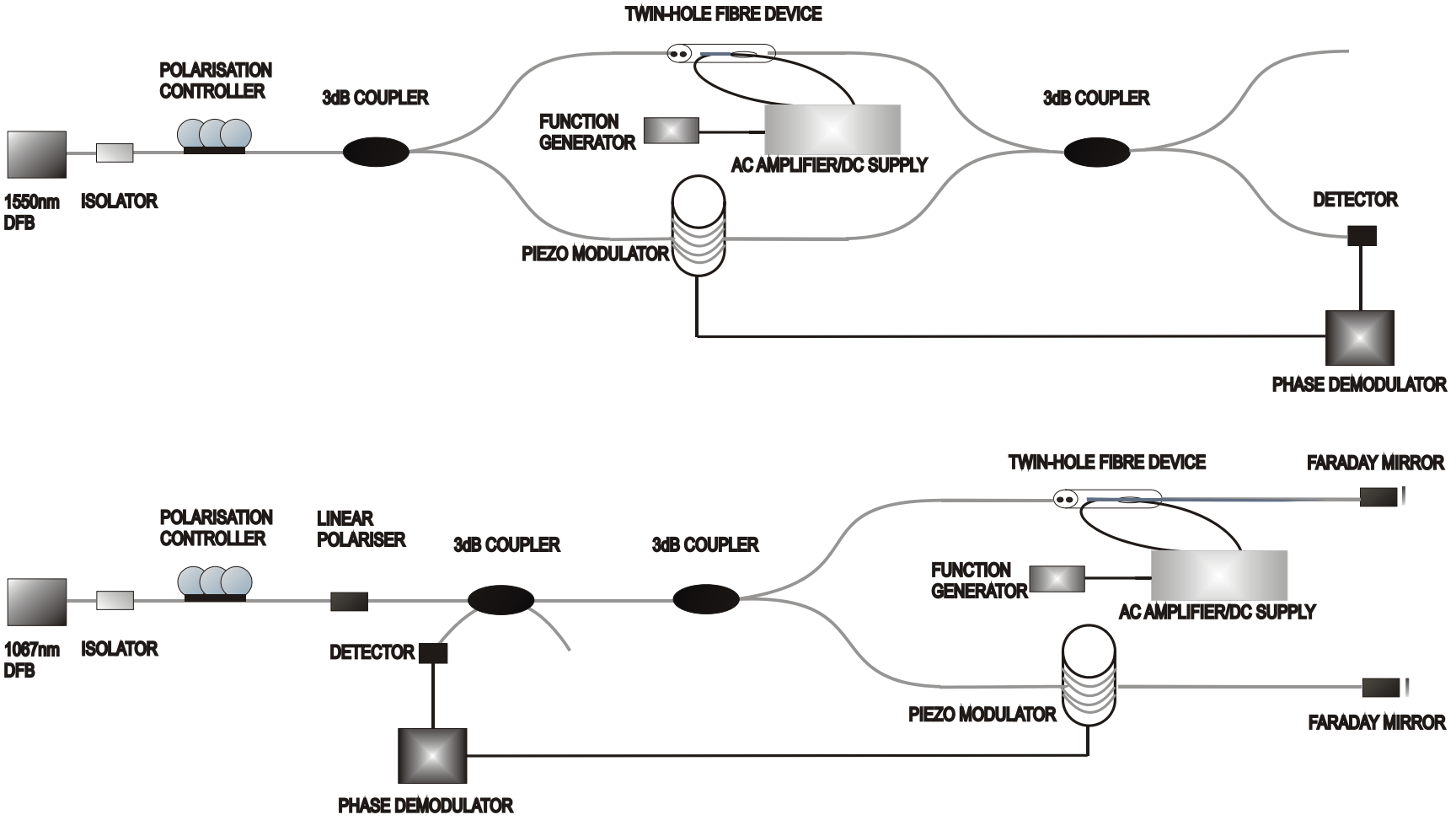

Figure 3.4 (a) Mach-Zehnder interferometer as constructed for the measurements with the commercial phase demodulator (b) Michelson interferometer with Faraday mirrors

3.2.5 Michelson Interferometer

A Michelson interferometer (MIC) was also constructed using 1060nm singlemode fibre (Corning Hi1060) and components made from the same fibre, the schematic of which is shown in Figure 3.4 (b). The reasons for the construction of the Michelson interferometer were twofold: 1. Measurement of the EO coefficient at 1060nm for comparison with measurements at 1550nm, 2. Improve OPD stability and phase extraction using a polarisation insensitive interferometer. The use of Faraday mirrors as a substitute for standard mirrors has been shown to overcome polarisation drift issues arising from environmental changes in the interferometer, lowering noise considerably [6]. The $1067nm$ interferometer was constructed as shown in Figure 3.4 (b). The input state of polarisation (SOP) to the Faraday mirrors (FRM) is rotated by $45°$ by the Faraday rotator and a further $45°$ after reflection from the end mirror. The birefringence of the fibre acts on the reflected beam to '*unwind*' the polarisation drift caused within the fibre in transmission. This hold for both paths of the interferometer and consequently the two reflected beams meet again at the $3dB$ coupler at same polarisation as each other but rotated exactly $90°$ from the initial SOP. Thus it is clear that the interferometer uses both orthogonal polarisation states and as a result, the measurement of the phase change in the twin-hole fibre device is an average of both polarisation states. Consequently it is not possible to make separate measurements of the two orthogonal components (r_{31} and r_{33}). This is essentially a polarisation insensitive interferometer that overcomes variations in fringe contrast resulting from arbitrary polarisation changes in the two arms of the interferometer.

3.2.6 Comparison of measurement techniques

All three interferometers described above were used extensively with several hundred devices made with wires inserted manually into the holes as described in Section 3.1.3. The measurement of the EO coefficient is dependent on the AC field in between the wires and for which the separation between the wires must be known. The AC field alone is insufficient to bring the wires together, however the wires were assumed to be together against the sides of the holes when the DC field was applied. This assumption was made for the measurement of the EO evolution and also for the measurement of the residual SON. In a collaboration with the ACREO group, a number of devices were

fabricated with alloy (Au/Sn) filled holes and poled. These devices were then tested with the three interferometers described in the preceding section. Figure 3.5 shows the measurement of the EO coefficient taken every 2 seconds over 60 seconds for one of the devices fabricated at ACREO with each of the interferometers. The black line represents the measurement made with the first interferometer while the red and blue lines represent the measurements of the 1550nm MZ and 1067nm MIC interferometers made with the OPD.

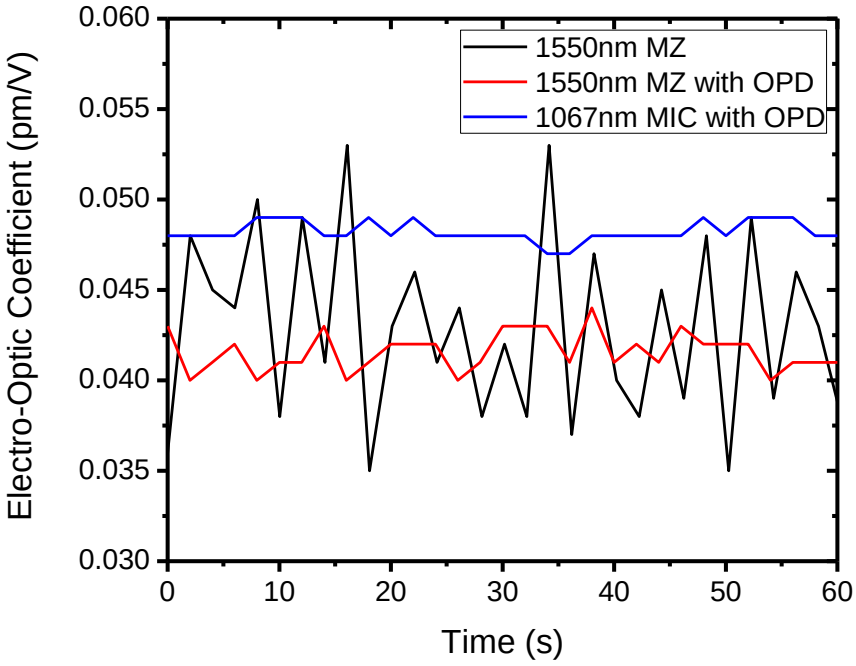

Figure 3.5 Measurements of the EO coefficient taken with the three interferometers over 60 seconds measurement time

The improvement made by using the OPD with the 1550nm MZ interferometer is clearly obvious from Figure 3.5 with a $5x$ improvement in the error (Table 3.1). The use of the Faraday Michelson interferometer improves the error a further $\sim$2-fold as seen in Table 3.1. This improvement is attributed to the polarisation insensitive nature of this interferometer and was confirmed by the extremely stable OPD input signal servo. The filled devices used in these measurements were made from a fibre (ACREO-2) with electrodes positioned very close to the core. When the holes were filled with the alloy, the transmission losses were seriously exacerbated. The propagation losses in a fibre (ACREO-2) of 0.2 NA was measured to be $0.33dB/cm$ and $0.82dB/cm$ for a 0.1 NA fibre (FORC-2). This will undoubtedly impact on the fringe visibility of the interferometer as a result of optical power imbalance between the two arms. A variable

optical attenuator can be used in the reference arm to match the power between the two arms. This is expected to lower the error in measurement further.

Table 3.1 EO coefficient measurements made with the three different interferometers

Measurement system	**Measured EO coefficient (pm/V)**	**Error**
1550nm MZ	0.043	0.005
1550nm MZ with OPD	0.042	0.001
1067nm MIC with OPD	0.048	5.84×10^{-4}

The measurements of the EO coefficient at the two wavelengths indicate an inverse relationship between the two. This difference is attributed to the difference in the mode field areas of the two wavelengths. In the device used in these comparative measurements of the interferometers, the longer wavelength has a mode field area about ~1.3 times that of the shorter wavelength and as a result is spans a greater area of the cladding. Hence the measurement of the EO coefficient is an average of a greater area for the longer wavelength interferometer. This inverse relationship has also been independently observed by another group [7].

3.3 UV periodic erasure

The $\chi^{(2)}$ grating for quasi-phase matching was fabricated by local erasure of the nonlinearity through exposure to UV light. This technique is referred to as periodic UV erasure (PUV). The UV light serves to ionise defect states and release trapped electrons. These electrons act to shield and neutralise the frozen-in field in the UV exposed regions [8]. The periodic nonlinearity was created point-by-point using a focussed output from a frequency doubled argon-ion laser operating at $244nm$. This was performed using an existing system used for the fabrication of long period fibre gratings (LPFG). The schematic of the erasure system is shown in Figure 3.6.

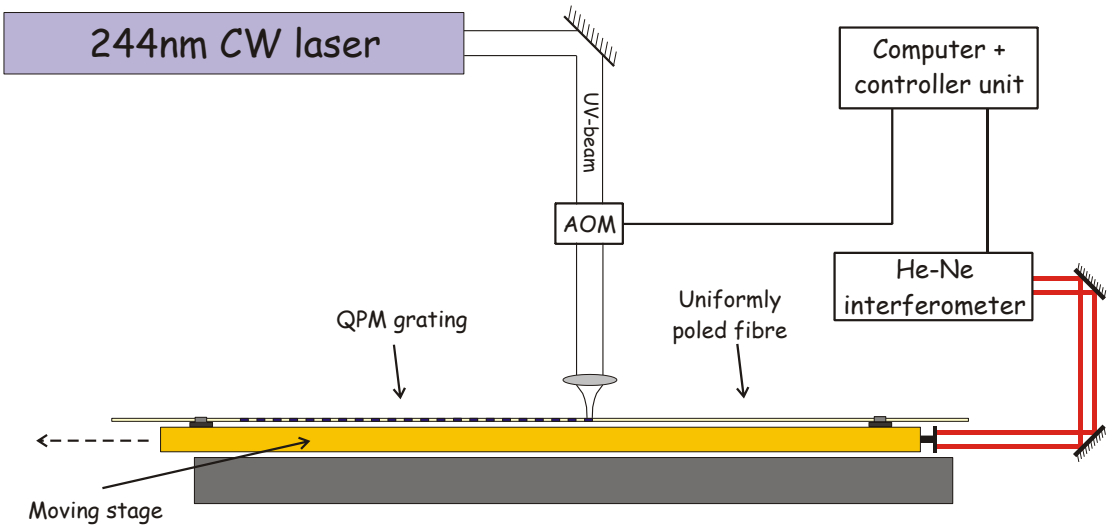

Figure 3.6 Schematic of the UV erasure system used for the fabrication of the PPSF

The poled fibre is mounted on the vibration controlled translation stage and held firmly using two clamps. An acousto-optic modulator (AOM) is used to control the exposure of the uniformly poled fibre to the UV light. Through control of the speed of the stage and the switching rate of the AOM, the period of the PPSF can be regulated. Specialised structures in poled fibre (e.g. chirping) can be also be fabricated by controlling the speed of the stage and the AOM switching. The position of the stage is accurately tracked using a free-space Michelson interferometer with sub-nanometre accuracy in the displacement measurement. The optimum erasure fluence was determined to be in the range $10 - 15 J cm^{-2}$ for the fibres used. This range was determined using a very large number of PPSF devices fabricated at different levels of fluence. The required erasure fluence is two orders of magnitude lower than that typically used for Bragg grating fabrication, suggesting that low power UV lamp sources can be used for this task. The duty cycle of the erasure beam is calibrated based on the focussed spot size and the required QPM period to obtain the 50% duty cycle between the domain boundaries.

3.3.1 Quasi phase matching period

The response of a dielectric medium to electromagnetic waves is frequency dependent. This phenomenon, referred to as chromatic dispersion, manifests itself through the frequency dependence of the refractive index. The origin of this phenomena is related to the characteristic resonance frequencies at which the medium absorbs the electromagnetic radiation through oscillations of bound electrons [9]. The refractive

index for a specific wavelength can be calculated approximately using the Sellmeier equation [9];

$$n^2(\lambda) = 1 + \sum_{i=1}^{3} \frac{a_i \lambda^2}{\lambda^2 - b_i} \quad (3.24)$$

Where a_i and b_i are the Sellmeier coefficients, which for fibres are dependent on the core constituents and determined experimentally by fitting the measured dispersion curves to Equation 3.24 with $m = 3$. Dispersion in optical fibres is detrimental for second harmonic generation as the fundamental and the generated second harmonic travel at different speeds in the fibre given by $c/n(\omega)$. As a result there is a continuous forward and backward transfer of power from the fundamental to the second harmonic fields. The transfer of power between the two fields is reversed each time the fundamental and the generated second harmonic are π degrees out of phase. This is defined as the coherence length and is given by $l_c = {}^{\pi}/_{\Delta k}$. Thus after one coherence length l_c, the generated second harmonic decreases and reaches zero. For wave vector $\Delta k = 0$, a continuous transfer of power from fundamental to second harmonic is attained. This is only possible if $n^{\omega} = n^{2\omega}$, which is not generally possible due to dispersion. However phase matching between the fundamental and second harmonic can be achieved through phase slippage of the two co-propagating waves. In crystals such as lithium-niobate this can be achieved through domain inversion whereby the sign of $\chi^{(2)}$ is reversed every coherence length. It is also possible to achieve SHG through birefringent phase matching and modal phase matching in crystals. In fibres quasi phase matching can be achieved through periodically nullification of the induced nonlinearity. Figure 3.7 shows the growth of the second harmonic power for perfectly phase-matched, quasi-phase-matched through domain inversion, quasi-phase-matched through periodic nullification and non-phase-matched waveguides.

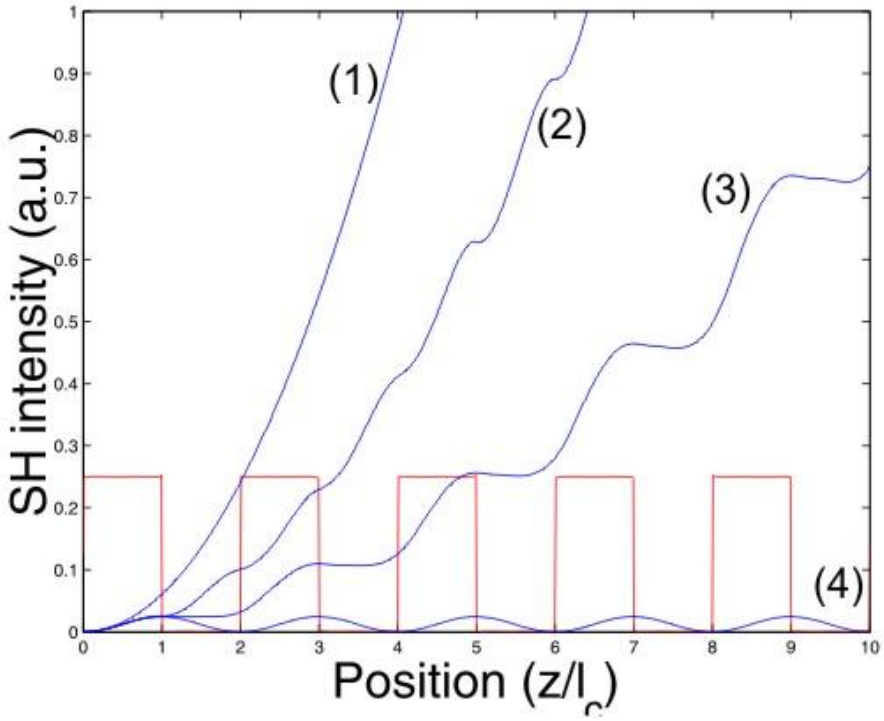

Figure 3.7 Intensity of SHG along propagation direction for; (1) perfect phase matching, (2) quasi phase matching through domain inversion (+1, -1) (3) quasi phase matching through periodic nullification (+1, 0) (4) non phase matching

Thus to compensate for the phase mismatch between the co-propagating fundamental k_ω and second harmonic $k_{2\omega}$ wavevectors ($\Delta k = k_{2\omega} - 2k_\omega$),

$$\Delta k_G = \Delta k \quad (3.25)$$

Where the wavevector of the periodic grating for QPM is given by

$$\Delta k_G = \frac{2\pi}{\Lambda_{QPM}} \quad (3.26)$$

Since $k_\omega = \frac{2\pi n^\omega}{\lambda^\omega}$, $k_{2\omega} = \frac{2\pi n^{2\omega}}{\lambda^{2\omega}}$and $\lambda^\omega = 2\lambda^{2\omega}$, the period for phase matching for SHG is

$$\Lambda_{QPM} = \frac{\lambda^\omega}{2(n^{2\omega} - n^\omega)} \quad (3.27)$$

There were some uncertainties in determining the refractive index relation with wavelength as dispersion was not experimentally measured in any of the fibres used for this present work. In the early part of this work, the effective indices were determined experimentally by fibre Bragg grating (FBG) inscription into the specialty fibres at the fundamental wavelength and calculating n^ω and subsequently $n^{2\omega}$ through

extrapolation. The accuracy of this technique was limited as $n^{2\omega}$ was not experimentally determined, although possible. However, once an approximate relationship between the QPM period and fundamental wavelength was established, several PUV erasures at a range of different periods (multi-period devices) were made to generate a more accurate relationship between the two quantities.

In the last fibre fabricated for this present work, a refractive index profiler was sourced and the index profile of the fibre cross section was measured and used to determine the wavelength dependence of the refractive index using a mode propagation software. The erasure parameters of duty cycle and fluence of the UV beam were optimised (separately) through the fabrication of multi-period PPSFs.

3.4 Characterisation sources

For the characterisation of the PPSFs an assortment of laser sources were used. For the characterisation of the multi-period devices and for the initial characterisation the PPSF devices fabricated earlier on in this present work, the supercontinuum generated from a dispersion shifted fibre (DSF) pumped by a master oscillator power amplifier (MOPA) was utilised. The MOPA source is explained in the following section. For the characterisation of the PPSF devices fabricated for the frequency doubling of wavelengths around the $1\mu m$ range, an optical parametric generator (OPG) pumped by $532nm$ light from a frequency doubled Nd:YVO_4 (Neodymium-doped Yttrium Vanadate) laser system (*Lumera Super Rapid*) operating at $10ps$ pulse duration and $250kHz$ repetition rate. At $532nm$ the system produces $\sim 5W$ of average power or $2MW$ peak power. The wavelength of the OPG can be tuned over the range $0.6 - 2.5\mu m$. The spectra of these broadband sources are shown in Figure 3.8.

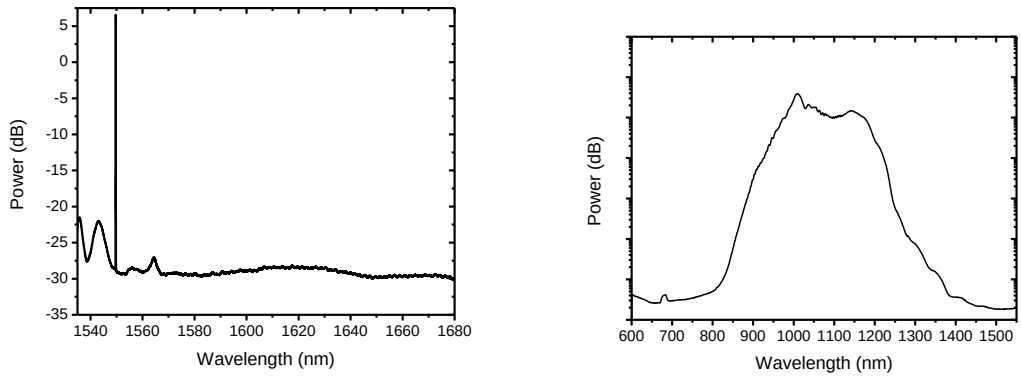

Figure 3.8 (a) Supercontinuum generated by a DSF pumped with MOPA laser (b) Spectrum of Nd: YVO_4 pumped OPG (Signal output)

A CW external cavity wavelength tunable diode laser (*Tunics Plus 3642 HE CL*) source of $\sim 9-10mW$ power was available for the characterisation of the PPSF devices in the later stages of this present work. This laser with its wide wavelength tuning range of $1500-1640nm$, very narrow linewidth ($150kHz$), $1pm$ wavelength setting resolution and sufficient output power to generate SH power in the nano-watt level or above, was found to be ideal for the initial characterisation of the PPSF. This system was utilised to determine the phase matching wavelength, generate the second-harmonic tuning curves and for the characterisation of the chirped period devices fabricated with the FORC-2 fibre.

3.4.1 Maximum second harmonic conversion

To demonstrate the highest conversion efficiencies possible, two fibre lasers based on the MOPA configuration were employed. In the MOPA configuration a light from a low power seed laser (*Tunics Purity*) is amplified in one or more amplifiers. To achieve higher powers, the amplifiers are cascaded usually with a filter to eliminate the excess amplified spontaneous emission (ASE) from the preceding amplifier. The first one fabricated by the high power fibre lasers group at the ORC had an externally modulated, wavelength tunable diode laser source amplified in two stages by a pre- and power-amplifier as shown in Figure 3.9 (a).

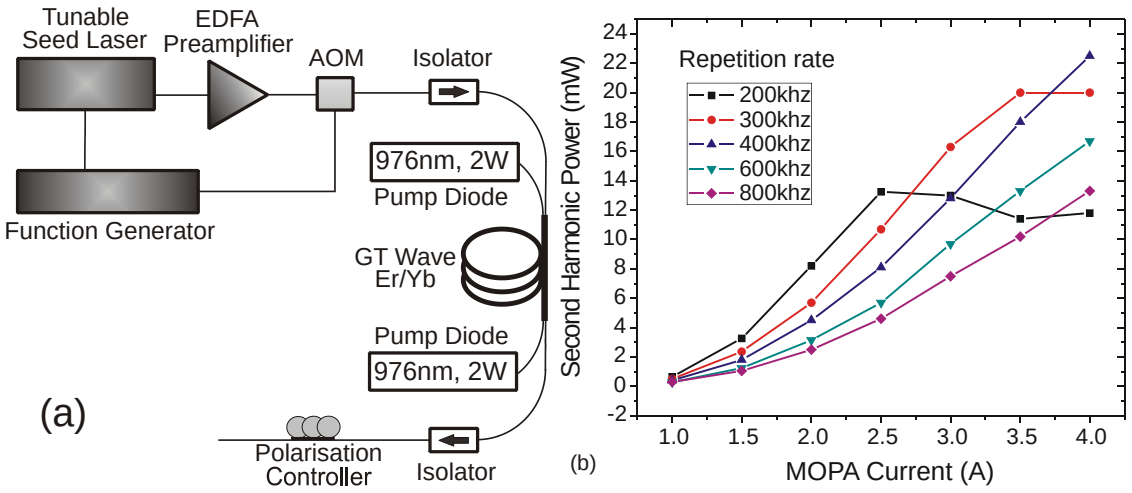

Figure 3.9 (a) ORC MOPA laser system (b) Characterisation of device ASCR141 with the MOPA for varying repetition rates, pulse duration fixed at 5ns

In this system, the tunable seed laser was directly modulated with a function generator typically with a pulse duration of $5ns$ and a repetition rate optimised so that the linewidth of the MOPA matches that of the bandwidth of the PPSF device. The seed laser is firstly amplified by a core-pumped erbium doped fibre amplifier (EDFA). The output from the first amplifier stage is then time-gated with a synchronised acousto-optic modulator (AOM) before being amplified further by a cladding pumped erbium/ytterbium doped fibre amplifier (EYDFA) (bi-directionally pumped *GT-wave* fibre [10]). The AOM drive signal was provided by the second output of the function generator with suitable amplification. A polarisation controller is added at the output of the MOPA laser to control the input polarisation to the PPSF device.

Figure 3.9 (b) shows measured SH power as a function of the current setting for the power amplifier for one of the PPSF devices (ASCR141) for a range of repetition rates. The average power of the source was not observed to alter for changing repetition rates. However, the lower repetition rates produce peak powers sufficient to cause linewidth broadening of the MOPA through the onset of self phase modulation (SPM). When the linewidth exceeds the acceptance bandwidth of the PPSF device, the power available for SH conversion is limited. This is evidenced by saturation and *roll-off* in the SH power as seen in Figure 3.9(b) for the 200 and $300kHz$ cases. The optimised average conversion efficiency for this particular device was obtained at a repetition rate of $400kHz$. This indicates that the linewidth of the MOPA source is within the acceptance bandwidth of the PPSF device at this repetition rate.

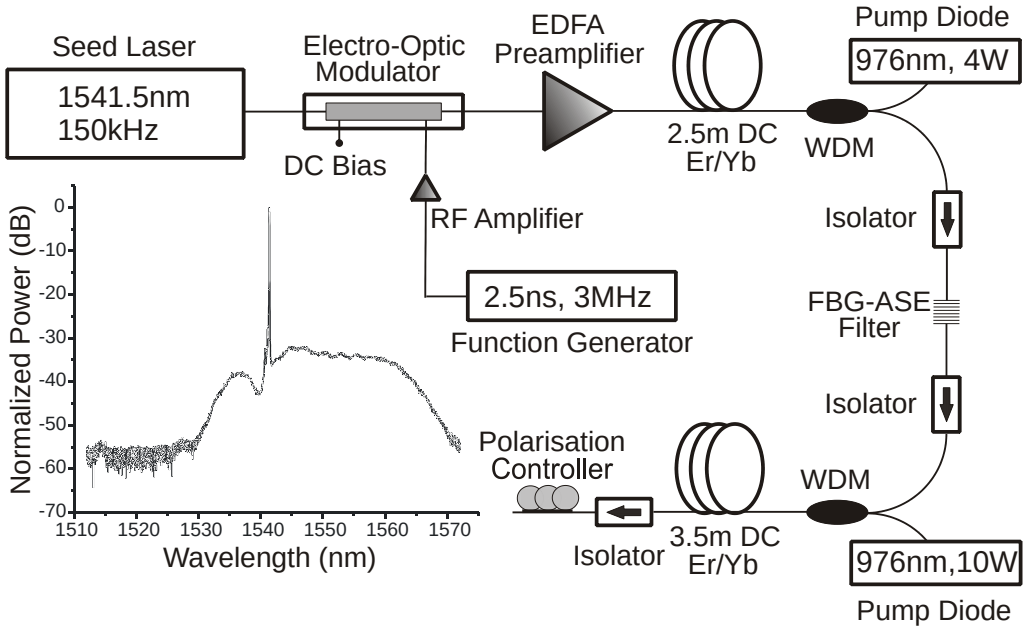

Figure 3.10 Multitel MOPA laser system

The schematic of the second MOPA system used for this present work is shown in Figure 3.10. This system was constructed by collaborators at Multitel, Inc, Belgium. A narrow linewidth ($150kHz$) seed laser is externally modulated using an electro-optic modulator (EOM) before being amplified with a low gain core-pumped EDFA. The amplified output from the EDFA is further amplified in two further stages by high power cladding-pumped amplifiers. An FBG filter is used after the first high power amplifier to remove the ASE from the signal before further amplification by the final stage amplifier. A maximum average power of $1.8W$ was measured at the optimum pulse duration ($2.5ns$) and repetition rate ($3MHz$).

3.5 Conclusions

In this chapter, the experimental techniques employed in this present work were described. The fabrication of the specialty twin-hole fibre and the associated problems were explained. In Section 3.2, the interferometric techniques employed for the *in-situ* measurement of the induced nonlinearity through the measurement of the EO coefficient was discussed. A range of improvements were implemented, resulting in a 10-fold improvement in error from the first measurement system constructed. The realisation of QPM for SHG through periodic UV erasure was explained. Finally a description of the laser sources used for the characterisation and demonstration of high conversion efficiencies in PPSFs was given.

3.6 References

1. Macchesney, J.B., *Materials and Processes for Preform Fabrication - Modified Chemical Vapor-Deposition and Plasma Chemical Vapor-Deposition.* Proceedings of the IEEE, 1980. **68**(10): p. 1181.
2. Mezzapesa, F.P., et al. *Second-order nonlinearity profile in thermally poled twin-hole fibre*. in *Conference on Lasers and Electro-Optics/International Quantum Electronics Conference and Photonic Applications Systems Technologies*. 2004: Optical Society of America.
3. Myren, N., et al., *Wide wedge-shaped depletion region in thermally poled fiber with alloy electrodes.* Optics Express, 2004. **12**(25): p. 6093.
4. Xu, W., *Thermally poled fibre devices, PhD thesis*, in *Department of Physics*. 1999, Sydney University: Sydney, Australia.
5. Dandridge, A., A.B. Tveten, and T.G. Giallorenzi, *Homodyne Demodulation Scheme for Fiber Optic Sensors Using Phase Generated Carrier.* Ieee Journal of Quantum Electronics, 1982. **18**(10): p. 1647.
6. Kersey, A.D., M.J. Marrone, and M.A. Davis, *Polarization-Insensitive Fiber Optic Michelson Interferometer.* Electronics Letters, 1991. **27**(6): p. 518.
7. Michie, A., *Sensing and interferometry, including design and characterisation of special optical fibres, PhD thesis*, in *Optical Fibre Technology Centre*. 2008, University of Sydney: Sydney.
8. Corbari, C., *Development of Non-Linear Waveguide Devices for Optical Signal Processing, PhD thesis*, in *Optoelectronics Research Centre*. 2005, Southampton University: Southampton, United Kingdom.
9. Agrawal, G.P., *Nonlinear fiber optics*. 2 ed, ed. P.F. Liao, P.L. Kelley, and I. Kaminow. 1995, San Diego, CA: Academic Press.
10. Yla-Jarkko, K.H., et al., *Low-noise intelligent cladding-pumped L-band EDFA.* Ieee Photonics Technology Letters, 2003. **15**(7): p. 909.

Chapter 4: Second harmonic generation in periodically poled silica fibres

Since the beginning of this present work, a total of five specialty twin-hole fibres were extensively tested and optimised, primarily for the purpose of second harmonic generation. The very first specialty fibre (ORC-1) used had a hole-to-hole separation of $10\mu m$, a germanium rich ($16.8mol\%$) core and a very high NA of 0.28. The fibre was found to be inconsistent over the length and it was generally very difficult to reproduce the same wavelength for quasi-phase-matching (QPM) even over a relatively short length. The irregularities leading to variations in the refractive index can be caused by diameter variations during fibre pulling and deviations in the positioning of the holes with respect to the core. The high NA of the ORC-1 fibre further impinges on the tolerances required for QPM second-harmonic generation (SHG). The relationship between the fabrication tolerances of the fibre with the wavelength, NA and core size is scrutinised at the end of this chapter.

The ORC-1 fibre was used to demonstrate the frequency doubling of an all-fibre MOPA source operating at a repetition rate of $100kHz$, pulse duration of $10ns$ and $108W$ peak power. An average conversion efficiency of 2.4% was demonstrated, representing a normalised conversion efficiency of $2x10^{-4}\%/W$, the highest at the time for periodically poled silica fibres [1]. The same fibre was used in the first demonstration of a tunable frequency doubler with a tuning range of $27.8nm$ achieved with a highly efficient, highly durable compression tuning package [2]. Over the years following the unfortunate loss of the fibre fabrication facility at the ORC, four new fibres were procured from two collaborators, one from ACREO, Sweden and the other from FORC, Russia. A considerable amount of time was dedicated to the four fibres, particularly in optimising the techniques of thermal poling and UV erasure for the generation of second harmonic (SH) light. The results of each of these fibres are presented in this chapter. Some repetitive results, such as that of the thermal poling optimisation and SH tuning profiles are omitted for some fibres. The devices fabricated for poling and periodic UV erasure are numbered with the prefix "ASC" for the ACREO fibres and "ASCR" for the FORC fibres. A comparison of performances

between the fibres used for this present work and between previously published results is given at the end of the chapter.

4.1 ACREO Fibres

In this section the results of the fibres fabricated at ACREO are presented. The fibres were fabricated from the same preform with a second mode cut-off chosen for the frequency doubling of fibre lasers operating in the erbium or erbium/ytterbium gain range. Two fibres were delivered, ACREO-1 (June 2006) and ACREO-2 (March 2007). Table 4.1 provides a side-by-side comparison of the key parameters for these fibres and the microscope images are shown in Figure 4.1. The length over which the drawing induced twist changes by $\sim 90°$ was measured on average to be $20cm$ and $40cm$ for ACREO-1 and ACREO-2, respectively.

Table 4.1 Key parameters of ACREO-1 and ACREO-2 fibres

Fibre name	ACREO-1	ACREO-2
Cut-off wavelength (nm)	1480	1305
Outer diameter (μm)	125	133
Hole-to-hole separation (μm)	15.7	13.2
Core radius (μm)	2.83	2.50
delta n	0.012	0.012
NA	0.2	0.2
Overlap area, A_{OVL} (μm^2)	31.4	28.9

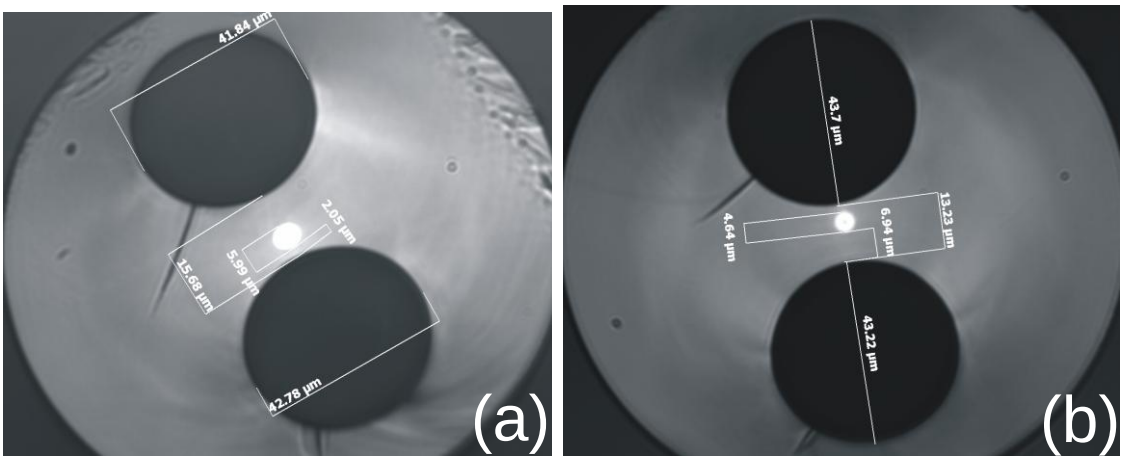

Figure 4.1 Microscope pictures of (a) ACREO-1 fibre (b) ACREO-2 fibre

4.1.1 Quasi phase matching period – ACREO-1

To determine the wavelength dependence of the refractive index, a fibre Bragg grating (FBG) was inscribed in the ACREO-1 fibre using the phase mask ($\Lambda = 1058\mu m$) technique and a continuous wave frequency doubled argon ion laser. The transmission profile of the FBG is shown in Figure 4.2 (a). The two peaks indicate the birefringence of the ACREO-1 fibre. Using the Bragg wavelength, the effective index (n_{eff}) at $1550nm$ was calculated and the effective index at $775nm$ was estimated through extrapolation from Sellmeier equation for germanium-doped silica. This technique gives a ball park figure for the QPM period for frequency doubling of a fundamental wavelength in the range 1530-1560nm (gain range of MOPA). Due to the uncertainty in the estimation of the effective index at the SH wavelength, many devices were fabricated with large steps in the QPM period to obtain the relationship between QPM period and fundamental wavelength in this fibre. It was not necessary to determine the dispersion curve for the fibre, as the relationship between the QPM period and the fundamental wavelength was found to be more or less linear in the wavelength regime (erbium/ytterbium gain range) for which these PPSF devices were fabricated.

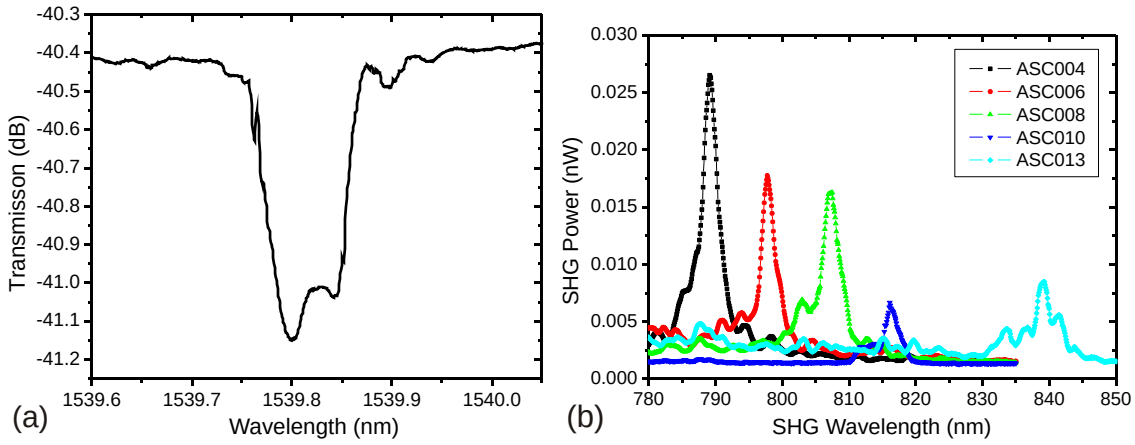

Figure 4.2 (a) Transmission profile of the fibre Bragg grating inscribed in the ACREO-1 fibre (b) Second harmonic generation in 12cm long periodically poled devices

The ACREO-1 devices in the very first batch were $12cm$ in length. The QPM period was varied from $53.4\mu m$ to $54.9\mu m$ in $0.3\mu m$ steps. Each device was characterised with the master oscillator power amplifier (MOPA) source operating at $100kHz$ repetition rate and $5ns$ pulse duration. The MOPA source was operated at full power, at which the spectrum of the source broadens through the onset of self phase modulation (SPM). This broadband spectrum was launched in each fibre device and the SH spectrum recorded with an optical spectrum analyser (OSA). As can be seen from

Figure 4.2 (b), none of the devices were suitable for frequency doubling in the high gain region of the MOPA. However, with the wavelength-period relationship obtained from this data, the QPM period for conversion in the high gain region was extrapolated.

4.1.2 Quasi phase matching period – ACREO-2 fibre

In ACREO-1 fibre 5 separate devices were used to determine the relationship between the QPM period and fundamental wavelength. In the second ACREO fibre delivered, 3 sections (6cm length each) of slightly varying periods were fabricated in each fibre, yielding a total of 6 points for the QPM period-wavelength relationship, as seen in Figure 4.3. Again, as with the ACREO-1 fibre, the linearity of this relationship over the short wavelength range was used to determine the QPM period for a given wavelength.

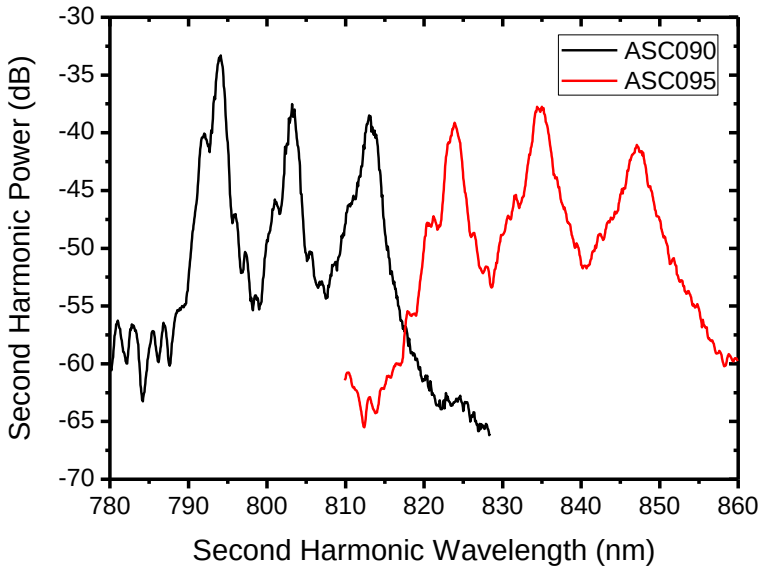

Figure 4.3 Multi-period devices for the determination of QPM period-wavelength relationship (RBW 0.1nm)

As with the ACREO-1 fibre devices, the characterisation of the multi-period gratings was carried out using the supercontinuum output from the MOPA fibre laser source. The SH spectra as measured with the OSA are seen in Figure 4.3. When the ASC090 device was characterised, setting the pulse duration to $5ns$ and the repetition rate to $50kHz$ provided sufficient power to visualise the generated SH peaks corresponding to the 3 periods with an OSA. However, in the device ASC095, the generated power of the supercontinuum was insufficient to generate the minimum SH power measurable by the OSA. To overcome this limitation, the bandwidth of the supercontinuum was

extended by increasing the peak power of the MOPA source. The peak power was increased $2.5X$ by reducing the repetition rate of the MOPA source to $20kHz$ while the pulse duration was maintained at $5ns$. The profiles of the SH peaks observed with the extended bandwidth are shown in Figure 4.3.

4.1.3 Frequency doubling

Several batches of devices from both ACREO fibres were poled and periodically erased with the frequency doubled argon-ion (FRED) laser. This technique is described in Section 3.3. The earliest devices were poled with the longest available heater at the time ($13cm$). Later longer heaters were custom fabricated ($21cm$ and $41cm$) in the interests of extending the interaction lengths for improved conversion efficiencies. A list of the best performing devices from each of the batches made is given in Table 4.2. All ACREO devices were characterised with the tunable ORC-MOPA system described in Section 3.4.1. The MOPA was typically operated at a repetition rate of $413kHz$ and pulse duration of $5ns$. The average power produced by the MOPA was wavelength dependent, averaging $\sim 700mW$. The SH power and tuning profile was measured by simultaneously scanning the wavelength of the seed laser for the MOPA through a range of wavelengths centred around the phase matching wavelength of the PPSF device and measuring the generated SH power. The SH power was measured using a silicon detector head (Newport 818-SL) and power meter (Newport 2936-C). The splice loss between the ACREO fibres and the standard telecommunications fibre (SMF-28) was typically $\sim 1dB$ at the fundamental and $\sim 2dB$ at the SH wavelength. The columns titled "SH adjusted power" and "FH power utilised" contain adjusted values based on the measured splice loss for each PPSF device.

Since the devices were of different length the normalised conversion efficiency, η_2 ($\%W^{-1}cm^{-2}$) or the nonlinear coefficient d_{33} calculated from η_2 can be used to compare between the devices. The mean nonlinear coefficient for the best performing ACREO-1 and ACREO-2 devices shown in Table 4.2 are $0.026 \pm 0.007pm/V$ and $0.007 \pm 0.002pm/V$, respectively. The variations in the nonlinearity between devices made from the same fibre are attributed primarily to the thermal poling process, in particular the random positioning of the inserted wires during poling and the influence of the heater block on the applied poling field. It is also possible that the devices were

at different stages of their initial fast decay (Introduced in Section 2.3.3), consequently contributing to the differences in the η_2 and d_{33} values. The decay of the induced nonlinearity in the poled ACREO fibres was realised to be significant when the SH generated in a PPSF device was observed to fade over a relatively short period of time. The periodic UV erasure conditions were identical for all ACREO fibre devices.

Table 4.2 List of PPSF device parameters for the ACREO fibres

Fibre ACREO	Batch No.	Device Name	Length (cm)	Period (μm)	Fundamental Wavelength (nm)	BW (nm)	SH adjusted power (mW)	FH Power Utilised (mW)	Average Conversion (%)	Peak Conversion (%)	Normalised Conversion η_1 ($\%W^{-1}$)	Normalised Conversion, η_2 ($\%W^{-1}cm^{-2}$)	Nonlinear Coefficient d_{33} (pm/V)
1	2	ASC003	13	52.85	1551.2	1.00	10.08	378.79	2.66	3.80	0.021	1.23×10^{-4}	0.031
1	2	ASC016	12	52.75	1545.2	1.10	3.47	421.91	0.82	1.17	0.006	3.99×10^{-5}	0.018
1	3	ASC018	9	52.80	1547.0	1.33	4.01	477.86	0.84	1.20	0.005	6.40×10^{-5}	0.022
1	3	ASC019	12	52.70	1543.1	1.00	12.71	415.85	3.06	4.37	0.022	1.51×10^{-4}	0.034
1	3	ASC021	8	52.55	1536.9	1.50	6.82	560.88	1.22	1.74	0.006	9.99×10^{-5}	0.028
1	7	ASC091	20	52.75	1547.4	0.70	49.93	453.24	11.02	15.74	0.072	1.79×10^{-4}	0.037
1	7	ASC091*	20	52.75	1547.3	0.77	33.98	453.24	7.50	10.71	0.049	1.22×10^{-4}	0.031
1	7	ASC092	20	52.80	1551.1	0.73	16.36	487.23	3.36	4.80	0.020	5.08×10^{-5}	0.020
1	7	ASC093	20	52.80	1549.9	0.65	29.10	427.18	6.81	9.73	0.047	1.18×10^{-4}	0.030
1	7	ASC094	20	52.85	1552.5	0.82	16.29	453.24	3.59	5.13	0.023	5.85×10^{-5}	0.021
1	8	ASC099	24	52.80	1550.7	0.56	16.17	464.57	3.48	4.97	0.022	3.84×10^{-5}	0.017
2	2	ASC110	20	51.8	1556.1	0.61	2.58	422.66	0.61	0.87	0.004	1.07×10^{-5}	0.009
2	2	ASC112	20	51.6	1546.7	0.61	5.07	442.17	1.15	1.64	0.008	1.91×10^{-5}	0.012
2	2	ASC115	20	51.5	1541.4	0.62	1.85	455.18	0.41	0.59	0.003	6.59×10^{-6}	0.007
2	2	ASC117	20	51.5	1541.5	0.63	1.90	435.67	0.44	0.63	0.003	7.38×10^{-6}	0.007
2	3	ASC153	24	51.4	1536.5	0.54	1.21	422.66	0.29	0.41	0.002	3.47×10^{-6}	0.005
2	3	ASC157	24	51.6	1546.0	0.53	1.44	422.66	0.34	0.49	0.002	4.13×10^{-6}	0.005

*Retested 24 hours later

In the case of device ASC091, the UV erasure was performed almost immediately after the thermal poling process before or during the onset of the initial fast decay. This device was poled under optimised conditions a very short time (~30 minutes) prior to erasure while the other devices from the same batch (No. 7) were made a few days earlier.

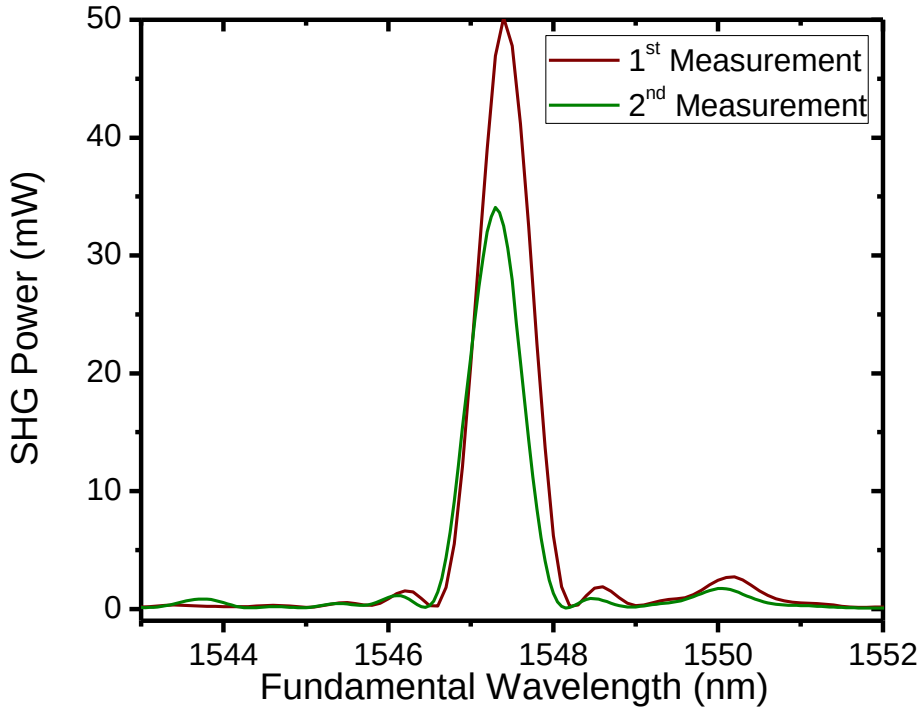

Figure 4.4 SH Tuning curve of device ASC091, characterised twice, 24 hours apart

The device was also tested immediately after periodic erasure and the SH profile for the first test is represented by the brown curve in Figure 4.4. An average SH power of $\sim 50mW$ was measured, corresponding to a conversion efficiency of 11%. At the time, the normalised conversion efficiency (η_1) of $0.072\%/W$ for this device represented the best value for a PPSF. However, about a day after the first measurement, the measured average power of the SH receded to $\sim 34mW$ and the average conversion efficiency to 7.5%. This measurement is represented by the olive green curve. This was the only device of the 21cm long batch of devices to show high conversion and subsequent fast decay. The decay of the SON observed in this device is attributed to the fast decay of the SON which typically occurs over a period of hours after poling. The shift in the phase matching wavelength could have occurred as a result of change in ambient temperature in the test laboratory or as a result of differences in the strain of the device during testing. The lower stable value was also obtained in the other devices and was

still detectable over a year after the initial measurements. The highly uniform, symmetrical shape of the SH profile illustrates the uniformity of the fibre and the precision of the domain boundaries achieved through the periodic UV erasure technique used in this present work.

Although even longer devices ($30cm$) were fabricated with the ACREO-1 fibre, higher conversion efficiencies were not obtained as the UV erasure beam was obstructed by twist over a section of the fibre and attempts to physically untwist the device during erasure were futile. The ACREO-2 devices were significantly less efficient in comparison to the ACREO-1 devices. The lower efficiency is attributed to the lower residual SON in the ACREO-2 fibre. Although the fibres were drawn from the same perform, there is a large difference in the induced SON. The preform used in the fabrication of the ACREO-1 fibre was re-sleeved before it was drawn again in to the ACREO-2 fibre. Thus it is likely that the impurity concentrations could have altered as a result of this. This disparity may also have been caused by the smaller hole-to-hole distance of the ACREO-2 fibre, leading to a faster and greater decay of the induced nonlinearity.

4.2 FORC fibres

In a collaboration with FORC, Russia, two specialty fibres were fabricated for this present work. The FORC-1 (October, 2007) and the FORC-2 (October, 2008) fibres had second mode cut-off values of $1060nm$ and $780nm$ respectively. Although these fibres were fabricated with the primary intention of frequency doubling for the generation of yellow and green light, the FORC-2 fibre was found to be suitable for frequency doubling of fibre laser sources in the infrared regime. Although the losses in the infrared regime are negligible for the typical lengths used, the PPSF devices had to be kept straight to minimise bend losses during frequency conversion. The FORC-1 fibre was used primarily to study the decay of the SON immediately after poling and for the frequency doubling of a CW bismuth doped fibre laser, whereas the FORC-2 fibre was used primarily for the frequency doubling of erbium/ytterbium doped fibre laser sources. The parameters of the two FORC fibres are presented in Table 4.3. The results for each of the fibres are presented separately as they were used for different purposes. The microscope images of the FORC fibres are shown in Figure 4.5. The

length over which the drawing induced twist changes by ~90° was measured on average to be $10cm$ and $30cm$ for FORC-1 and FORC-2, respectively.

Table 4.3 Key parameters of the FORC fibres

Fibre name	FORC-1	FORC-2
Cut-off wavelength (nm)	1060	780
Outer diameter (μm)	160	166
Hole-to-hole separation (μm)	11	31
Core radius (μm)	1.6	2.8
delta n	0.016	0.004
NA	0.21	0.105
Overlap area, A_{OVL} (μm^2)	25.6	156.0

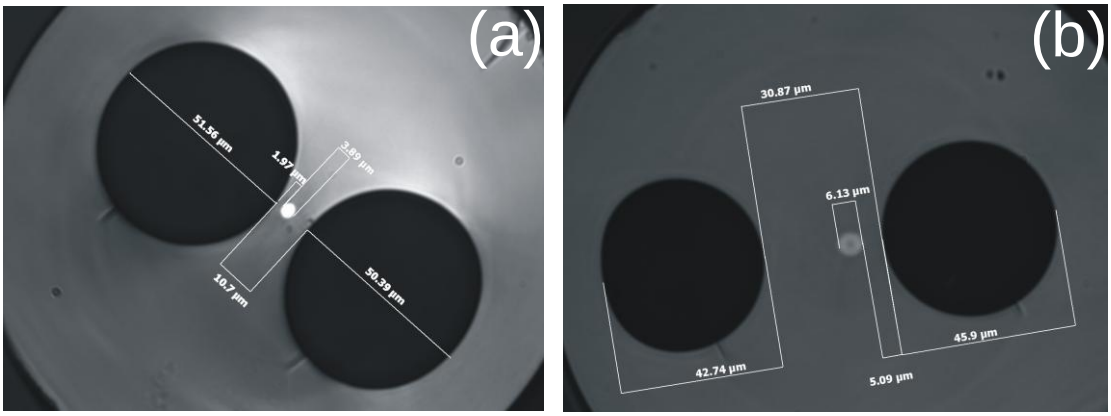

Figure 4.5 Microscope images of (a) FORC-1 fibre (b) FORC-2 fibre

4.2.1 Poling optimisation and stability of the induced nonlinearity- FORC-1 Fibre

The poling temperature for thermal poling of the FORC fibres was optimised. For the FORC-1 fibre several devices of $7cm$ wire overlap were made and poled with the $7cm$ long aluminium block heater at a range of temperatures while the poling voltage was kept to $3kV$ DC. The evolution of the electro-optic (EO) coefficient was measured in-situ for all devices using the Michelson interferometer (Section 3.2.5) and the commercial optical phase demodulator OPD (Section 3.2.4). Since the residual values vary with the optimum poling duration, a direct comparison is difficult to make, thus the highest value reached during poling was used to determine the optimum

temperature. Figure 4.6(a) indicates that the optimum poling temperature is at or around 260℃. All devices were poled until the growth of the EO coefficient saturated, however only the first 10 minutes of poling is shown for the sake of clarity and since the EO evolution did not deviate much ($< 0.01 pm/V$) from the value reached at 10 minutes. In the case of device ASCR071 poled at 200℃, the measured EO coefficient is seen to drop off after ~10 seconds of poling and then begins to increase again after ~30 seconds of poling. Prior to the commencement of the migration of ions and the formation of the depletion region the field is initially uniform across the sample. Once the depletion starts to form, the field strength is increased in this region as explained in Section 2.3.1. The core, positioned away from the edge of the hole, experiences a drop in the applied electric field. As the depletion region widens and makes its way into the core, the field in the core begins a gradual increase as seen in the evolution profile of the device poled at 200℃. This characteristic 'dip' in the evolution profile is not observed in the devices poled at higher temperatures as it occurs on a much faster time scale than the measurement interval of the EO coefficient, which was recorded every 2 seconds.

The value of the electro-optic coefficient immediately after poling with the heat and DC voltage removed can be deduced from the first points of Figure 4.6(b). For the FORC-1 fibre, the initial residual value of the EO coefficient measured immediately after poling was always higher than the value reached with the DC applied during poling. This interesting phenomenon was not observed with any other fibre used for this present work. This discrepancy in the result is thought to be related to the significantly smaller hole-to-hole distance of this fibre in comparison to the other fibres used. It is thought that as poling progresses, the internal field opposes the applied field.

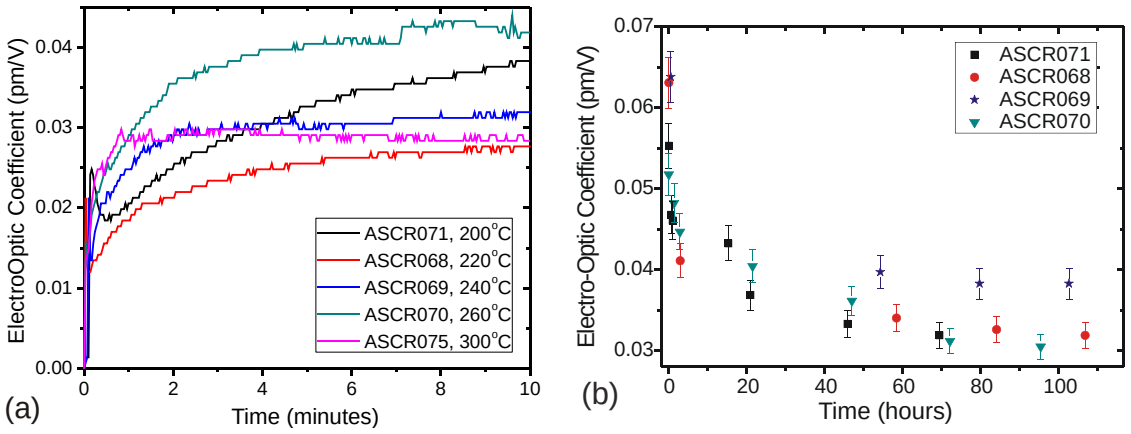

Figure 4.6 (a) Evolution of the EO coefficient during the first 10 minutes of poling (b) the decay of the EO coefficient after poling

The decay of the induced SON observed in the PPSF devices fabricated with the ACREO fibres highlighted the need for measurement of the decay after the poling process. However, the uncertainty in the position of the electrodes during the measurement of the residual EO coefficient implied that reliable measurements could not be made. Nevertheless an acceptable interim solution was devised whereby the DC voltage is switched on momentarily to bring the wire electrodes together before the measurement of the EO coefficient is taken. The electro-optic coefficient for four of the devices fabricated for the optimisation experiments was monitored over several days as shown in Figure 4.6(b). Each point is an average of several values of the EO coefficient measured after switching off the DC voltage. As with previous reports [3-4], the EO coefficient was observed to possess two decay components, a fast component occurring over $3-4$ hours and a slower component and subsequent stabilisation over a few days.

4.2.2 Frequency doubling of CW bismuth fibre laser

Bismuth doped fibre lasers operating in the range $1150-1300nm$ have been demonstrated. Fibres doped with bismuth are fully compatible with standard telecommunication fibres and therefore they are very promising for the development of telecommunication wideband fibre amplifiers in O-band ($1260-1360\,nm$). Yellow lasers are useful for a range of applications particularly in medicine and astronomy. However the lack of suitable gain media within the yellow band has hampered the development of such laser sources. Nonlinear frequency conversion using crystals has been employed to access yellow wavelengths. Frequency doubling of Yb solid-state lasers [5], frequency doubling of Raman-shifted Yb (Nd) lasers [6], and more recently frequency doubling of Bi-doped fiber lasers [7] have been demonstrated using KTP and PPLN non-linear crystals. Given the advantages of an all- fibre system, the PPSF was considered for the frequency doubling of CW bismuth fibre lasers.

In the collaboration with FORC, Russia, several $20cm$ long PPSF devices were fabricated at the ORC and sent for frequency doubling of the bismuth fibre laser source. The results of the experiments carried out at FORC are presented in this section.

The bismuth fibre laser used for frequency doubling was comprised of a $10m$ long bismuth doped silica fibre, pumped by a ytterbium fibre laser producing $5W$ of CW power at $1161nm$ over a $0.1nm$ linewidth. A $20cm$ long periodically poled FORC-1 fibre of period $34.15\mu m$ was spliced to the output of the fibre laser. Taking into account the $1.8dB$ splice loss only $3.3W$ of the fundamental light was available for frequency doubling to $580nm$. The spectra of the fundamental and the generated second harmonic are shown in Figure 4.7 (a) and (b).

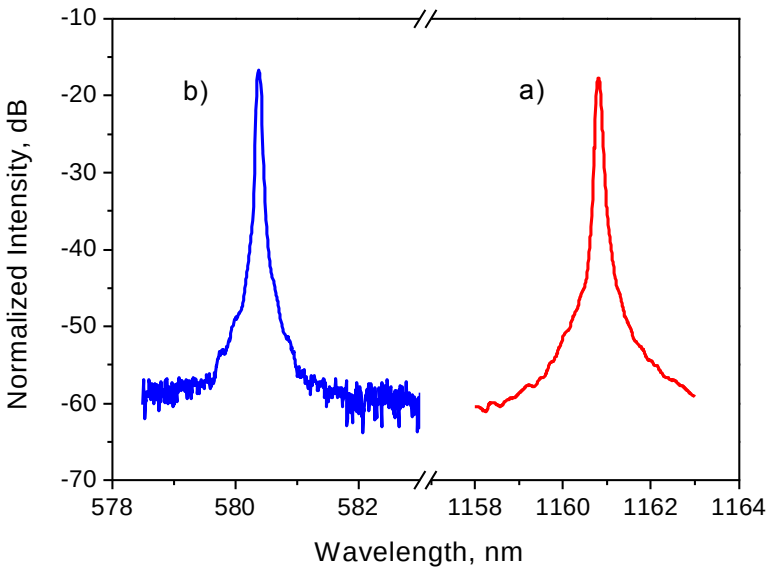

Figure 4.7 Spectra of the (a) bismuth fibre laser (b) second harmonic generation

The second harmonic output power was measured to be $295\mu W$ at the pig-tailed output translating to $447\mu W$ of actual generated power at $580nm$. The conversion efficiency was calculated to be $1.4 \times 10^{-4}\%$ [8]. The low efficiency is attributed to the low residual SON in the FORC-1 fibre after decay. The linewidth of the CW bismuth laser source used in this experiment was comparable to the acceptance bandwidth of the $20cm$ long PPSF device, thus the conversion efficiency could have suffered if there was a mismatch or misalignment in the spectral overlap.

4.2.3 Optimising fibre designs – FORC-2 fibre

All the fibres used thus far were identified to have a number of drawbacks associated primarily with the design. A number of observations were made from the studies on the residual electro-optic coefficients of the fibres and its decay. These were:

- The closer the core is to the anode, the larger the EO coefficient immediately after poling. However, a larger NA was required to minimise propagation losses from mode leakage into the anode hole. The higher NA possibly exacerbates the barrier like effect [9] at the core-cladding interface where the germanium doped core acts as a barrier for the migration of cations [10], lowering the induced SON.
- The residual values of the EO coefficient were observed to decay quite rapidly with upto 50% loss recorded in some devices fabricated from the FORC-1 fibre. This is the initial fast decay component and the amount decayed is dependent on the proximity of the core to the anode hole and the width of the separation between the holes as explained in Section 2.3.3.

The microscope pictures of the design of the FORC-2 fibre are shown in Figure 4.5 (b). The NA of the core was lowered to improve splice losses to standard fibres and also to lower the impeding effects of the core-cladding interface. The core was moved further away from the anode hole, minimising the mode leakage loss and greatly improving the stability of the EO coefficient. The separation between the holes was increased to 2 times that of ACREO-1 and about 3 times that of ACREO-2 and FORC-1 fibres. To extend the nonlinear region further and increasing its overlap with the core, the fibre can be poled for longer periods of time.

4.2.4 Temperature optimisation- FORC-2 fibre

As with previous fibres, the poling temperature was optimised for the FORC-2 fibre. A poling voltage of 7.5kV, well below the breakdown voltage was used for all devices. The measurement of the evolution of the EO coefficient was made using the 1550nm MZI system and OPD described in Section 3.2.4. The evolution of the electro-optic coefficient for the different poling temperatures is shown in Figure 4.8(a). The characteristic dip observed in one of the devices of the FORC-1 fibre is visible for most of the devices poled at a range of temperatures. In comparison to the FORC-1 fibre, the core of the FORC-2 fibre is positioned further into the glass and as a result the depletion region takes a longer period of time to reach the core. Thus the dip is

observable for many devices, even though the measurements were taken with the same 2 seconds interval. The noise seen is attributed to the movement of electrodes within the holes. The diameter of the electrodes used for the uniform poling of the FORC-2 fibre were larger ($30\mu m$) than that used previously for the ACREO fibres ($25\mu m$). The use of larger wires helped reduce random movements in the holes.

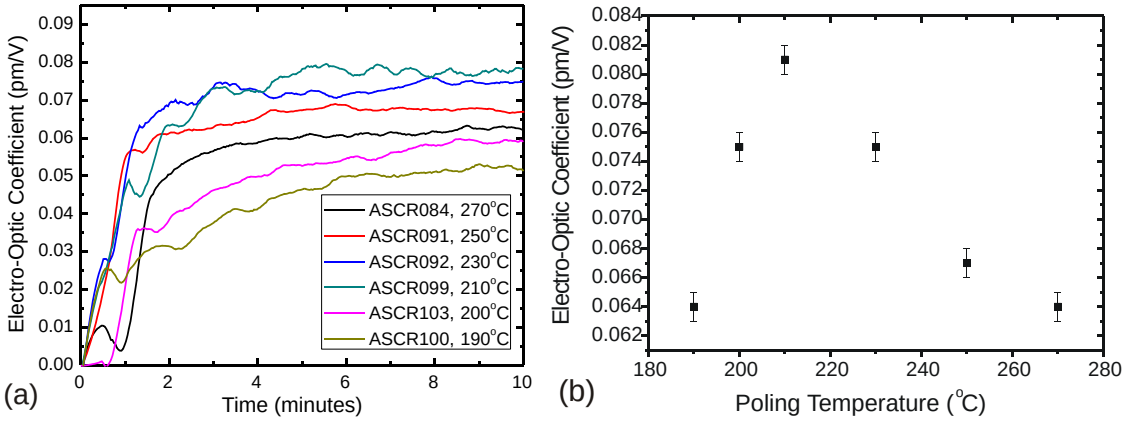

Figure 4.8 (a) Evolution of the electro-optic coefficient during poling for varying temperatures (b) The maximum electro-optic coefficient reached for each poling temperature

The optimum poling duration is strongly dependent on the poling temperature. The poling voltage of $7.5kV$ used for the temperature optimisation experiments is less than 75% of the actual break-down voltage for this fibre at 210℃. The lower voltage was chosen to avoid breakdown at higher temperatures. All devices were poled until a slight roll-off was seen; however only the first ~10 minutes of the poling evolution is shown for clarity. Since the residual values vary with the optimum poling duration, a direct comparison is difficult to make, thus the highest value reached during poling was used to determine the optimum poling temperature. The optimum temperature was determined to be in the range $200 - 220$℃ for the FORC-2 fibres. It is believed that the optimum temperature is dependent on the other two poling parameters, the applied voltage and duration. All devices fabricated since have been poled within this range (typically 210℃) at the highest poling voltage possible, typically $10 - 11kV$ for a duration of ~1 hour.

4.2.5 Residual nonlinearity and stability

The stability of the induced nonlinearity in the FORC-2 fibre is discussed in this section. The residual EO coefficient was continuously monitored for two of the devices used in the temperature optimisation experiments. Device ASCR084 and ASCR103

were poled at a voltage of $7.5kV$ and temperatures of 270℃ and 200℃ respectively. The devices were poled until a slight roll-off the EO coefficient was observed which for device ASCR084 and ASCR103 occurred at ~30 and 160 minutes respectively.

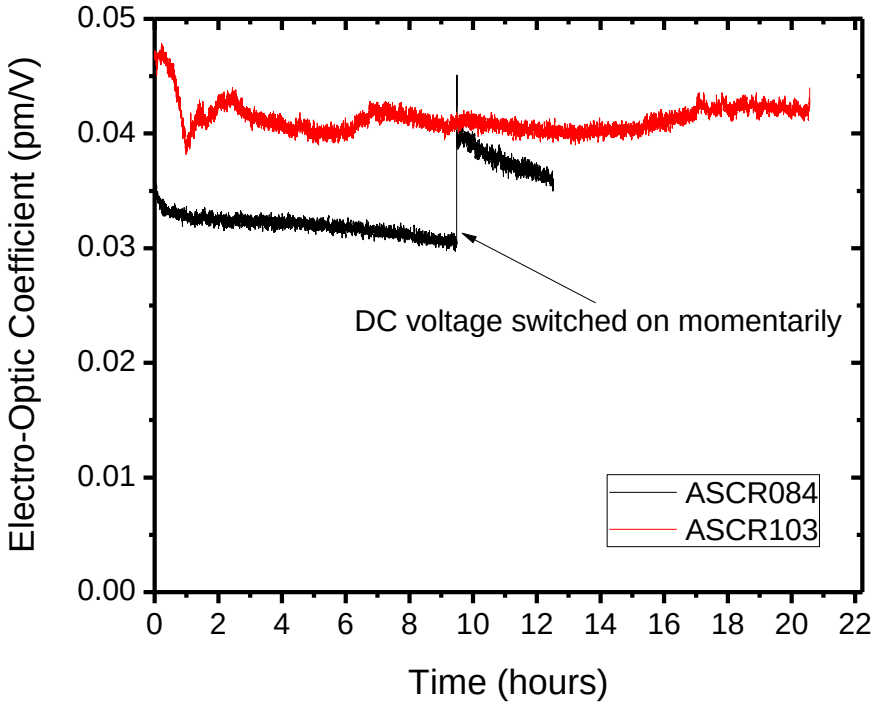

Figure 4.9 Residual EO coefficient in two FORC-2 fibre devices

As mentioned previously, the removal of the DC poling voltage causes the electrodes to relax and move away from the edge of the holes, reducing the applied AC test field and affecting the measurement of the EO coefficient. The DC field was switched on momentarily for device ASCR103 after about 9.5 hours of monitoring bringing the electrodes close together again and raising the residual EO to a higher value as a result. The electrodes were observed to remain attracted to each other momentarily after the DC field is switched off, possibly due to electrostatic attraction. The EO coefficient measurements were taken immediately after the DC field was switched off. The residual values seen are about $20-30\%$ lower than that typically obtained at the optimum poling conditions. At optimum poling conditions a value in the range of $0.05-0.06pm/V$ was consistently achieved. The design of the FORC-2 fibre with the placement of the core away from the holes and the increased separation between the holes has helped avoid the decay of the induced nonlinearity as seen in previous designs. In fact several devices were periodically erased and used for frequency doubling all within an hour after poling and none of the devices showed any sign of

reduction in the generated second harmonic power even months after the first measurement. The deviations seen in Figure 4.9 are thus attributed wholly to the movement of electrodes within the holes in the case of the FORC-2 fibre. The initial drop seen, particularly with the ASCR103 device, was originally thought to be due to the fast decay seen with other fibres, however the stability of the SH signal produced with many devices fabricated from the FORC-2 fibre suggested that this drop was in fact due to electrode movement.

4.2.6 Effective index determination

As with previous fibres, FBGs were inscribed in the new FORC-2 fibre. However, the FBGs spectra were not visible with a low power white light source, in either transmission or reflection mode. This is most likely due to the lower germanium concentration in the FORC-2 fibre. Although it would have been possible to write a longer grating, it was decided that it would be simpler to fabricate a QPM multi-period grating for SHG to determine the relationship between QPM period and the fundamental wavelength. Before the multi-period structure was fabricated, the index profile shown in Figure 4.10 (a) was used to generate the dispersion relation for a range of wavelengths, which would provide a closer estimate of the period-wavelength relationship.

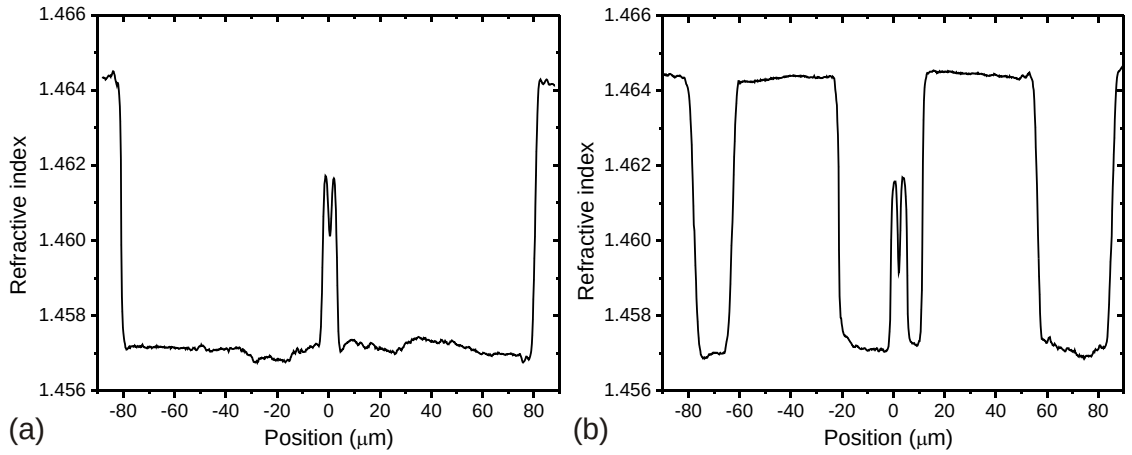

Figure 4.10 (a) Index scan perpendicular to the direction of the holes (fast axis) (b) index scan along the direction of the holes (slow axis). The characteristic index dip produced during the MCVD preform fabrication can be seen in both profiles.

The index profiles shown in Figure 4.10 was taken with a commercial index profiler (Photon Kinetics, S14), which utilises a HeNe laser and gives a relative measurement of the difference in the refractive indices of the core and cladding only. Since it was

known that the fibre had a fused silica cladding, the index of fused silica at $632.8nm$ wavelength ($n_{fused} = 1.45702$) was used to normalise the measurement for the cladding as obtained with the index profiler. The higher index seen on the edges of the fibre in Figure 4.10(a) and (b) and in the holes on either side of the core in Figure 4.10 (b) are from the high index gel coating used on the ends of the fibres. Since it was known that the core was doped with germanium only and knowing the core radius ($2.80\mu m$), the variation of the refractive index with the wavelength was generated for this fibre, using a mode propagation simulator. The concentration of germanium in the core was determined to be $2.7mol\%$ and the cut-off wavelength of the fibre was determined to be $\sim 780nm$ from this simulation.

With the variation of the refractive index with the wavelength relationship (Figure 4.11(a)) was then used to generate the relationship between the QPM period and fundamental wavelength (Equation 3.27) as shown in Figure 4.11(b).

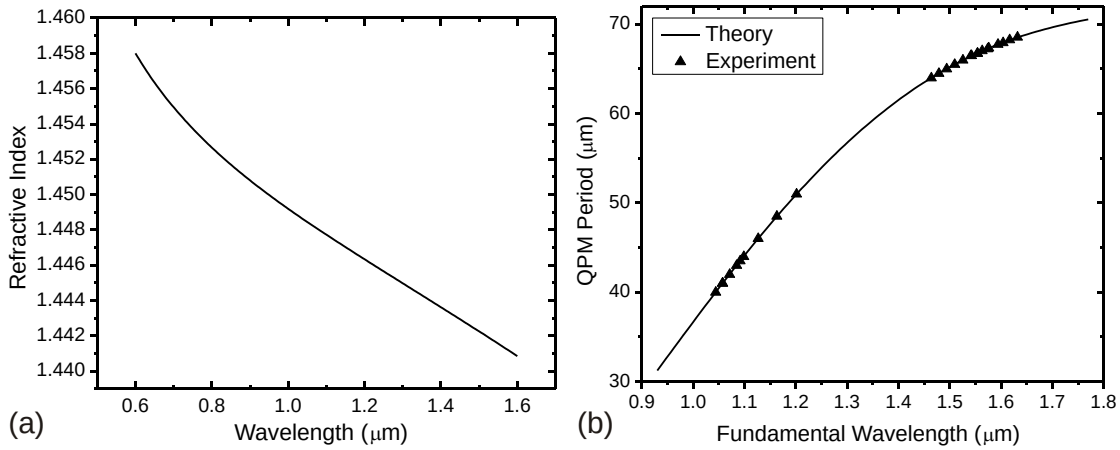

Figure 4.11 (a) Variation of the effective refractive index (modal index) with wavelength in FORC-2 fibre (b) Dependence of the QPM period on the fundamental wavelength for the FORC-2 fibre from mode-propagation simulator (solid line) and experimental measurements (filled triangles)

4.2.7 Multi-period characterisation

The FORC-2 fibre was considered for frequency doubling of fibre lasers operating in two wavelength regimes: 1. $1060 - 1180nm$ (ytterbium) 2. $1530 - 1560nm$ (erbium, erbium/ytterbium). Multi-period devices were fabricated for a range of periods for the phase matching of wavelengths around these regions using the calculated relationship between the QPM period and fundamental wavelength (Figure 4.11(b)). The individual PPSF gratings were $5cm$ long. The multi-period grating around the $1.5\mu m$ and $1.0\mu m$

regimes were characterised using the MOPA supercontinuum and a solidstate Nd:YVO_4 source (Lumera Super Rapid) pumping an optical parametric generator respectively. The spectra of these sources are shown in Figure 3.7(a) and (b). The measured SH peaks are similar in appearance to those of the ACREO-2 multi-period gratings (Figure 4.3) and are not shown here. The measured phase matching wavelengths for the multi-period gratings are shown as triangular data points on the curve in Figure 4.11(b) along with those of all the PPSF devices fabricated later with the FORC-2 fibre. The outstanding agreement between the theoretical curve, calculated from the refractive index profile of the fibre, and the experimental data over a 500 nm-wide spectral range is an indication of the good uniformity of the fibre and the exceptional reproducibility of the point-by-point UV erasure technique. As it turns out the simulation of the effective refractive index and the wavelength relation (Figure 4.11(a)) provided more than just an approximation of the QPM period-wavelength relationship, it was a perfect match.

4.2.8 Frequency doubling

The FORC-2 fibre with its relatively low splice loss of $\sim 0.5 dB$ (at $1550 nm$) to standard telecommunications fibre (SMF-28) was found to be suitable for frequency doubling of erbium doped fibre laser sources. The positioning of the core away from the holes and the lower degree of drawing induced twist allowed the fabrication of long PPSF devices, only limited by the travel of the translation stage used ($32 cm$). The interaction length was improved by 1.5 fold over the length of $20 cm$ achieved in the ACREO-1 fibre.

A list of the best performing devices fabricated from the FORC-2 fibres is given in Table 4.4. These devices were typically poled at a temperature of 210℃ and a voltage of $10 kV$. The PPSF devices were characterised with a $9 mW$ CW external cavity tunable laser system which was not available for the devices fabricated from the previous fibres. The laser system with its very narrow linewidth spectrum and stable output power was found to be ideal for the characterisation of the PPSF devices. The uncertainties in the power lost through nonlinear broadening and amplified spontaneous emission (ASE) in the high power fibre laser systems are completely avoided and a more accurate measurement of the SH power and subsequently the normalised

conversion efficiency was obtained. The SH power was measured using a silicon detector head (Newport 818-SL) and power meter (Newport 2936-C). As with the ACREO fibre devices, the nonlinear coefficient, d_{33} was then inferred from the normalised conversion efficiency, η_2 using Equation 2.52.

Table 4.4 List of FORC-2 PPSF devices

Batch No.	Device Name	Length (cm)	Period (μm)	Wavelength (nm)	BW (nm)	SH power (nW)	Normalised Conversion, η_1 ($\%W^{-1}$)	Normalised Conversion, η_2 ($\%W^{-1}cm^{-2}$)	Nonlinear Coefficient d_{33} (pm/V)
4	ASCR119	20.0	66.6	1544.25	0.68	15.84	0.0283	7.08 x10^{-5}	0.052
5	ASCR133	31.5	66.5	1542.55	0.45	41.34	0.0737	7.43 x10^{-5}	0.053
5	ASCR137	31.5	66.5	1540.2	0.45	41.22	0.0734	7.41 x10^{-5}	0.053
5	ASCR140	31.5	66.5	1541.52	0.46	40.83	0.0728	7.34 x10^{-5}	0.053
6	ASCR148	31.5	66.5	1538.6	0.46	48.30	0.0861	8.68 x10^{-5}	0.057
6	ASCR149	31.5	66.5	1540.5	0.45	44.12	0.0788	7.94 x10^{-5}	0.055

The values of the residual EO coefficient measured and the nonlinear coefficient ($d_{33} = \frac{n_o^4}{4}.r$) were in good agreement for the FORC-2 fibres. For the devices shown in Table 4.4, the values of the induced nonlinearity are quite comparable to each other ($d_{33} = 0.054 \pm 0.001$). This is an indication of the reproducibility of the nonlinearity in the FORC-2 fibre. The use of larger electrodes during thermal poling helps reduce electrode movements as explained in the preceding section. Further the anode hole for the FORC-2 fibre is positioned further inside the fibre ($30\mu m$) compared to ACREO-1 ($18\mu m$), and therefore the field in between the wires was less likely to be influenced by the metal heater block. This is due to the greater physical separation between the wires and the heater block. Thus the repeatability of the value of the induced SON in this fibre was greater than any of the other fibres used in this present work.

4.2.9 High average second harmonic power

The FORC-2 fibre was used in a fruitful collaboration with Multitel in Mons Belgium, the results of which are presented here. Several devices of $42cm$ wire overlap were fabricated and poled at the optimum temperature of 210℃ and $11kV$ poling voltage. The residual EO coefficient measured using the interferometric technique for the devices was typically in the range of $0.05 - 0.06pm/V$. The wires were subsequently removed and the devices were prepared for UV erasure. All devices were UV erased at

the optimised erasure parameters over $\sim 32cm$, the maximum length possible with the translation stage used. These devices (Batch number 5, Table 4.4) were pre-characterised with the CW tunable diode laser source before being taken to Belgium for the frequency doubling experiments with a high power fibre laser source. The results obtained with device ASCR137 are presented here.

The second harmonic tuning curve shown in Figure 4.12 was obtained by scanning the wavelength of the low power CW laser and recording the corresponding second harmonic power. The acceptance bandwidth (FWHM) of the device was measured to be $0.46nm$ in good agreement with theoretical predictions. The almost perfect $sinc^2$ profile of the tuning curve is a testament to the extremely good quality of the quasi-phase matched grating over the whole $32cm$ length. From this measurement, the normalised conversion efficiency (η_1) was estimated to be $7.34x10^{-2}\%W^{-1}$, translating to a 3.3-fold improvement in comparison to the previously best reported value [1] and 14-fold over [11]. The normalised conversion efficiency (η_1) was further improved to $8.61x10^{-2}\%W^{-1}$ in a device made (ASCR148) after the collaboration.

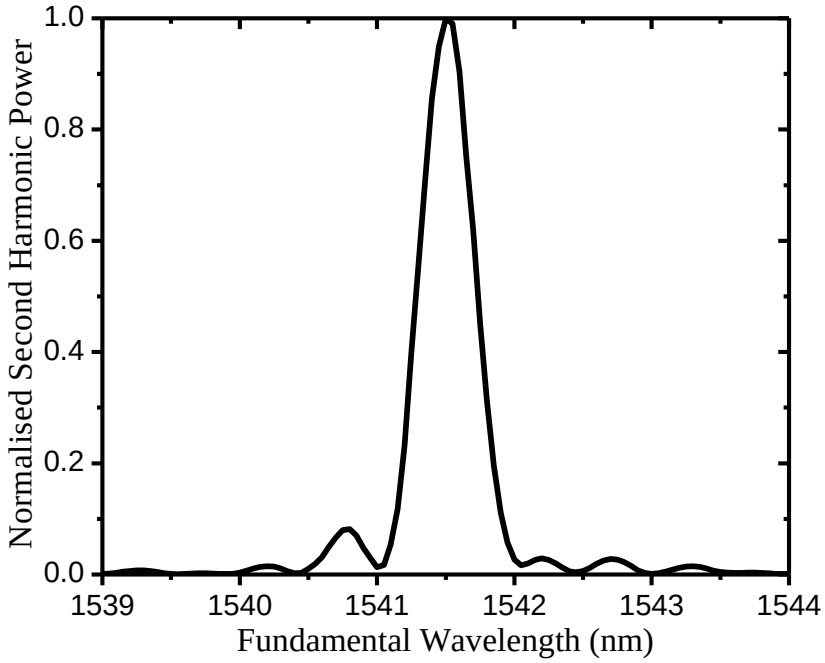

Figure 4.12 Second harmonic tuning curve of device ASCR140 obtained with the low power CW tunable laser source

For the demonstration of SHG, the PPSF device was spliced to the output of a high-power, narrow linewidth, pulsed fibre laser source delivering $2.5ns$ pulses at a

repetition rate of $3MHz$. This is the Multitel-MOPA source described in Section 3.4.1 and shown schematically in Figure 3.9. The output spectrum of the MOPA source is shown in the inset of Figure 3.9.

The quadratic dependence of the average second harmonic power at the wavelength of $771.75nm$ against the fundamental source power operating at $1541.5nm$ is shown in Figure 4.13. The average conversion efficiency is also shown in Figure 4.13 for increasing fundamental power. The maximum average conversion efficiency was estimated to be 15.2% with just $207W$ of fundamental peak power. The minor deviation from the expected linear response seen in the conversion efficiency is attributed to the variation in the ratio of the power contained within the narrow linewidth to the ASE power in the fundamental source. The generated SHG did not appear to decay even with repeated and prolonged testing with the high power fibre laser source. The obtained average SH power was $236mW$ contained within the LP_{01} mode is to date the highest obtained in a PPSF device.

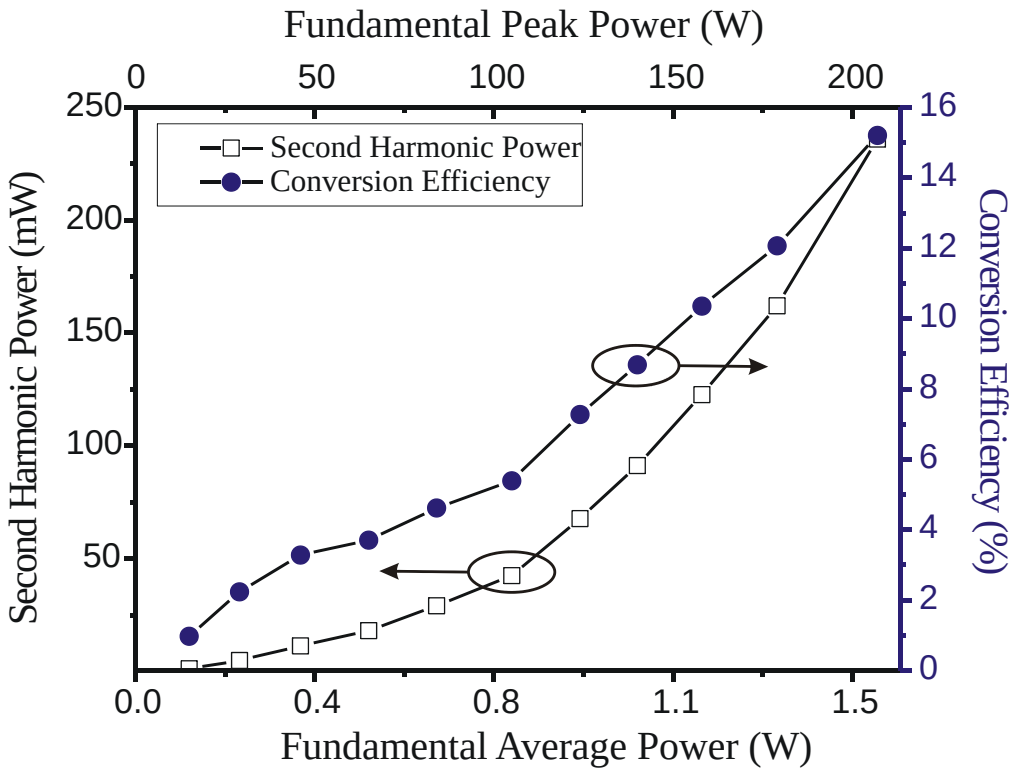

Figure 4.13 Average second harmonic power and average conversion efficiency measured as a function of the fundamental power for the 32cm long PPSF device

The significant enhancement obtained over previously reported results is attributed to the improvement in the design of the specialty twin-hole fibre. The uniformity of the fibre along its length is a critical parameter for quasi-phase-matched SHG.

Irregularities in the core along the length of the fibre result in variations in the effective index and consequently the phase-matching condition for second harmonic generation. This in turn affects the quality of the second harmonic profile and the conversion efficiency. Lowering the NA of the FORC-2 fibre lowered the QPM tolerances as explained in the following section. The axial twist induced during the drawing process of the twin-hole fibre limits the length of the point-by-point UV erasure. Tighter control over the drawing parameters produced a fibre with good uniformity over the length and a significant reduction in twist. Given the noticeable improvement in the SON in the FORC-2 fibre despite the positioning of the core away from the anode hole, it is believed that the width of the nonlinear region and its overlap with the core is improved, possibly through the application of a poling voltage $2-3$ times that typically used in the poling of silica fibres. The longer poling durations used ($\sim$1 hour) is also thought to play a role in creating a more uniform SON across the core than with other fibres. Furthermore, the induced nonlinearity was extremely stable and did not appear to decay or possess a fast decay component as observed in designs with the core positioned closer to the anode hole [4].

4.3 Comparison with previous results

In Table 4.5, a summary of the parameters of the best performing device for each of the fibres used in this present work along with the results reported in literature is provided. To facilitate a direct comparison, all results listed were from devices used for frequency doubling of laser sources around $1550nm$ and the normalised efficiencies, η_1 and η_2 have been quoted for all devices along with the nonlinear coefficient, d_{33} calculated from η_2 and the overlap area, A_{OVL}.

Table 4.5 Comparison of PPSF device performance for frequency doubling with published results and the devices from this present work

	Length (cm)	Normalised efficiency, η_1 ($\%W^{-1}$)	Normalised efficiency, η_2 ($\%W^{-1}cm^{-2}$)	Overlap Area, A_{OVL} (μm^2)	Nonlinear coefficient, d_{33} (pm/V)
Pruneri et al.	7.5	$5.25\text{x}10^{-3}$	$9.30\text{x}10^{-5}$	35.0	0.028
Corbari et al.	11.5	0.022	$1.68\text{x}10^{-4}$	14.8	0.029
ACREO-1	21	0.049	$1.22\text{x}10^{-4}$	31.4	0.031

ACREO-2	21	0.008	1.91×10^{-5}	28.9	0.012
FORC-1	10	0.001	1.20×10^{-5}	25.6	0.008
FORC-2	31.5	0.086	8.68×10^{-5}	156.0	0.057

Comparing the values of the normalised efficiency, η_1 first, it can be seen that a significant improvement was achieved with the ACREO-1 and FORC-2 fibres over previously reported results. ACREO-1 fibre yielded a d_{33} nonlinearity comparable to that of previous results of Pruneri et al [11] and Corbari et al [1]. Thus the improvement obtained with the ACREO-1 fibre, is purely through the enhancement of the PPSF length. With the FORC-2 fibre, a 4-fold improvement in η_1 was obtained over previously published results. Comparing the ACREO-1 and FORC-2 fibres, the nonlinearity has been improved 2-fold with the latter. Uniformly poled ACREO-1 fibre devices typically had the same initial nonlinearity as that of FORC-2 but suffered from the initial fast decay as a result of its design with the core positioned close to the anode hole. Although the induced nonlinearity has been improved by a factor of 2 with the improved design of the FORC-2 fibre, the lower NA and the consequently larger area overlap of the fundamental and second harmonic modes inhibited the expected 4 times improvement in the second harmonic power. The area overlap can be reduced by increasing the NA or lowering the cut-off wavelength (smaller core) further. However, it is clear that a trade-off exists between the fibre parameters, the inducible SON and nonlinear frequency conversion.

4.4 Comparison of QPM tolerances

Fibres ACREO-1 and FORC-2 were used extensively for the frequency doubling of erbium/ytterbium fibre laser sources. Although the core and cladding constituents of these fibres were identical, the germanium concentration, NA and the cut-off wavelengths were quite different. Besides a similar core size, the geometry of the fibres was also dissimilar leading to differences in the poling characteristics and the stability of the induced nonlinearity. The wavevector mismatch for a QPM structure in an optical fibre was introduced in Equation 2.49. The QPM period is defined as

$$\Lambda_{QPM}(\lambda, NA, a) = 2\pi \left[\beta\left(\frac{\lambda}{2}, NA, a\right) - 2\beta(\lambda, NA, a)\right]^{-1} \qquad (4.1)$$

Where a is the radius of the core and $NA = \sqrt{n_{core}^2 - n_{cladding}^2}$. The dependence of the QPM period on the three key parameters of wavelength, NA and the core size are shown in Equation 4.1. In an effort to quantify the tolerances of the QPM period with the phase matching wavelength, the refractive index profiles of the two most useful fibres (ACREO-1 and FORC-2) were measured using the index profiler introduced earlier. These profiles were then used to generate the effective index to wavelength relation (FORC-2 index profile shown in Figure 4.10(a)) using a mode propagation simulation software. Using this relation, the QPM period as a function of the fundamental wavelength was generated for both fibres as shown in Figure 4.14. The variation of the fibre diameter during the drawing process was explained in Section 3.1.1. The relationship of the QPM period to the fundamental wavelength was generated for the specified core size (black line), a 2% increase (red line) and a 2% decrease (green) in the core size. The lower and upper insets of Figure 4.13 provide a close-up of one of the areas of interest for erbium/ytterbium fibre laser sources for the ACREO-1 and FORC-2 fibres respectively.

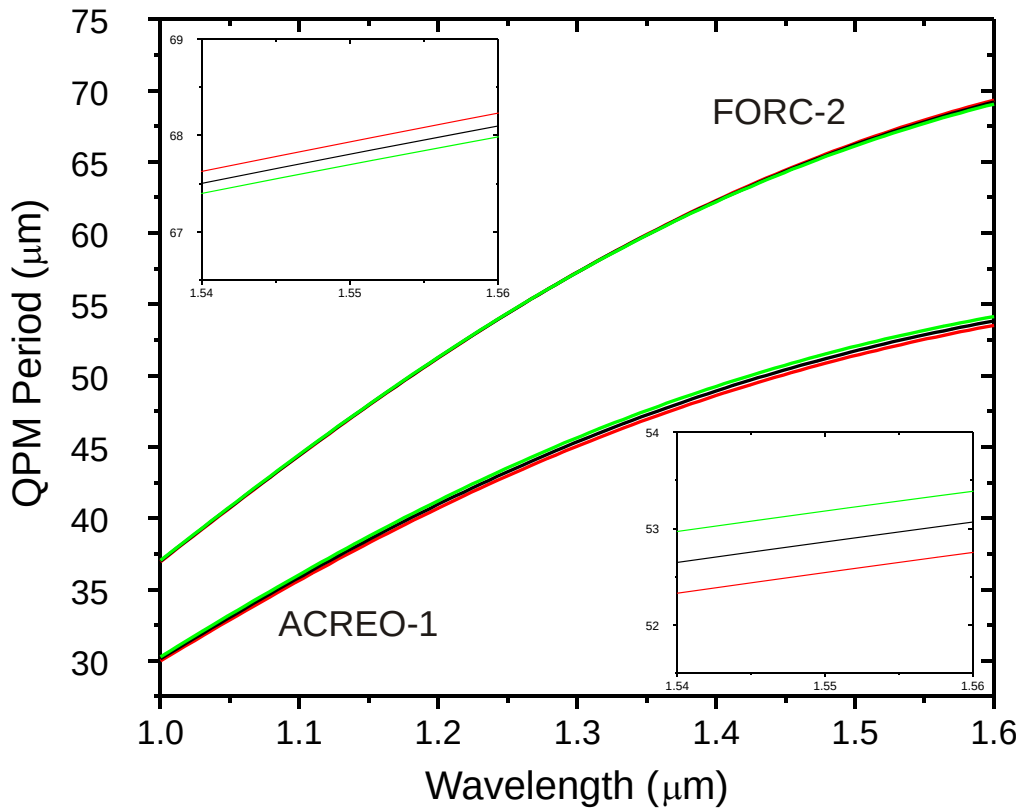

Figure 4.14 QPM period as a function of fundamental wavelength for ACREO-1 and FORC-2 fibres. Black line represents actual core size, green and red lines indicate the core size variation of plus and minus 2% respectively

From the graphical representation of QPM period as a function of wavelength in Figure 4.14, it is immediately clear that the tolerances on the uniformity of the core size are greater for fibres of higher NA. For frequency doubling of $1550nm$, a core variation of 2% would result in a shift of $\sim 16nm$ of the fundamental phase matching wavelength for the ACREO-1 fibre and $\sim 4nm$ for the FORC-2 fibre. Over the relatively short lengths of the PPSF devices, both fibres were found to be extremely uniform as evidenced by the good agreement between measured and theoretical values of the acceptance bandwidth for a given length. The symmetrical profiles of the SH tuning curves are a further testament to the uniformity.

4.5 Conclusions

A summary of the experimental results obtained during the course of this present work was given in this chapter. The interferometric techniques developed for the *in-situ* measurement of the induced SON were extensively used to optimise poling conditions for all the fibres used. This ensured the inducement of the maximum possible SON in all the fibres used, exploiting their full potential for frequency doubling and other SON processes. Further, a significant improvement in the design of the fibre was aided by the *in-situ* measurements of the poling evolution and decay of the SON. The PPSF devices were used primarily for the frequency doubling of erbium/ytterbium fibre laser sources.

The fibre design has been progressively improved, with the last fibre (FORC-2) fabricated yielding almost a two-fold improvement in the induced nonlinearity over previously reported results and also over the best ACREO-1 fibre result with no observable decay in the nonlinearity over normal operating temperatures. The improvement in the normalised efficiency, η_1 of the FORC-2 fibres over previous fibres is attributed to the improved nonlinearity and to the significant extension of the periodically poled length. The average power and normalised conversion efficiency have been significantly enhanced over previous reports through the improved fibre design and optimised PPSF device fabrication. A conversion efficiency of 15.2% was demonstrated, limited by the relatively moderate power available from the fibre laser source used. The improvement reported herein is due for the greater part to the ability to fabricate long periodically poled fibres, compensating for the relatively low effective

nonlinearity and enhancing the conversion efficiency through the quadratic dependence of second harmonic power with interaction length.

4.6 References

1. Corbari, C., et al. *All-fibre frequency conversion in long periodically poled silica fibres*. in *OFC*. 2005. Anaheim, California, USA: Optical Society of America.
2. Canagasabey, A., et al. *Tuneable Second Harmonic Generation in Long Periodically Poled Optical Fibres*. in *OFC*. 2005. Anaheim, California, USA: Optical Society of America.
3. Canagasabey, A., et al. *Extended lifetime of the electro-optic coefficient in poled silica fibres*. in *Australian Conference on Optical Fibre Technology (ACOFT)*. 2001. Sydney, Australia: OSA.
4. Janos, M., et al., *Growth and Decay of the Electrooptic Effect in thermally Poled B/Ge Codoped Fiber.* Journal of Lightwave Technology, 1999. **17**(6): p. 1037.
5. Sinha, S., et al., *Efficient yellow-light generation by frequency doubling a narrow-linewidth 1150 nm ytterbium fiber oscillator.* Optics Letters, 2006. **31**(3): p. 347.
6. Georgiev, D., et al., *Watts-level frequency doubling of a narrow line linearly polarized Raman fiber laser to 589nm.* Opt. Express, 2005. **13**(18): p. 6772.
7. Dianov, E.M., et al., *High-power cw bismuth-fiber lasers.* Journal of the Optical Society of America B-Optical Physics, 2007. **24**(8): p. 1749.
8. Dvoyrin, V.V., et al. *Yellow All-fiber Bi laser*. in *ECOC*. 2008. Brussels, Belgium.
9. An, H.L. and S. Fleming, *Hindering effect of the core-cladding interface on the progression of the second-order nonlinearity layer in thermally poled optical fibers.* Applied Physics Letters, 2005. **87**(10): p. 101108.
10. Faccio, D., et al., *Effect of core-cladding interface on thermal poling of germano-silicate optical waveguides.* Optics Communications, 2001. **196**(1-6): p. 187.
11. Pruneri, V., et al., *Greater than 20% efficient frequency doubling of 1532nm pulses in quasi-phase-matched germanosilicate fibres.* Optics Letters, 1999. **24**(4): p. 208.

Chapter 5: Extended functionality through QPM engineering

Quasi-phase-matched (QPM) interactions for second order nonlinear processes in poled fibres, is achieved through periodic point-by-point UV erasure, a technique tried and tested, particularly for the fabrication of long period fibre gratings (LPFG). The simplicity and repeatability of this technique (Section 3.3) can not only be exploited for the fabrication single-period periodically poled silica fibre (PPSF) but also for the fabrication of specialty structures for specific applications. In this chapter, the results of the demonstration of wavelength tunability of the second-harmonic (SH) and the implementation of aperiodic poling for bandwidth control are presented. The application of these established techniques is envisaged to increase the functionality and versatility of PPSFs further, reinforcing the motivation for all fibre solutions to nonlinear frequency conversion of fibre lasers.

5.1 Wavelength tunable $\chi^{(2)}$ processes

The electrodes required for periodic poling for QPM in ferroelectric crystals are fabricated through photolithographic patterning. This technique offers a degree of flexibility in the patterning of the electrodes and has enabled the demonstration of a number of novel frequency conversion devices. A wavelength tunable optical parametric oscillator (OPO) has been demonstrated in a transversely offset multi-grating structure with varying periods [1]. Wavelength tuning is achieved through transverse translation of the crystal. This technique does not allow continuous tuning, although it is possible to fill in intermediate wavelengths through temperature fine tuning [2]. A fan-out grating structure [3-4] or an angle-tuned cylindrically polished crystal can also be used to obtain continuous wavelength tuning. Temperature tuning of the wavelength has also been demonstrated in periodically poled lithium tantalate (PPLT) [5], however this technique is not practicable for tuning over very large ranges given the large temperature excursion required for relatively short tuning range. For SHG from PPLT into UV ($325nm$), a temperature change of $240℃$ was required for

$14nm$ tuning of the fundamental wave [5]. The requirement for periodically poled crystals such as PPLN and PPLT to be operated at elevated temperatures to avoid photorefractive damage is a further limitation on temperature tuning, particularly for the frequency doubling of high power sources [6].

5.1.1 Wavelength tunable fibre Bragg gratings

Wavelength tuning of fibre Bragg gratings (FBG) using mechanical compression has been recognised as the best solution to date for achieving very large tuning ranges [7]. The high endurance of silica based fibres to high compressive stresses allows efficient broadband tuning of FBGs encompassing the S, C and L bands, translating to a tuning range of 110 nm [7]. The mechanically induced strain physically compresses the periodic structure causing a linear shift of the Bragg wavelength as a result of the induced refractive index change through the strain-optic effect. In this work, broad wavelength tuning of the generated second harmonic light is demonstrated through mechanical compression of the periodic QPM structure.

5.1.2 Compression through elastic bending

The application of compressive stress on a beam causes it to bend into an arc shape. The beam experiences tensile and compressive stresses simultaneously. The side experiencing tensile stress is elongated while the side experiencing compressive stress is compressed, as shown in Figure 5.1. The region in between, called the 'neutral axis', remains neutral of these two stresses. The strain experienced by the beam is defined as the change in length divided by the original length.

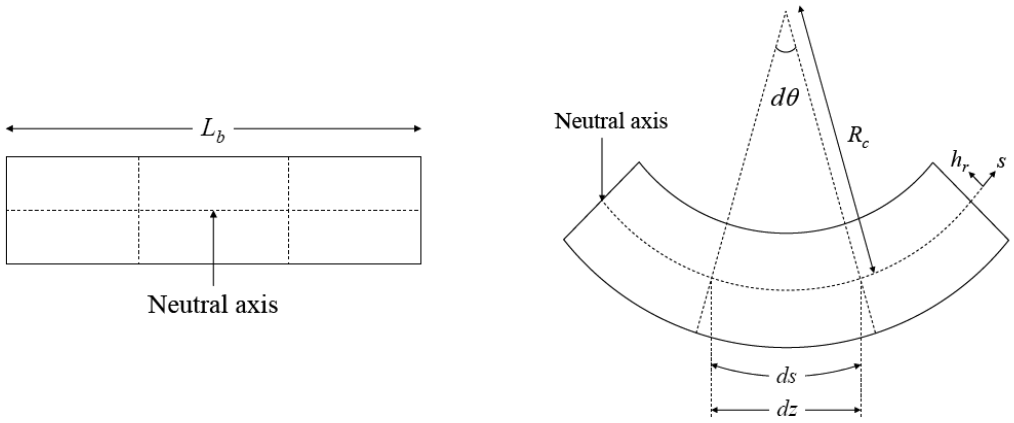

Figure 5.1 The beam before (left) and during (right) compression

From Figure 5.1, the length of the unit segment on the neutral axis ds is given by

$$ds = R_c d\theta \quad (5.1)$$

A segment at a distance h_r from this neutral axis is then given by

$$ds_h = (R_c \pm h_r)d\theta \quad (5.2)$$

The strain experienced by the segment at the distance h from neutral is

$$\varepsilon_s = \frac{ds_h - ds}{ds} \quad (5.3)$$

Combining Equations 5.1-5.3 gives,

$$\varepsilon_s = \frac{(R_c \pm h_r)d\theta - R_c d\theta}{R_c d\theta} = \pm\frac{h_r}{R_c} \quad (5.4)$$

Where the positive and negative signs indicate the tensile (below neutral axis) and compressive (above neutral axis) strains respectively.

5.1.3 Tunable wavelength PPSF

Tunable SHG in a PPSF was firstly demonstrated using a $3cm$ long PPSF device fabricated from the ORC-1 fibre [8]. Wavelength tunability was achieved over $27.8nm$ in the fundamental. Using the same technique, this range was later extended to almost $45nm$ using a $4cm$ device fabricated from the ACREO-1 fibre. Since the technique employed in both demonstrations was identical, only the results of the second

demonstration are presented. The results of the first demonstration can be found in reference [8].

The PPSF device was wholly embedded in a composite beam, consisting of a base-plate of high tensile steel and two layers of polymeric material with disparate Young's modulus values. The twin-hole fibre device is positioned so that the two holes are parallel to the beam and the polymeric layers. The lower polymeric layer affixed to the steel beam is of sufficient hardness to resist buckling and indentation. The fibre is sandwiched between this layer and another softer layer which conforms to the fibre to hold it firmly in place. This ensures that the device is compressed only in the direction perpendicular to the holes. The polymer layers and the embedded PPSF device are attached to the steel beam using a strong adhesive solution. The beam containing the PPSF device is then mounted on an aluminium purpose-built stage, in between a fixed block and a moveable block, as seen in Figure 5.2. During tuning, the inward translation of the moveable block causes the beam to deform into a circular arc shape as explained in the preceding section. The strain (Equation 5.4) for the full beam length (L_b) for compression of the PPSF is given by

$$\varepsilon = \frac{h_r \theta}{L_b} \quad (5.5)$$

The wavelength shift of the fundamental pump wave, $\Delta\lambda$ is given by

$$\Delta\lambda = (1 - \rho_e)\varepsilon\lambda_f \quad (5.6)$$

where λ_f is the fundamental wavelength in idle state, and $\rho_e \approx 0.22$ is the photoelastic constant of the optical fibre.

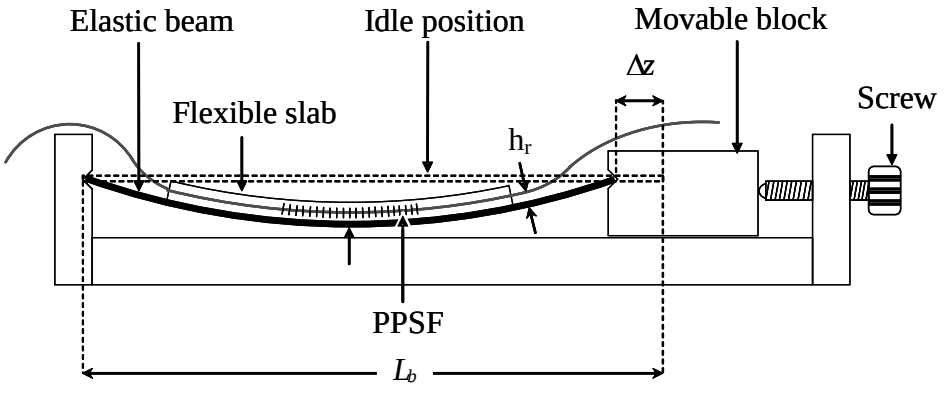

Figure 5.2: Compression tuning package used for wavelength tuning of the PPSF device.

5.1.4 Spectral characterisation

The characterisation of the PPSF devices was performed with the high power master oscillator power amplifier (MOPA) fibre laser (Figure 3.7(a)) source delivering $5ns$ pulses, at a repetition rate of $450\,kHz$, described in Section 3.4.1. The source consists of a seed laser followed by a series of cascaded fibre amplifiers in a MOPA configuration. The source produces high power in the erbium gain range and a lower power supercontinuum in the $1400-1600nm$ range. The PPSF device used for the wavelength tuning experiments had a QPM period of $53.7\mu m$ which in this particular fibre corresponds to a fundamental wavelength of $1594.5nm$. The length of the embedded PPSF section was $4cm$. The characterisation of the generated second harmonic during tuning was performed using the broadband supercontinuum generated by the aforementioned fibre laser source. The wavelength spectrum of the source is shown in the lower portion of Figure 5.3. The spectrum of the generated second harmonic wave was captured with an optical spectrum analyser after each compressive tuning adjustment.

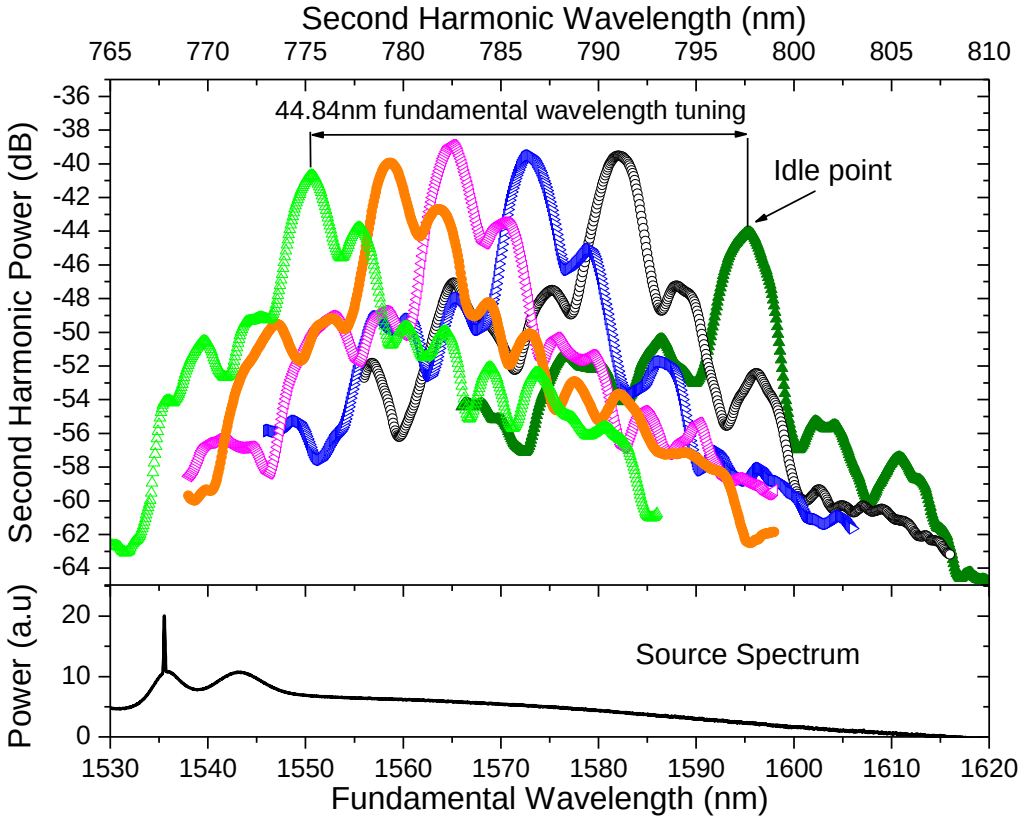

Figure 5.3: Second harmonic power measured as a function of the fundamental wavelength for the 4cm PPSF device. Only 6 profiles from a total of 26 taken are shown for clarity. The 'idle point' indicates the SH spectrum of the PPSF device prior to tuning.

Figure 5.3 shows the SH spectral profiles for a range of compressive strain values. The SHG spectrum, measured when no strain is applied to the QPM grating, is indicated as the 'idle point'. The spectra to the left of the idle point were measured for increasing compressive strain tuning. As the power of the supercontinuum source used for characterisation is not consistent across its spectral range, the generated SH power also fluctuates. The quadratic relationship between the SH power and the fundamental pump power further accentuates the SH signal variation. The inherent birefringence of the twin-hole fibre results in two slightly different phase matching conditions between the orthogonal polarisation states in the fibre, giving rise to two SH peaks of slightly different centre wavelengths. The polarisation of the fundamental wave was initially adjusted at the idle point to extinguish the second (weaker) SH signal. However, during the course of the experiments, the polarisation state of the fundamental wave was seen to drift, as evidenced by the presence of a weaker SH signal from the other polarisation state. The shoulder peak seen alongside the stronger peak in the profiles to the left of the idle state profile is thus attributed to the contribution from the orthogonal polarisation state. This drift also causes a reduction in the power of the primary SH peak as seen with further tuning. The presence of the holes did not seem to alter the spectrum of the main SH peak during compression. However a study of the changes to the birefringence of this fibre with compression was not carried out. The acceptance bandwidth of the generated second harmonic light was measured to be $\sim 4.65nm$ for this $4cm$ PPSF device, in agreement with theoretical predictions. Initially a maximum tuning range of $\sim 45nm$ in the fundamental wavelength was obtained, limited by the travel range of the compression tuner used. Further attempts to increase this range using a second tuner resulted in the breakage of the device at one of the splice points. The short travel stage could still be used for further tuning if the distance (h_r) from the fibre to the base plate in the composite beam is increased.

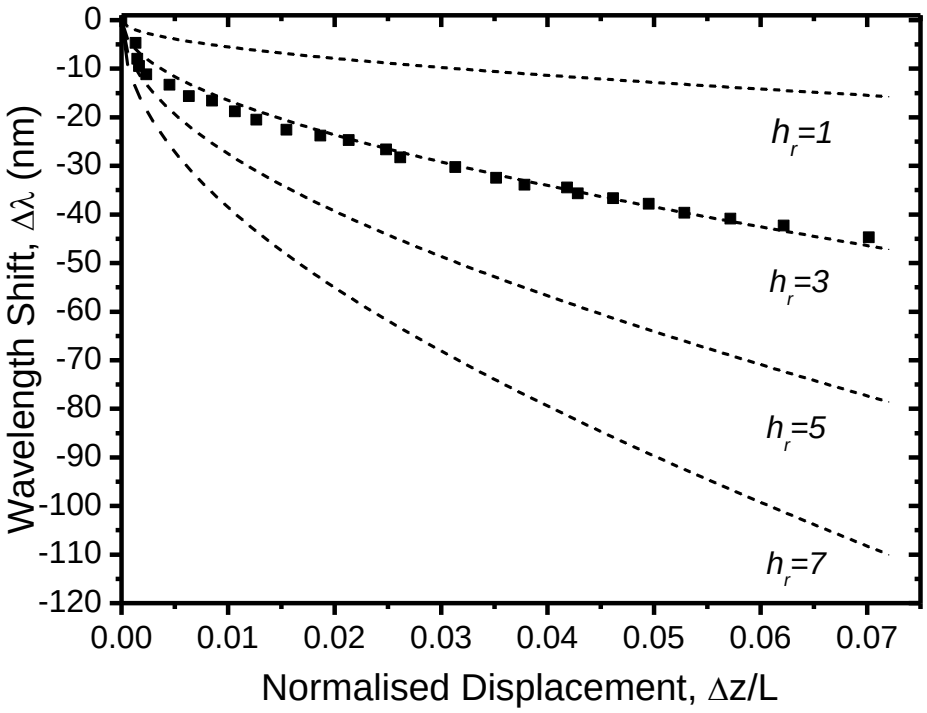

Figure 5.4: Fundamental wavelength shift plotted against the normalised horizontal displacement for different values of h_r, dotted lines indicate theoretical and black boxes indicate actual measured values.

Figure 5.4 show the relationship between $\Delta\lambda$ and the normalised displacement, $\Delta z/L_b$ for various values of h_r (see Figure 5.2). The data points show the actual experimental values obtained for wavelength tuning of the $4cm$ PPSF device. The experimental data are in good agreement with theoretical curves for the $h_r = 3mm$ case, demonstrating that the wavelength can be precisely controlled. It can be seen from the theoretical curves of Figure 5.4 that larger values of h_r allow broader tuning for the same displacement. The ~45nm shift in the fundamental wavelength is obtained with a normalised displacement of 0.07 in the compression mode. While it is a significant improvement over the $\sim 28nm$ reported previously [8], it still falls short of the $110nm$ achieved in FBGs through compression tuning. The reasons for this shortfall are attributed to the fragility of the twin-hole fibre used for this work and to the presence of two splice points inside the composite beam. The splice points also prevented tuning of the device in extension mode, as had been done with FBGs, to further extend the tuning range [7]. It should be possible to further increase the SH tuning range by placing the splice points outside the beam and/or by utilising twin-hole fibres more resilient to axial stresses. The axial strength could be improved by revising the geometrical design of the present twin-hole fibre.

Unlike periodically poled ferroelectric crystals, in PPSFs broadband tuning is possible purely through compressive tuning, enabling a wide range of SHG wavelengths to be accessed using a single device. The PPSF device can be maintained at room temperature, preserving the induced SON, which in turn ensures a stable and consistent SH signal.

5.2 Bandwidth engineering

The concept of *chirping* to broaden the bandwidth of grating-based components has existed for some time. Chirped period grating structures have been fabricated on thin-film structures for broadband filter devices [9], output couplers [10] and wavelength demultiplexers [11]. The advent of the FBG has resulted in the use of the chirped structure grating for a range of specialist applications. The negative group velocity dispersion (GVD) displayed by these gratings has been exploited for dispersion compensation. Some other common applications include, chirped pulse amplification [12], gain flattening filters [13], band-blocking/band-pass filters [14], etc.

5.2.1 Chirped SON grating

The acceptance bandwidth of QPM structures is controlled by the GVM and length of the periodically poled device as explained in Section 2.6. The inverse relationship between the interaction length and the bandwidth was also explained. Conversely the conversion efficiency for processes such as frequency doubling scales quadratically with the interaction length. Detailed theoretical analysis of linearly chirped bandwidth of periodically poled devices was given by Suhara and Nishihara [15]. Helmfrid and Arvidsson also provided a similar treatment approaching it from a practical point of view of the fabrication of periodic grating structures for QPM in crystals taking into consideration random variations of domain lengths and the effective index [16]. At the time the accuracy of the photolithographic fabrication techniques was insufficient to create the linearly varying chirp structure for the experimental demonstration. A segmented structure consisting of several uniform period gratings of varying periods was proposed as an alternative to achieve bandwidth broadening and demonstrated [17].

Arbore et al showed that SHG and pulse compression can be achieved simultaneously in the same chirped structure [18]. The chirped QPM grating exhibits an effect analogous to group velocity dispersion (GVD) where the time delay experienced by the generated SH wave relative to the fundamental wave can be exploited to stretch or compress the SH pulse. This effective GVD is a result of the interplay of two phenomena: group-velocity mismatch between the fundamental and the SH pulses, which is intrinsic to the nonlinear material, and spatial localisation of SHG of particular frequency components, a property of chirped QPM gratings [18]. A 150-fold compression over the fundamental wave was subsequently demonstrated with the generated SH having a pulse duration of $150fs$ [19].

5.2.2 Chirped period PPSF

Over the course of this present work, it became clear that significant improvements yielding high and stable SON in poled silica fibres was not possible without instituting major changes to the make-up of the glass. Since the objective was to keep the fibre parameters (such as NA, core size) as close as possible to standard fibres for straightforward integration, it was decided that the only remaining alternative was to extend the interaction lengths of the PPSF devices. As the PPSF fabrication capabilities were improved over the course of this present work, longer devices for QPM-SHG were fabricated. The problem of mismatch between acceptance bandwidth of the PPSF and the linewidth of laser sources, particularly for SHG at shorter wavelengths was envisaged and using chirped structures to improve conversion efficiencies was considered. To this end a number of experiments exploring this possibility were conducted. In the following sections, the evolution of SH in a chirped period poled fibre is mathematically described, following which the experimental results are presented.

5.2.3 SH evolution in a chirped QPM grating

The coupled mode equations derived for the SHG process in Section 2.4.3 can be adapted to describe the amplitude evolution of the fundamental and SH waves in a chirped period poled device. The SH wave is now represented by

$$\frac{dA_{2\omega}}{d\zeta} = -\frac{i\omega d_{33}}{n_{2\omega}c} A_{\omega}^{2} e^{i\varphi\zeta} \quad (5.7)$$

And similarly for the fundamental wave,

$$\frac{dA_{\omega}}{d\zeta} = -\frac{i\omega d_{33}}{2n_{\omega}c} A_{2\omega} A_{\omega}^{*} e^{-i\varphi\zeta} \quad (5.8)$$

with ζ the normalised propagation coordinate given by $\zeta = \frac{y}{L}$, replacing y and φ is the phase term associated with the phase mismatch which for a chirped structure is position dependent. L is the total length of the device.

$$\varphi(\zeta) = \int_{0}^{\zeta} \Delta\beta(\zeta) L d\zeta \quad (5.9)$$

where $\Delta\beta$ is the phase mismatch which in terms of actual position coordinate y is given by

$$\Delta\beta(y) = \frac{4\pi}{\lambda_{\omega}(n_{2\omega} - n_{\omega})} - \frac{2\pi}{\Lambda(y)} \quad (5.10)$$

where the QPM period (variable along y) is given by

$$\Lambda(y) = \Lambda_0 + \frac{\Delta\Lambda}{L} y \quad (5.11)$$

where Λ_0 is the initial QPM period and $\Delta\Lambda$ is the total chirp of the grating.

5.2.4 Experimental results

In the first instance a number of chirped period devices were fabricated from the ACREO-1 fibre. The uniformly poled devices were erased with chirps ($\Delta\Lambda$) varying from $0 - 0.5\mu m$ over a length of $8cm$, corresponding to an acceptance bandwidth variation of $3 - 26.4nm$ [20]. The maximum acceptance bandwidth was chosen to be narrower than the gain bandwidth of the ORC MOPA source employed for the characterisation of the devices (Section 3.4.1). When the CW broadly tunable source became available, the experiments were repeated with the FORC-2 fibre to demonstrate

even greater acceptance bandwidths. The source with its very broad tuning range, very narrow linewidth and constant output power was ideal to generate the SH tuning profiles of the chirped period poled fibre. The improved results are presented in this section.

Six devices were fabricated from FORC-2 fibre with chirps ($\Delta\Lambda$) of $0, 0.13, 0.25, 0.60, 1.00, 1.50\mu m$. The devices were characterised with the above mentioned CW tunable source. The output of the source was launched into a fibre polarisation controller and then into the device under test. The generated SH was measured using a silicon head detector (Newport 818-SL) connected to a power meter (Newport 2936-C). A LabView program was used to control and scan the tunable laser at $0.05nm$ steps and record the SH power after each wavelength adjustment. The polarisation controller was used to optimise the SH power of each device prior to the measurements. The measurements were performed with all fibres held firmly in place to minimise polarisation drifts and with the lights off to lower contributions to the SH power from ambient light. The measured SH power was typically in the hundreds of pW range.

The normalised wavelength tuning curves of the generated SH profiles for the six devices of varying chirp rates are shown in Figure 5.5 (a) – (f). The blue dots indicate the actual experimental measurement, while the red line indicates the theoretical fit of the SH evolution. The theoretical simulations were generated in collaboration with K. Gallo at the KTH Royal Institute of Technology, Sweden. The refractive index-wavelength relation (see Section 4.2.6) generated by a mode propagation simulator from the measured index profile was used to simulate the SH evolution for the unchirped and chirped devices. The device with no chirp (Figure 5.5(a)) was used as the reference to introduce a correction factor to the fibre dispersion which was marginally underestimated in the mode propagation simulation. The SH evolution for the chirped devices were then simulated using only the start and end QPM periods. In the unchirped case the experimental SH curve is very symmetrical and the lobes are a very close match of the theoretical simulation. The experimental data for the chirped cases (Figure 5.5 (b) – (f)) are also in very good agreement with the theoretical curves. Although there is some discrepancy in the amplitude levels, the characteristic spectral features of linearly chirped QPM structures are present in every case.

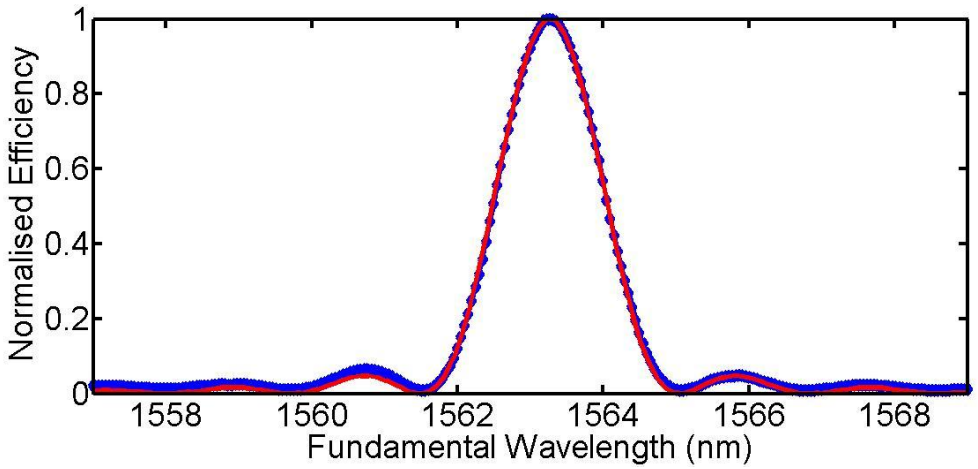

Figure 5.5(a) Unchirped PPSF

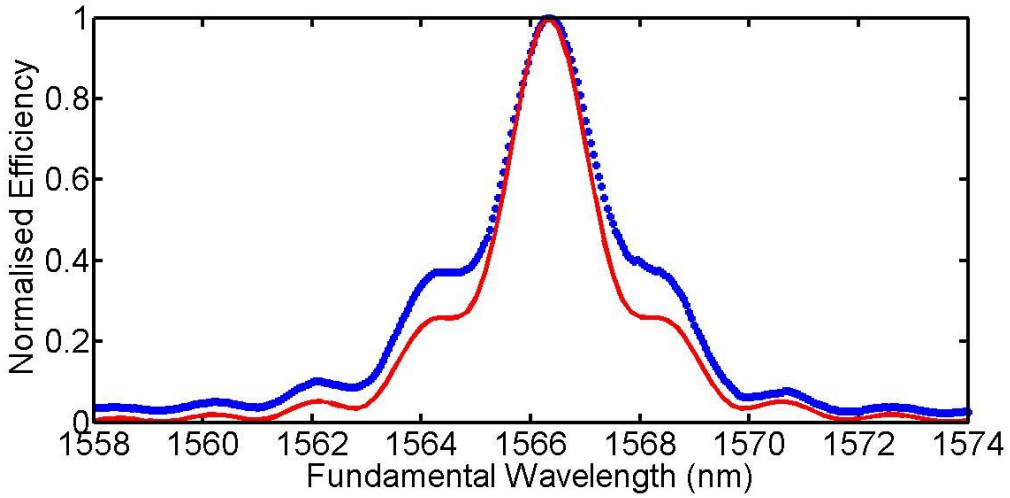

Figure 5.5(b) Chirped, $\Delta\Lambda = 0.13\mu m$

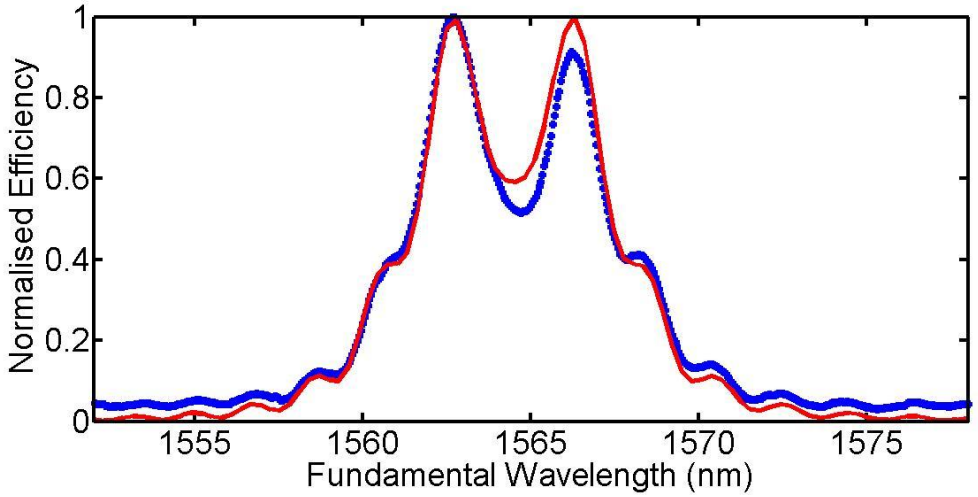

Figure 5.5(c) Chirped, $\Delta\Lambda = 0.25\ \mu m$

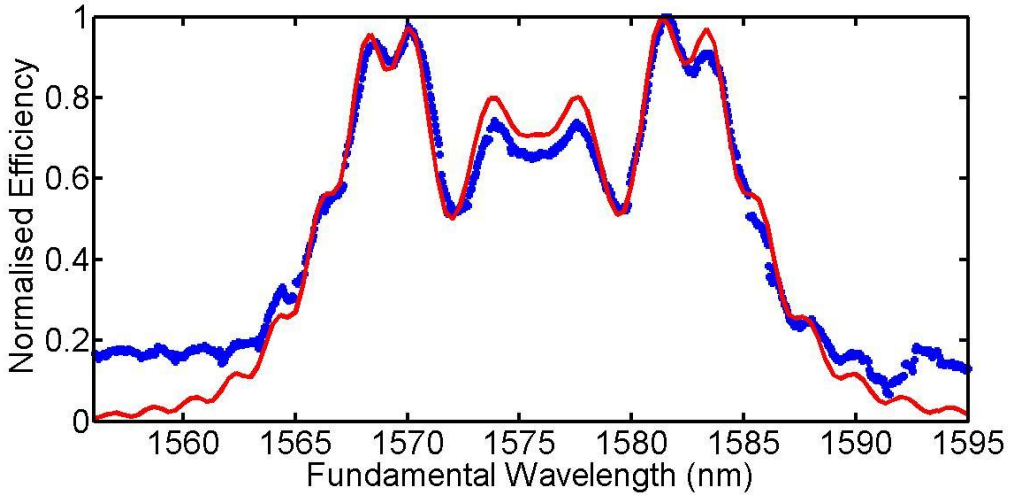

Figure 5.5 (d) Chirped, $\Delta\Lambda = 0.6$ µm

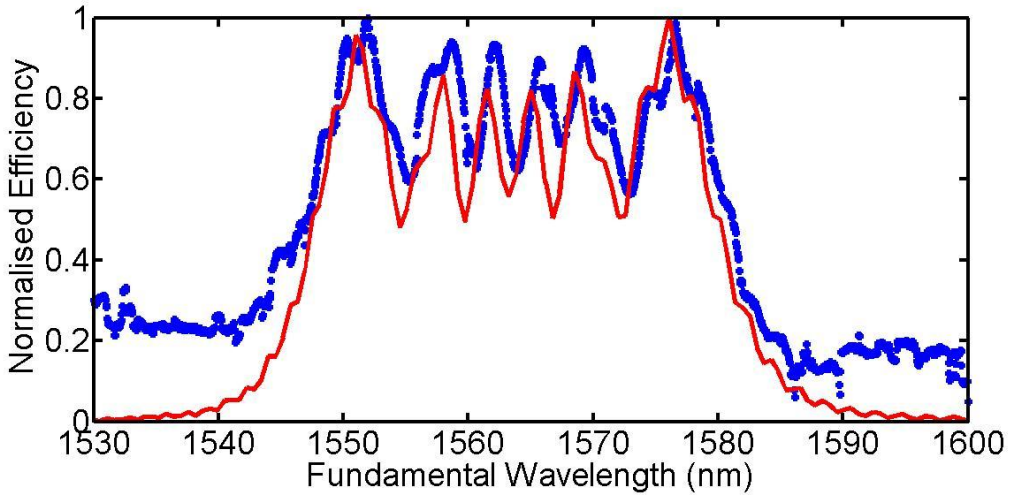

Figure 5.5(e) Chirped, $\Delta\Lambda = 1$ µm

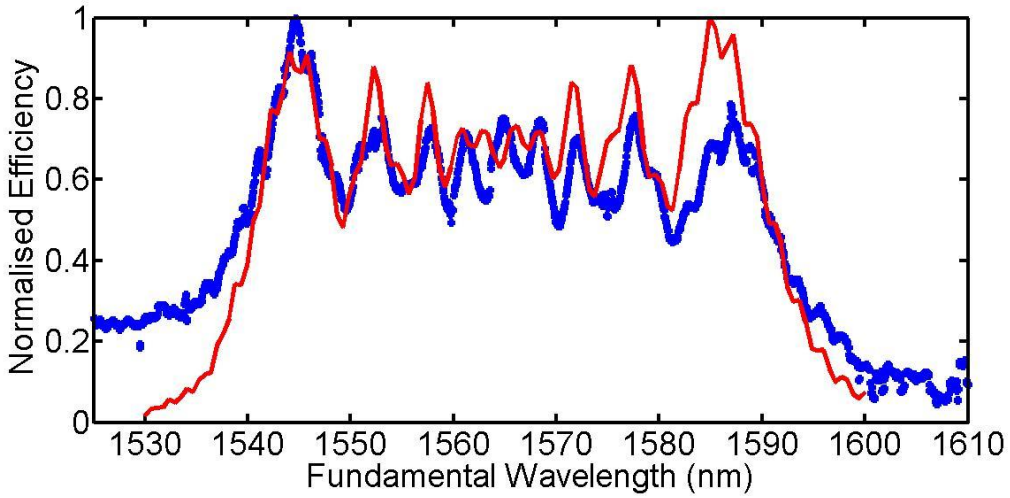

Figure 5.5(f) Chirped, $\Delta\Lambda = 1.5$ µm

The bandwidths of the chirped devices as measured at full-width-half-maximum (FWHM) are shown as a function of the chirp for each of the devices in Figure 5.6 (a) The theoretical values inferred from the SH amplitude simulations (Figure 5.5) are also shown on the same graph. The experimental and theoretical bandwidths are in good agreement with each other. The scaling of the normalised conversion efficiency with increasing chirp is shown in figure 5.6(b). The theoretical values were normalised to the unchirped device with the assumption that the nonlinearity was the same in all devices. The values are in good agreement with each other besides that of the device with the chirp of $\Delta\Lambda = 0.13\mu m$. This discrepancy is thought to be due to lower induced nonlinearity in this device.

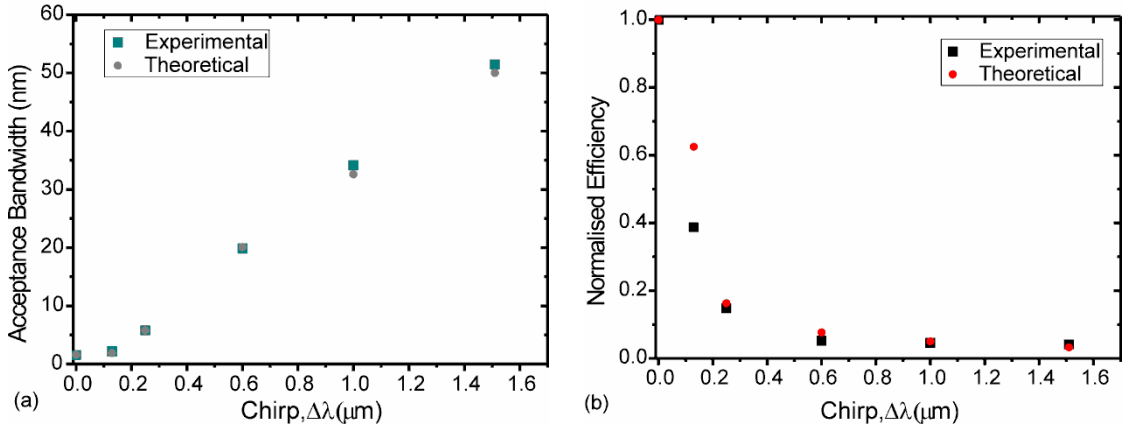

Figure 5.6 (a) Measured bandwidth of the chirped devices and (b) normalised efficiency as a function of the chirp

Comparing the device with the chirp of $\Delta\Lambda = 1.5\mu m$ to that of the uniform period device, the bandwidth has been enhanced by a factor of ~ 33, while the conversion efficiency has been lowered by factor of ~ 25, in agreement with theoretical predictions. In comparison the efficiency would drop almost a 1000 times (33^2) in a uniform device having the same bandwidth. In the pulsed regime the acceptance bandwidth exceeding $50nm$ realised in this $10cm$ long aperiodically poled device is sufficient to accommodate the spectrum of a $1.5\mu m$ transform-limited $50fs$ pulse. Provided that the fundamental pulse is stretched in a linear delay line to produce a chirp matching the effective GVD induced by the chirped QPM grating, a chirp free SH pulse is produced [15, 19]. The QPM grating shown in Figure 5.5 (f), having a GVM $of\ 0.04\ ps/mm$ at $1550nm$, would be suitable to produce $50/\sqrt{2}fs$ transform limited SH pulses, when $50fs$ pulses at the fundamental harmonic are stretched to $\sim 11ps$.

An acceptance bandwidth exceeding $50nm$ was realised in this $10cm$ long aperiodically poled device. The ability to precisely control the acceptance bandwidth of

the QPM interaction suggests that longer devices can be fabricated and it also enables efficient frequency doubling of high power, sources of short pulse durations. Further, tunable SH can be realised in chirped period poled devices. Small mismatches in the QPM wavelength of the PPSF and the source wavelength can be compensated by using a chirped device. This ensures that the stability of the output SH power and the conversion efficiency are preserved.

5.3 Conclusions

The functionalities of the PPSF has been extended through two demonstrations. In the first, the QPM period was altered through mechanical compression, resulting in wavelength tunability. A wavelength tuning range of $\sim 45nm$ in the fundamental was demonstrated with further tuning limited by the fragility of the splices between the twin-hole fibre and the SMF-28 pigtails. This technique can be used to realise a visible all-fibre wavelength tunable laser system based on erbium or ytterbium gain media.

In the second demonstration, the acceptance bandwidth of the PPSF was expanded significantly by a factor of ~ 33 in a $10cm$ long device. The fabrication of the aperiodic structure is far simpler in comparison to the same in crystals. The ability to control the bandwidth of the PPSF interaction is useful in optimising the QPM interaction. The linewidth of the fundamental source and the acceptance bandwidth can be matched closely to improve the conversion efficiency. Wavelength tunability is also possible using this technique.

5.4 References

1. Myers, L.E., et al., *Multigrating quasi-phase-matched optical parametric oscillator in periodically poled LiNbO3.* Optics Letters, 1996. **21**(8): p. 591.
2. Pruneri, V., et al., *532 nm Pumped Optical Parametric Oscillator in Bulk Periodically Poled Lithium-Niobate.* Applied Physics Letters, 1995. **67**(15): p. 2126.
3. Ishigame, Y., T. Suhara, and H. Nishihara, *LiNbO3 Wave-Guide Second-Harmonic-Generation Device Phase Matched with a Fan-out Domain-Inverted Grating.* Optics Letters, 1991. **16**(6): p. 375.
4. Powers, P.E., T.J. Kulp, and S.E. Bisson, *Continuous tuning of a continuous-wave periodically poled lithium niobate optical parametric oscillator by use of a fan-out grating design.* Optics Letters, 1998. **23**(3): p. 159.

5. Meyn, J.P. and M.M. Fejer, *Tunable ultraviolet radiation by second-harmonic generation in periodically poled lithium tantalate.* Optics Letters, 1997. **22**(16): p. 1214.
6. Xu, C.Q., H. Okayama, and Y. Ogawa, *Photorefractive damage of LiNbO3 quasiphase matched wavelength converters.* Journal of Applied Physics, 2000. **87**(7): p. 3203.
7. Mokhtar, M.R., et al., *Fibre Bragg gratings compression-tuned over 110nm.* Electronics Letters, 2003. **39**(6): p. 509.
8. Canagasabey, A., et al. *Tuneable Second Harmonic Generation in Long Periodically Poled Optical Fibres*. in *OFC*. 2005. Anaheim, California, USA: Optical Society of America.
9. Hong, C.S., et al., *Broad-band grating filters for thin-film optical waveguides.* Applied Physics Letters, 1977. **31**(4): p. 276.
10. Katzir, A., A.C. Livanos, and A. Yariv, *Chirped-grating output couplers in dielectric waveguides.* Applied Physics Letters, 1977. **30**(5): p. 225.
11. Livanos, A.C., et al., *Chirped-grating demultiplexers in dielectric waveguides.* Applied Physics Letters, 1977. **30**(10): p. 519.
12. Boskovic, A., et al., *All-Fiber Diode-Pumped, Femtosecond Chirped Pulse Amplification System.* Electronics Letters, 1995. **31**(11): p. 877.
13. Kashyap, R., R. Wyatt, and P.F. Mckee, *Wavelength Flattened Saturated Erbium Amplifier Using Multiple Side-Tap Bragg Gratings.* Electronics Letters, 1993. **29**(11): p. 1025.
14. Zhang, L., et al., *Postfabrication Exposure of Gap-Type Bandpass-Filters in Broadly Chirped Fiber Gratings.* Optics Letters, 1995. **20**(18): p. 1927.
15. Suhara, T. and H. Nishihara, *Theoretical-Analysis of Wave-Guide Second-Harmonic Generation Phase Matched with Uniform and Chirped Gratings.* Ieee Journal of Quantum Electronics, 1990. **26**(7): p. 1265.
16. Helmfrid, S. and G. Arvidsson, *Influence of randomly varying domain lengths and nonuniform effective index on second-harmonic generation in quasi-phase-matching waveguides.* Journal of the Optical Society of America B-Optical Physics, 1991. **8**(4): p. 797.
17. Mizuuchi, K., et al., *Broadening of the Phase-Matching Bandwidth in Quasi-Phase-Matched Second-Harmonic Generation.* IEEE Journal of Quantum Electronics, 1994. **30**(7): p. 1596.
18. Arbore, M.A., O. Marco, and M.M. Fejer, *Pulse compression during second-harmonic generation in aperiodic quasi-phase-matching gratings.* Optics Letters, 1997. **22**(12): p. 865.
19. Arbore, M.A., et al., *Engineerable compression of ultrashort pulses by use of second-harmonic generation in chirped-period-poled lithium niobate.* Optics Letters, 1997. **22**(17): p. 1341.
20. Canagasabey, A., et al. *Bandwidth Control of Second Harmonic Generation through Chirped Period Poling of Optical Fibres*. in *CLEO*. 2007: Optical Society of America.

Chapter 6: Conclusions and future Work

6.1 Conclusions

The primary objective of this present work was to improve the conversion efficiency of frequency doubling of fibre lasers through the use of periodically poled silica fibres (PPSF). Fibre lasers operating in the telecommunications C-band were singled out to achieve this objective since they were readily available. The first report of high conversion efficiency in a PPSF was achieved with a very high peak power source ($4kW$) as the length of the device was limited to $7.5cm$ by the photolithography technique employed [1]. The technique of uniform poling and subsequent UV erasure overcomes this fundamental limitation and made the fabrication of long PPSF devices feasible. Using this novel technique, the PPSF length was initially improved to $11.5cm$, contributing in part to a four-fold improvement in the normalised conversion efficiency (η_1) [2]. The high NA (0.28) of the fibre used (ORC-1) resulted in an improved (lower) overlap area (A_{OVL}) of the interacting fundamental and second harmonic (SH) modes. The lower overlap area of the fibre used was the second contributing factor in the improvement in the normalised efficiency. The choice of high NA for the ORC-1 fibre was to improve the confinement of the modes to minimise leakage loss into the anode hole. The high germanium content in the core is believed to raise the concentration and/or mobility of charge carriers, thereby increasing the induced nonlinearity [3]. The induced nonlinearity however was relatively modest ($d_{33} = 0.029pm/V$), comparable to that of the ACREO-1 fibre with its lower NA of 0.2. The low nonlinearity is attributed to the barrier like effect of the core-cladding interface and the initial fast decay which occurs over several hours after poling [4-6]. An improvement of ~ 2.2 times was made in the normalised conversion efficiency with the ACREO-2 fibre. The improvement was achieved purely through an enhancement of the length ($2X$), with the greater area overlap ($2X$) preventing a quadratic scaling of the conversion efficiency. The best PPSF sample fabricated from the ACREO-1 fibre had an average conversion efficiency of $\sim 11\%$. However this level of conversion was short lived, decaying to 7.5% in less than 24 hours. Since the ACREO-1 fibre was expended by this stage, the FORC-1 fibre, which has a similar design, was used to study the

decay of the induced nonlinearity. This study confirmed that the decay can be quite significant, with some samples losing about 50% of the initial nonlinearity within hours of poling before stabilising. All twin-holes fibres fabricated were found to have a degree of drawing induced twist which limits the length of the periodic UV erasure. The ACREO-1 fibre for instance was limited to a PPSF length of $\sim 20 cm$. Thus it was clear at this stage that either a reduction in twist or an improvement in the induced nonlinearity was necessary for further improvement of the conversion efficiency. The FORC-2 fibre was designed with these considerations in mind. The core was positioned further away from the anode, since it was believed that injected neutralising charges are less mobile and are less likely to reach the core. The separation between the holes was increased significantly. This was necessary to accommodate the larger core and to maintain the asymmetric offset of the core in relation to the holes. The larger separation of the holes would also assist in creating a wider depletion region, ensuring a greater overlap of the core. The lower NA of the fibre reduces the disparity between the refractive indices of the core and cladding, thereby reducing the barrier like effect at the interface. The NA of the FORC-2 is also closely matched to that of standard fibres and doped fibres typically used in fibre lasers, alleviating splice losses.

In the revised design of the twin-hole fibre (FORC-2), the induced nonlinearity was improved by a factor of ~ 2 over the fibres used previously in the reports of the frequency doubling with PPSFs and also with the ACREO-1 fibre. The improvement is credited largely to the major improvement in the stability of the induced second order nonlinearity (SON).

The interaction length of the FORC-2 fibre was improved significantly over previous reports and over the longest device fabricated with the ACREO-1 fibre. Although the drawing induced twist of the FORC-2 was comparable to the ACREO-1 fibre, the accessibility of the UV beam to the core was improved through its placement away from the holes, permitting the fabrication of longer periodic lengths. In fact, the PPSF length in the FORC-2 was limited only by the range of the translation stage used. The improvement of the PPSF length and the induced SON did not result in quadratic improvements of the conversion efficiency over the ACREO-1 fibre as the overlap area of the FORC-2 fibre was significantly larger. Nevertheless a four-fold improvement of the normalised conversion efficiency (η_1) was achieved with the FORC-2 fibre over the

ACREO-1 fibre. The improvement resulted in a demonstration of $\sim 15\%$ average conversion efficiency using a fibre laser source of $\sim 200W$ peak power.

A range of improvements were made to the basic design of the specialty twin-hole fibre to overcome a number of limiting factors in achieving a high and stable conversion efficiency. This present work was commenced with the construction of an all-fibre interferometer capable of measuring the evolution of the SON during poling. The use of this system helped determine the optimum poling conditions required to induce the maximum possible SON. The interferometers were heavily used to optimise poling conditions in each of the fibres and later to improve the design of the FORC-2 fibre. A range of enhancements were made to the interferometric measurement system resulting in a 10-fold reduction in the error levels.

The functionality of the PPSF was improved with the demonstrations of broadband wavelength tunability and bandwidth engineering through chirped period poling. A wavelength tuning range of $\sim 45nm$ was demonstrated using a robust compressing tuning package. The tunable PPSF is particularly suited for use with tunable fibre laser sources such as those based on erbium/ytterbium gain media. The acceptance bandwidth of the PPSF devices can be controlled precisely through chirped period poling. In this demonstration, an expansion factor of 33 of the bandwidth was achieved. An acceptance bandwidth exceeding $50nm$ was realised in a $10cm$ long aperiodically poled device.

The highly precise domain boundaries of the PPSF grating resulting in comparable experimental and theoretical SH tuning profiles were fabricated using the point-by-point UV exposure technique typically used in the fabrication of long period fibre gratings. The high accuracy and versatility of this technique permits the fabrication of very long, high quality PPSF gratings, with lengths of $1m$ considered attainable. In addition, the phase matching structure can be engineered to match the properties of the pump laser source, optimising the conversion efficiency and enhancing the spectral quality of the generated waves. Devices with broadened acceptance bandwidths can also be used to realise tunable SH or simply to lower the tolerance of the quasi phase matching wavelength. This feature is particularly attractive for the preservation of the stability of the output SH power and the conversion efficiency for pump sources with

wavelength instabilities or changes to the phase matching condition of the poled fibre device resulting from arbitrary variations in the operating temperature.

The demonstration of wavelength tunability, high average SH power and reasonable conversion efficiency has generated some interest from a number of fibre laser manufacturing companies. These companies either had an existing product utilising nonlinear crystals for visible wavelength generation or were interested in introducing one. The fresh prospect of using a PPSF to create a truly all-fibre system, overcoming a number of issues inherent to crystal based frequency doubling was the main motivating factor. In this present work, the groundwork required to achieve very high conversion efficiencies has been completed. Conversion efficiencies exceeding that reported within this thesis can be obtained by means of improving the SON, by extending the interaction length or by employing a fundamental source with higher peak powers.

6.2 Future work

The most obvious routes to enhancing the conversion efficiency in the existing fibres is either through the use of higher power lasers or through the extension of the PPSF interaction length. Although fibre devices with electrode overlaps approaching $0.5m$ lengths have been fabricated, the periodically poled length was limited by the translation stage used in this present work. Translation stages with greater travel range can be used to fabricate longer PPSF devices. Extending the device length to $50cm$ in the FORC-2 fibre for instance, would result in a conversion efficiency of almost 40% for the same $207W$ laser source used (Multitel-MOPA). It is believed that the PPSF can handle powers of over $1kW$ sources operating in the erbium/ytterbium regime. However for frequency doubling of high power sources with wavelengths around $1\mu m$, a study on the stability of the induced SON is required to ascertain their suitability as two photon absorption of the generated second harmonic could potentially erase the induced nonlinearity. An alternative technique to extending the length would be to splice two separate PPSF devices of closely matched wavelengths of operation. This technique requires the devices to be mounted on separate wavelength tuning stages and an intermediate stage to compensate for the phase mismatch in between them. Some preliminary work has been completed with PPSF devices fabricated from the FORC-2 fibre mounted on Peltier temperature tuning stages. Although precise overlap of the SH tuning curves of the two devices was achieved, the expected quadratic improvement in

the conversion was not obtained as a result of very high splice losses between the devices. The losses are attributed to diameter variations of the twin-hole fibre in the section of fibre used for the concatenation work.

Another route to enhancing the conversion is through the re-circulation of the unconverted pump photons via double or multi-pass schemes. A simple scheme of pump re-circulation can be achieved with FBGs fabricated directly into the twin-hole fibre, on either side of the periodically poled section. Bragg reflectors at the SH wavelength would be required on the input end to reflect the generated SH on the return passes. A femtosecond laser source can be used for FBG fabrication in the case of fibres with low UV photosensitivity. This idea can be extended to the realisation of an optical parametric oscillator (OPO) based on the PPSF. Wavelength tunability of the OPO using the grating compression technique realised in this present work is also practicable.

Supercontinuum generation has been demonstrated in holey fibres by pumping at the zero-dispersion wavelength (ZDW) with short duration pulses (nanosecond, femtosecond) [7-8]. The ability to design holey fibres with the ZDW matched to the wavelength of the fundamental pump source makes all-fibre supercontinuum sources possible. Further, pumping at shorter wavelengths enhances the power in the visible range and pushes the spectral envelope further into the UV. Double wavelength pumping has been proposed to overcome the requirement for precise matching of the fundamental and ZDW wavelengths [9]. Pumping around the ZDW is also useful in improving the spectral density of the visible wavelengths. The use of PPSFs for this particular application is envisaged. For instance, a ytterbium doped fibre laser operating around $1\mu m$ can be frequency doubled. The generated green light along with the residual pump can be used to pump a holey fibre for broadband supercontinuum generation.

6.3 References

1. Pruneri, V., G. Bonfrate, P.G. Kazansky, D.J. Richardson, N.G. Broderick, J.P. deSandro, C. Simoneau, P. Vidakovic, and J.A. Levenson, *Greater than 20% efficient frequency doubling of 1532nm pulses in quasi-phase-matched germanosilicate fibres.* Optics Letters, 1999. **24**(4): p. 208.

2. Corbari, C., A. Canagasabey, M. Ibsen, F.P. Mezzapezza, C. Codemard, J. Nilsson, and P.G. Kazansky. *All-fibre frequency conversion in long periodically poled silica fibres*. in *OFC*. 2005. Anaheim, California, USA: Optical Society of America.
3. Fleming, S.C. and H. An, *Poled glasses and poled fibre devices.* Journal of the Ceramic Society of Japan, 2008. **116**(1358): p. 1007.
4. Faccio, D., A. Busacca, D.W.J. Harwood, G. Bonfrate, V. Pruneri, and P.G. Kazansky, *Effect of core-cladding interface on thermal poling of germano-silicate optical waveguides.* Optics Communications, 2001. **196**(1-6): p. 187.
5. An, H.L. and S. Fleming, *Hindering effect of the core-cladding interface on the progression of the second-order nonlinearity layer in thermally poled optical fibers.* Applied Physics Letters, 2005. **87**(10): p. 101108.
6. An, H.L. and S. Fleming, *Overcoming the impeding effect of core-cladding interface on the progression of the second-order nonlinearity in thermally poled optical fibers.* Applied Optics, 2006. **45**(24): p. 6212.
7. Ranka, J.K., R.S. Windeler, and A.J. Stentz, *Visible continuum generation in air-silica microstructure optical fibers with anomalous dispersion at 800 nm.* Optics Letters, 2000. **25**(1): p. 25.
8. Provino, L., J.M. Dudley, H. Maillotte, N. Grossard, R.S. Windeler, and B.J. Eggleton, *Compact broadband continuum source based on microchip laser pumped microstructured fibre.* Electronics Letters, 2001. **37**(9): p. 558.
9. Champert, P.A., V. Couderc, P. Leproux, S. Fevrier, V. Tombelaine, L. Labonte, P. Roy, C. Froehly, and P. Nerin, *White-light supercontinuum generation in normally dispersive optical fiber using original multi-wavelength pumping system.* Optics Express, 2004. **12**(19): p. 4366.

Publications

1. Canagasabey, A., C. Corbari, M.R. Mokhtar, P.G. Kazansky, and M. Ibsen. *Tuneable Second Harmonic Generation in Long Periodically Poled Optical Fibres*. in *OFC*. 2005. Anaheim, California, USA: Optical Society of America.
2. Corbari, C., A. Canagasabey, M. Ibsen, F.P. Mezzapezza, C. Codemard, J. Nilsson, and P.G. Kazansky. *All-fibre frequency conversion in long periodically poled silica fibres*. in *OFC*. 2005. Anaheim, California, USA: Optical Society of America.
3. Canagasabey, A., J. Canning, J.D. Mills, D.P. Banks, and M. Ibsen. *Fibre Bragg fabrication in germanosilicate fibres with 244nm femtosecond laser light*. in *PICALO*. 2006. Melbourne, Australia.
4. Canagasabey, A., J. Canning, J.D. Mills, D.P. Banks, and M. Ibsen. *Femtosecond Pulsed 244nm versus CW 244nm Grating Writing in Boron Codoped Germanosilicate Optical Fibres operating within the one photon absorption regime*. in *ACOFT/AOS*. 2006. Melbourne, Australia.
5. Canagasabey, A., F.P. Mezzapesa, C. Corbari, P.G. Kazansky, and M. Ibsen. *75% Enhancement of the Second Order Nonlinearity in Twin-Hole Fibres through Voltage Assisted Cooling during Poling*. in *CLEO*. 2006: Optical Society of America.
6. Fotiadi, A.A., O. Deparis, P. Mégret, C. Corbari, A. Canagasabey, M. Ibsen, and P.G. Kazansky. *All-Fiber Frequency Doubled Er/Brillouin Laser*. in *CLEO/QELS*. 2006. Longbeach, California, USA: Optical Society of America.
7. Canagasabey, A., C. Corbari, P.G. Kazansky, and M. Ibsen. *Bandwidth Control of Second Harmonic Generation through Chirped Period Poling of Optical Fibres*. in *CLEO*. 2007: Optical Society of America.
8. Canagasabey, A., C. Corbari, Z.W. Zhang, P.G. Kazansky, and M. Ibsen, *Broadly tunable second-harmonic generation in periodically poled silica fibers.* Optics Letters, 2007. **32**(13): p. 1863.
9. Huy, K.P., A.T. Nguyen, E. Brainis, M. Haelterman, P. Emplit, C. Corbari, A. Canagasabey, M. Ibsen, P.G. Kazansky, O. Deparis, A.A. Fotiadi, P. Megret, and S. Massar, *Photon pair source based on parametric fluorescence in periodically poled twin-hole silica fiber.* Optics Express, 2007. **15**(8): p. 4419.
10. Canagasabey, A., C. Corbari, A.V. Gladyshev, F. Liegeois, S. Guillemet, Y. Hernandez, M.V. Yashkov, A. Kosolapov, E.M. Dianov, M. Ibsen, and P.G. Kazansky, *High Average Power Second-Harmonic Generaion from Periodically Poled Silica Fibres.* Accepted for publication in Optics Letters, 2009.
11. Canagasabey, A., C. Corbari, F. Liegeois, A.V. Gladyshev, S. Guillemet, Y. Hernandez, M.V. Yashkov, A. Kosolapov, E.M. Dianov, M. Ibsen, and P.G. Kazansky. *236mW Average Second-Harmonic Power Generated from Periodically Poled Silica Fibres*. in *Conference on Lasers and Electro-Optics*. 2009. Munich, Germany.